MRI of mouse heart failure

Citation for published version (APA):
Nierop, van, B. J. (2013). *MRI of mouse heart failure*. [Phd Thesis 1 (Research TU/e / Graduation TU/e), Biomedical Engineering]. Technische Universiteit Eindhoven. https://doi.org/10.6100/IR751939

DOI:
10.6100/IR751939

Document status and date:
Published: 16/05/2013

Document Version:
Publisher’s PDF, also known as Version of Record (includes final page, issue and volume numbers)

Please check the document version of this publication:

• A submitted manuscript is the version of the article upon submission and before peer-review. There can be important differences between the submitted version and the official published version of record. People interested in the research are advised to contact the author for the final version of the publication, or visit the DOI to the publisher's website.
• The final author version and the galley proof are versions of the publication after peer review.
• The final published version features the final layout of the paper including the volume, issue and page numbers.

Link to publication

General rights
Copyright and moral rights for the publications made accessible in the public portal are retained by the authors and/or other copyright owners and it is a condition of accessing publications that users recognise and abide by the legal requirements associated with these rights.

- Users may download and print one copy of any publication from the public portal for the purpose of private study or research.
- You may not further distribute the material or use it for any profit-making activity or commercial gain
- You may freely distribute the URL identifying the publication in the public portal.

If the publication is distributed under the terms of Article 25fa of the Dutch Copyright Act, indicated by the “Taverne” license above, please follow below link for the End User Agreement:

www.tue.nl/taverne

Take down policy
If you believe that this document breaches copyright please contact us at:

openaccess@tue.nl

providing details and we will investigate your claim.

Download date: 04. Oct. 2023

MRI of Mouse Heart Failure

This research was performed within the framework of the Center for Translational Molecular Medicine, project TRIUMPH (grant 01C-103), and supported by the Dutch Heart Foundation.

Financial support by the Dutch Heart Foundation for the publication of this thesis is gratefully acknowledged.

A catalogue record is available from the Eindhoven University of Technology Library
ISBN: 978-90-386-3360-2

Printed by: Ipskamp Drukkers BV, Enschede, The Netherlands
Lay-out: Bastiaan van Nierop
Cover design: Douwe Hoendervanger

MRI of Mouse Heart Failure

PROEFSCHRIFT

ter verkrijging van de graad van doctor aan de
Technische Universiteit Eindhoven, op gezag van de
rector magnificus, prof.dr.ir. C.J. van Duijn, voor een
commissie aangewezen door het College voor Promoties
in het openbaar te verdedigen
op donderdag 16 mei 2013 om 16.00 uur

door

Bastiaan Jeroen van Nierop

geboren te Hengelo

Dit proefschrift is goedgekeurd door de promotor:

prof.dr. K. Nicolay

Copromotor:
dr.ir. G.J. Strijkers

Contents

1

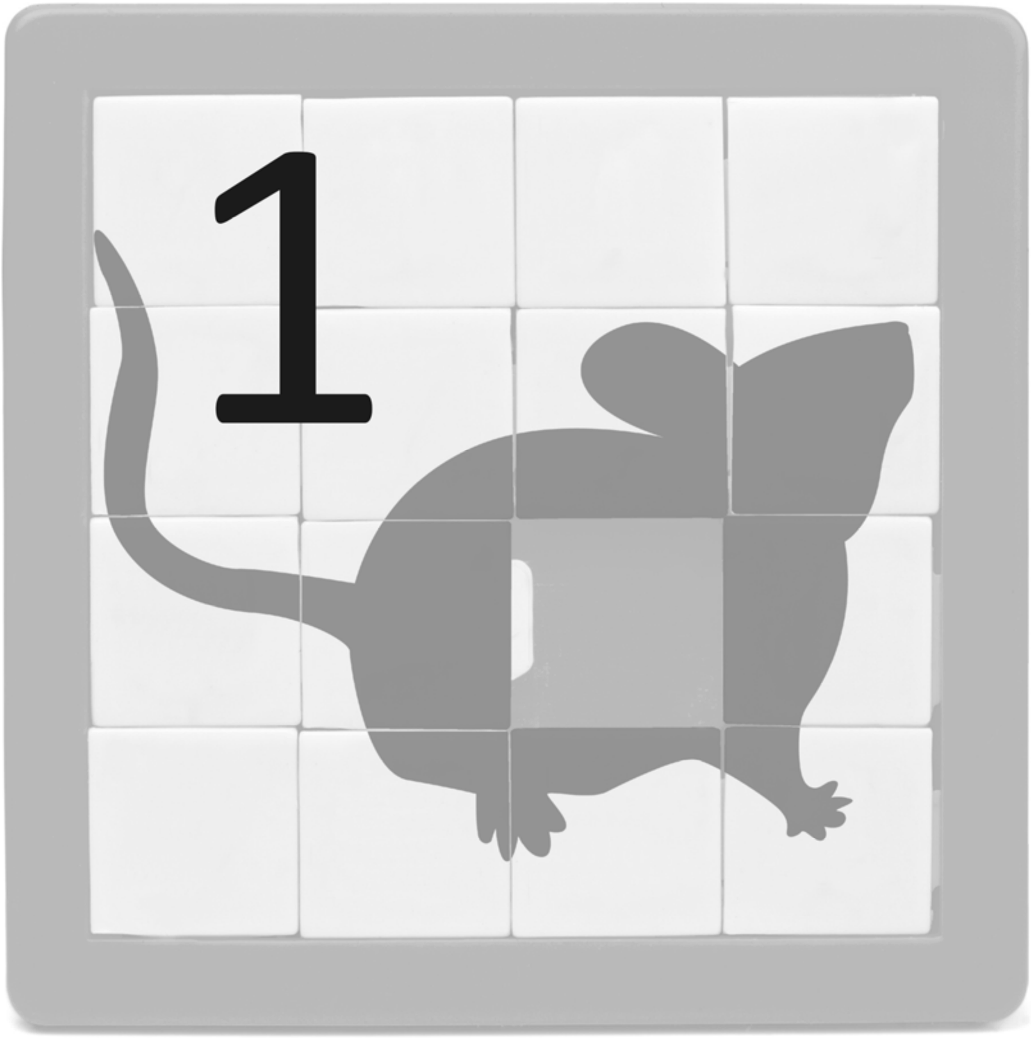

General introduction

The heart

The systemic circulation serves to deliver oxygen rich blood to the organs via the arterial circulation and to remove carbon dioxide and other waste products from the organs via the venous circulation. The primary responsibility of the heart, one of the most vital organs in the body, is to maintain an adequate pressure difference between the arterial and venous part of the circulation, thereby facilitating sufficient blood perfusion of the tissue capillaries.

The heart is divided in a right and left part responsible for the blood supply to the pulmonary circulation and the other organs, respectively (Figure 1.1). Both halves of the heart consist of an atrium and a ventricle. The atria collect blood returning to the heart from the venous system and provide active filling of the ventricles. Next, the ventricles pump the blood into the arterial circulation. The coronary arteries originate from the root of the aorta and provide the blood supply to the heart itself.

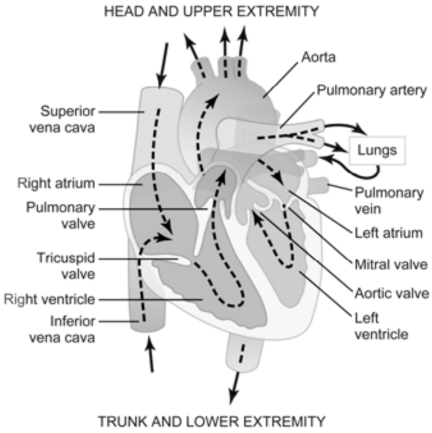

Figure 1.1. Anatomy of the heart. Indicated are the left ventricle (LV), right ventricle (RV), left atrium (LA), right atrium (RA), pulmonary artery and aorta. First, the heart collects blood it receives from the venous circulation in the RA, from where it enters the RV during diastole. In systole the deoxygenated blood is pumped to the lungs and then reenters the heart via the LA. The oxygenated blood then is moved to the LV during diastole again, and is pumped into the aorta during systole. Reprinted with permission from Guyton and Hall [1].

Approximately 75 percent of the cardiac tissue is occupied by cardiomyocytes (Figure 1.2). Important constituents of the remainder of the tissue are the extracellular matrix (ECM), myofibroblasts and blood vessels.

The ECM is a complicated, highly organized network. Its main constituent is collagen type I, but it also contains collagen type III and V, elastic fibers, proteoglycans and basement membranes. The ECM forms a structural backbone for the cardiomyocytes and the vasculature providing passive stiffness to the myocardium, preventing myocyte slippage and tissue deformation during ventricular filling. In addition, ECM components serve as important regulators of tissue growth, differentiation and angiogenesis [2,3]. Myofibroblasts in the heart play an important role in the generation

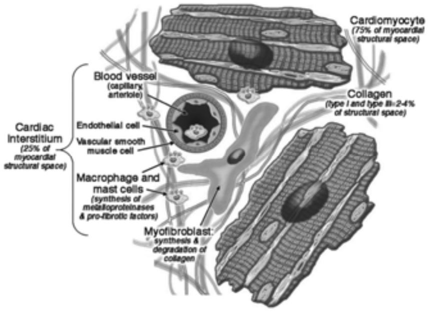

Figure 1.2. Schematic representation of the myocardial tissue. Indicated are the cardiomyocytes, collagen fibers, blood vessels, macrophages and mast cells, and myofibroblasts. Reprinted with permission from Mewton *et al.* [4].

and degradation of the ECM [5]. In particular as a result of tissue injury and during tissue remodeling these cells become active in response to cytokine activation or a mechanical challenge.

The intricate network of blood vessels in the heart plays a key role in providing the heart with oxygen and nutrients and removing waste products. The heart is unique in the sense that approximately 75% of the oxygen is extracted from the blood entering the heart, a fraction that is much lower in many other organs [6,7]. Increased oxygen extraction during periods of increased demand is therefore possible to a very limited extent. Instead, a sophisticated autoregulation mechanism ensures that the higher oxygen demand is met by increased myocardial perfusion [8].

An adequate cardiac energy metabolism plays a key role in enabling proper cardiac function, and consists of three major steps. First, free fatty acids and glucose are taken up in the cells and converted by means of beta-oxidation and glycolysis. The intermediates formed are fed into the Krebs cycle, in which NADH and CO_2 are formed. Second, NADH is used in the mitochondrial respiratory chain to generate energy that drives the phosphorylation of adenosine diphosphate (ADP) to obtain the high-energy compound adenosine triphosphate (ATP). Third, the creatine kinase shuttle is used to transport the chemical energy to the myofibrils where it is utilized for muscle contraction [9,10].

Heart failure

Heart failure (HF) is the final consequence of a large number of pathologies, but common to this defect is an inability of the heart to supply sufficient cardiac output to meet the body needs, due to impaired filling and/or ejection of blood [11,12]. HF is a major burden to patients in terms of a significantly reduced quality of life and is associated with high morbidity and mortality rates [13,14]. After the onset of HF the median survival is only 1.7 and 3.2 years for men and women, respectively [15,16]. In

Europe alone over 14 million people are affected by HF. Considerable advances have been made in the treatment of HF [17,18]. Despite this the future incidence is expected to increase due to ageing of the population, improved patient survival after ischemic heart disease, and the increased prevalence of diabetes and hypertension [19]. HF also forms a burden to society as a whole due to the high associated costs. It is estimated that between 1 and 2% of the annual healthcare budget is spend on treatment of HF patients [20].

Many pathologies can compromise cardiac function and ultimately lead to the development of HF, including diabetes, genetic disorders, volume- and pressure overload of the ventricles, and myocardial infarction [14]. Amongst these, pressure overload induced hypertrophy and myocardial infarction are the most frequent causes of HF [14,18,21].

The heart is capable to respond to an increased workload or loss of muscle tissue due to myocardial infarction, with various mechanisms [22]. In this way, the heart tries to compensate for the increased load and maintain a proper cardiac output. Although the morphological changes that occur in these pathologies may differ, the underlying mechanisms by which these lead to HF show many similarities [3,22,23]. The altered workload induces biomechanical and neurohumoral stress, both promoting intracellular signaling cascades that result in increased protein synthesis or stability [22,24]. This results in hypertrophic growth of the cardiomyocytes and thereby in a net increase in heart size [25]. Initially, myocardial hypertrophy helps to maintain cardiac output and might act as a compensatory mechanism by normalizing the increased wall stress thereby reducing biomechanical stress to the heart [26]. However, concomitant processes developing in concert with myocardial hypertrophy eventually have a deleterious effect and lead to a decompensated stage of hypertrophy. On a tissue level, remodeling results in myocardial fibrosis, impaired tissue perfusion and altered myocardial energetics [9,22,27,28]. On a gene level, maladaptation comes with re-expression of fetal genes, and altered expression of genes regulating calcium handling and metabolism [29]. All these processes together contribute to the development of HF, but the precise underlying mechanisms and their interactions are still poorly understood [25].

Fibrosis is defined by a substantial increase in myocardial collagen content and has two important subtypes (Figure 1.3). Interstitial fibrosis is often observed in response to pressure overload induced HF and results in a diffuse pattern of fibrosis throughout the myocardium. Focal or replacement fibrosis is found in the heart to replace tissue

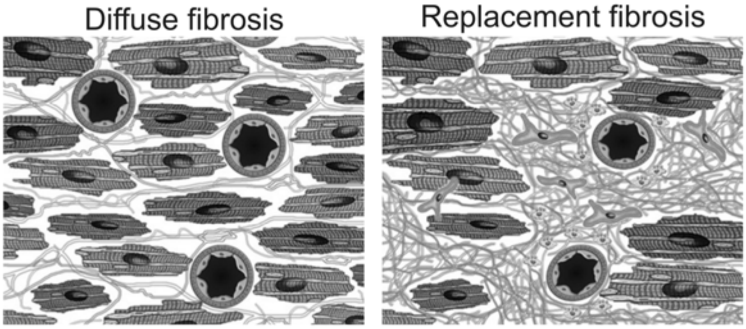

Figure 1.3. Schematic representation of myocardial tissue with formation of diffuse and replacement fibrosis. Reprinted with permission from Mewton *et al.* [4].

that died as a result of ischemic heart disease. The formed scar tissue does not contribute to myocardial contraction.

In HF vascular growth is outpaced by the hypertrophic growth of the myocytes resulting in a net decrease of the vascular density limiting myocardial perfusion [30]. In addition, the capability to increase blood supply to the heart under stress conditions, i.e., the myocardial perfusion reserve, is diminished in the hypertrophic heart. Moreover, perivascular fibrosis is often observed in HF and contributes to vascular abnormalities [31]. The resulting lower O_2 delivery capacity may promote apoptosis and fibrosis, and also has direct functional consequences in terms of impaired myocardial contractility [22,32]. Accumulating evidence supports the hypothesis that a (regional) mismatch between perfusion supply and demand in the heart is imperative for the development of HF [33-35].

It is thought that metabolic remodeling plays an important role during the development of HF [9,10]. In the hypertrophic heart the flux through the creatine kinase shuttle decreases, glucose uptake and utilization are increased and fatty acid oxidation might be near normal or decreased. When hypertrophy progresses towards a decompensated stage, the creatine kinase flux drops, and the rate of fatty acid oxidation is decreased, which cannot be compensated anymore by increased glucose utilization. As a result, the ATP supply diminishes [36]. Failure of cardiac metabolism to supply the heart with sufficient energy has detrimental consequences for cardiac function. Indeed, in ischemic and non-ischemic heart disease a decreased cardiac energy status is consistently reported [37-40].

Cardiac magnetic resonance

Nuclear magnetic resonance is based on nuclei that possess spin, for example ^1H and ^{31}P. When placed in a static magnetic field these spins align either in a parallel or anti-parallel orientation, described by the Boltzmann equation. At room temperature slightly more spins have a parallel than an anti-parallel orientation, resulting in a very small net magnetization vector M_0 aligned with the direction of the main magnetic field B_0 (the z-direction by convention). M_0 can be tilted towards the x-y plane when exposed to a second oscillating magnetic field in the perpendicular direction. Following the tilt into the x-y plane, M_0 precesses with the Larmor frequency in the x-y plane, where it induces a current in an RF receive coil. This is the magnetic resonance signal. M_0 will return to its equilibrium state along the z-direction over time, a process called relaxation. Relaxation of the x-y and the z-component of the magnetization vector are characterized by the transverse relaxation times T_2 and T_2*, and the longitudinal relaxation time T_1, respectively. Magnetic field gradients can be used to impose phase and frequency differences depending on the spatial location of the spins, thereby enabling the reconstruction of MR images from the object under study. The characteristic relaxation times and the proton density of tissue are widely exploited to generate image contrast. In general, image contrast in MRI depends on the MR sequence, the sequence parameters that are used, as well as the tissue under examination. As a result, MR imaging offers an ever expanding range of different image contrasts and is a very versatile technique.

Since magnetic resonance (MR) techniques were first used for imaging (MRI) and spectroscopy (MRS) of the heart in the ‘70s considerable technical improvements were made, leading to major advances in noninvasive cardiac imaging [41-43]. Cardiac magnetic resonance (CMR) techniques have become important tools both in the clinic and for research [44]. CMR offers excellent spatial resolution, good temporal resolution and unsurpassed soft tissue contrast as compared to other cardiac imaging modalities [45]. Moreover, virtually any oblique slice orientation can be obtained not necessitating geometrical assumptions for the assessment of ventricular function and mass. This is of particular importance for the study of remodeled ventricles, and when studying the right ventricle with its complex geometry [46]. CMR is now recognized as a robust and powerful imaging modality. It provides highly accurate and reproducible diagnostic information on various aspects of many different cardiovascular diseases, including cardiac morphology and function, blood flow, myocardial rest and stress perfusion, metabolism and tissue viability [41,43,47,48]. As a result, CMR has become a valuable tool for the diagnosis of patients with unclear etiology [49]. Despite the increasing clinical use of CMR, however, there is still much to gain with regard to its acceptance in the medical community [43,45,47,49,50].

On the downside, CMR generally involves long acquisition times and is hampered by limited availability and high costs [42]. The benefits and disadvantages of CMR are better appreciated when compared to other important cardiac imaging modalities. Echocardiography is still the workhorse in cardiac imaging and can provide data on cardiac morphology and function, valve function and blood flow. Echocardiography is relatively inexpensive and widely available. Disadvantages include limited tissue contrast and the possibility of restricted acoustic windows, especially around thoracic structures. Nuclear imaging techniques are very sensitive and provide valuable information on cardiac perfusion and metabolism [45,51]. Downsides of nuclear imaging techniques are the limited spatial resolution, the use of tracers that emit ionizing radiation and the requirement of anatomical reference information obtained from another imaging modality, mostly computed tomography.

HF, irrespective of the precise etiology, is typically progressive in nature, very complex, and the symptoms and outcome in patients are highly variable [16,18]. HF is often difficult to detect in an early stage and the clinical picture of HF cannot be adequately described by one single measurement parameter, in particular not on an individual basis [21]. It is becoming increasingly clear, though, that it is of utmost importance for the patient to intervene as early as possible in the disease process, even before symptoms have developed [21,52].

Diagnosing the underlying etiology in HF remains an important challenge and current diagnostic techniques could benefit from increased specificity in identifying the precise etiology causative of cardiac disease [46]. It is anticipated that plasma biomarkers in conjunction with further improvements in imaging technology and genetic testing may provide a means to obtain improved diagnostics for individual patients, potentially even in an earlier disease stage [53]. Such developments will help clinical decision making and risk stratification, and could also aid in defining better (surrogate) end-points for the evaluation of HF therapy [54]. Fortunately, there is still much to gain for CMR with respect to technological advances that could help improve HF diagnosis. As a result, there is a continuous interest in the development of new MR contrast mechanisms and techniques [55,56]. In particular, CMR might advance the diagnosis of non-ischemic HF by more refined assessment of cardiac morphology and tissue characterization [46,57].

Imaging moves towards applications beyond plain anatomy and function. A plethora of MRI and MRS techniques have been developed for the assessment of various aspects of HF. An example is the development of methods to detect diffuse myocardial fibrosis. Diffuse fibrosis has an important impact on disease progression, but is still difficult to detect using noninvasive imaging readouts [4]. Iles *et al*. showed that more extensive diffuse fibrosis resulted in a decreased post-contrast myocardial T_1 time [55]. With so called spin-lock MRI, $T_1\rho$ contrast is obtained that holds great potential for fibrotic tissue characterization in the infarct [56]. Quantification of T_2 and T_2* in ischemic heart disease provides important information on edema and hemorrhage and T_2 and T_2* may eventually serve as markers for grading disease severity [58]. To obtain insights in cardiac metabolism MRS techniques can be exploited [59]. Phosphorous (^{31}P) MRS provides a unique way to quantify the *in vivo* phosphocreatine (PCr)-to-adenosine triphosphate (ATP) ratio, which is an accepted measure for the energy status of the heart and known to be a good predictor for mortality in dilated cardiomyopathy [9]. Proton (^{1}H) MRS, on the other hand, provides a means to quantify creatine levels as well as lipids important for cardiac metabolism [60]. Diffusion tensor imaging can be used to quantify *ex vivo* and *in vivo* 3D muscle fiber architecture [61-65].

Ultimately, such new readouts could lead to improved diagnostic techniques and risk stratification for HF patients. Here, cardiac MRI in small animal models plays an important role to develop new imaging techniques and assess their potential value for better myocardial tissue characterization in well-defined disease models [66-78].

Heart failure mouse models

The mouse and human heart share remarkable anatomical similarities [79]. Obvious differences are the heart weight in mice and humans (100-200 mg and 250-300 g, respectively) and the heart rate (500-600 min^{-1} and 60-70 min^{-1}, respectively). Other important differences are: the overall shape of the human heart is described as pyramidal, whereas the mouse heart is shaped more ellipsoidal, and the relative size of mouse atria is comparatively small as compared to human atria. Despite these differences, the mouse heart is considered to be a highly relevant model for the study of the human heart. For the aforementioned reasons and the wide availability of well-defined surgical and transgenic models mimicking various aspects of human cardiac diseases, mouse models have become indispensable tools in biomedical research [12].

In this thesis, surgically induced HF mouse models of left ventricular (LV) pressure overload and of myocardial infarction were used. Both models are described below.

A surgically induced constriction of the aorta is frequently used to induce LV pressure overload in mice analogous to systemic hypertension and aortic valve stenosis in patients, as was first described by Rockman *et al.* [80]. Since then, the model has been extensively used to study various facets of pressure overload induced myocardial

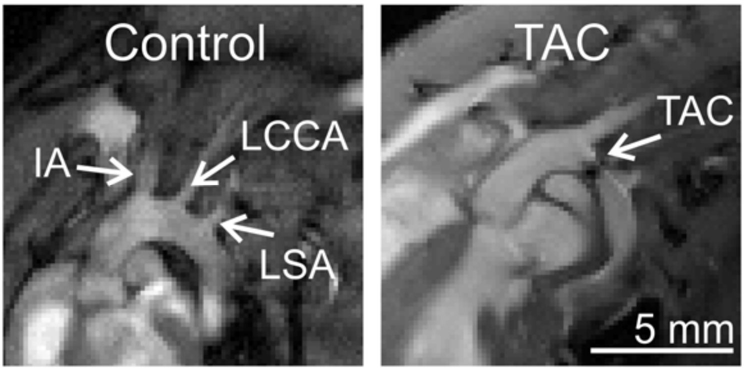

Figure 1.4. MR image of the aortic arch of a control mouse (left) and a TAC mouse (right). Indicated are the innominate artery (IA), the left common carotid artery (LCCA), the left subclavian artery (LSA), and the transverse aortic constriction (TAC).

adaptation [81-89]. The position of the constriction along the aorta and the degree of constriction are major determinants of the time course of the resulting disease progression. Most often a constriction is imposed in between the innominate artery and the left common carotid artery (Figure 1.4), resulting in a severe reduction of the aortic diameter by approximately 60%. The first days after surgery the heart strives to cope with the increased workload [83,84]. After three days hypertrophy is measurable, that can result in partial restoration of cardiac function [90]. Afterwards the hypertrophic growth continues, which leads to a compensated disease stage during the first two weeks. After this period, a progressive decline of cardiac function can occur causing the development of decompensated right ventricular (RV) and LV function and profound lung disease, which eventually will increase mortality [91,92]. On a tissue level, TAC hearts are characterized by diffuse fibrosis and maladaptive vascular and metabolic remodeling. Aortic constriction before the innominate artery results in a faster disease progression, whereas a constriction between both renal arteries typically only results in a moderate degree of hypertrophy [86,93].

A surgically induced permanent occlusion of the left anterior descending (LAD) coronary artery is often used as a relevant model to mimic myocardial infarction (Figure 1.5) [86,94]. The stages of infarct remodeling are characterized by cell death, followed by an inflammation response, the formation of granulation tissue and finally the formation of replacement fibrosis [69]. Typically, thinning of the myocardium is observed already within 48 hours. Collagen deposition can be detected after 1 week and ensues in subsequent weeks during which the scar matures [61]. Infarct size is a primary determinant of the ensuing LV remodeling, which includes progressive LV

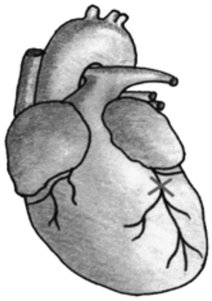

Figure 1.5. Position of the permanent occlusion of the left anterior descending coronary artery of the mouse heart, indicated by the cross. Adapted from Tarnavski *et al.* [86].

dilation, deterioration of LV function and diffuse fibrosis in the surviving myocardium. Eventually, mice may die due to HF or infarct rupture.

Small animal cardiac MRI

CMR involves a number of specific technological challenges, in particular when applied to small animals due to small organ sizes and high heart rates [68,95-97]. In the past, many CMR techniques were therefore first developed for human applications and only later translated to small animal applications for research purposes. However, due to tremendous hardware improvements novel techniques are now often developed for small animal applications first and only then translated for human CMR. To this end, dedicated small animal MRI scanners are used, enabling MRI (Figure 1.6) and MRS with high signal-to-noise ratios, fast image acquisition and excellent spatial (typically 100-200 µm) or spectral resolution. Key to this are high magnetic field strengths, up to 17.6 T for *in vivo* applications, dedicated gradient systems and custom-build RF coils for high sensitivity signal reception.

It is crucial to maintain mouse physiological parameters, such as heart rate, breathing rate and body temperature, within normal range during MR measurements, in particular during measurements of diseased mice as they can comparatively easy become hemodynamicaly unstable when anesthetized [68,95,98]. Tailor made mouse cradles have therefore been developed on which mice are positioned in the isocenter of the MRI scanner (Figure 1.7). During MRI mice need to be anesthetized. Isoflurane is most often used as anesthetic as it has minimal influence on cardiac functional parameters [99]. A rectal temperature sensor is used to measure the mouse temperature, which is maintained at 37 °C with a water-circulated heating pad placed supine on the mouse in this setup. To effectively freeze cardiac motion and prevent severe motion artifacts, the acquisition of the MRI data needs to be strictly synchronized with the mouse heartbeat using ECG triggering. ECG electrodes are therefore incorporated in the animal cradle, which are also vital for monitoring mouse physiology during the MRI exam. Alternatively, self-gated MR sequences can be used [72]. Respiratory motion is conveniently detected with a balloon pressure sensor and used to gate the MR sequence and thereby prevent respiratory motion artefacts.

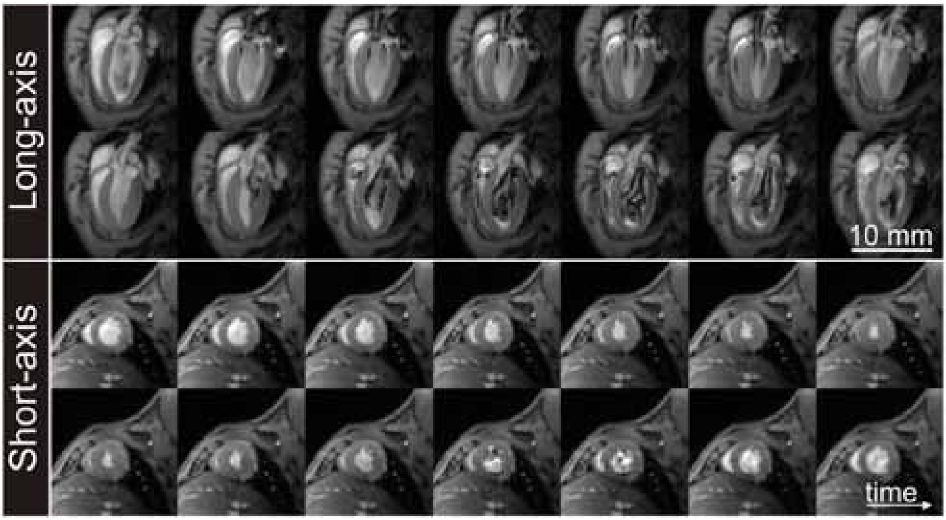

Figure 1.6. Cinematographic MRI obtained in a four-chamber long-axis (top rows) and short-axis orientation (bottom rows) from the same mouse heart. Series of 14 frames were collected during the cardiac cycle with a temporal resolution of 7 ms. The first frame (top left in both collages) was acquired immediately following ECG R-wave detection.

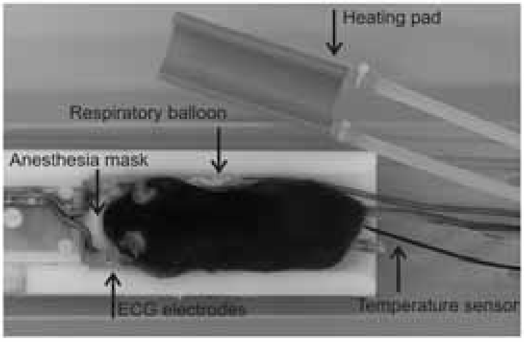

Figure 1.7. A mouse in the animal cradle. The ECG electrodes, respiratory balloon, rectal temperature sensor, anesthesia mask and heating pad are indicated with arrows.

Thesis outline

The **aim** of this thesis was to expand the toolbox of cardiac magnetic resonance techniques for the study of various aspects of mouse HF, in particular to assess: the development of myocardial hypertrophy; longitudinal alterations in myocardial perfusion; the presence of fibrosis; the cardiac energy status.

In **Chapter 2**, longitudinal MR imaging of mouse myocardial function and morphology is described in TAC mouse models of compensated hypertrophy and HF. Cinematographic and tagging MRI were used to characterize the transition from a healthy to a compensated or decompensated state of HF. Vascular adaptation plays an important role in the transition from compensated hypertrophy to HF. In **Chapter 3** a repeatable first-pass perfusion MRI method is described, based on a dual-bolus approach, to quantify regional mouse myocardial perfusion values (in mL min^{-1} g^{-1}) using a rapid imaging sequence and a Fermi constrained deconvolution model. In **Chapter 4** this method was used to study the relationship between myocardial perfusion and LV function and morphology in TAC mice. Current diagnostic tools for diffuse myocardial fibrosis are limited. In **Chapter 5**, proof-of-principle *ex vivo* and *in vivo* ultra short echo time (UTE) MRI measurements are described for the imaging of replacement and diffuse fibrosis. In **Chapter 6**, the phosphocreatine-to-adenosine triphosphate ratio (PCr/ATP) was quantified *in vivo* as a measure for myocardial energy status in the healthy and TAC mouse heart using a 3D Image Selected *In vivo* Spectroscopy (ISIS) method for single-voxel localized ^{31}P-MR spectroscopy. In a next study, described in **Chapter 7**, PCr/ATP was quantified at the day of TAC and four days thereafter. Moreover, the hypothesis was tested that early changes in PCr/ATP can be used as a marker to predict subsequent adverse remodeling, which was monitored using the cinematographic MRI technique. The thesis is concluded with a summarizing discussion in **Chapter 8** describing the main findings of this work, and providing an overview of future perspectives for cardiac magnetic resonance techniques and their application for diagnosis and risk stratification of HF patients.

References

1. Guyton, A.C., Hall J.E. Textbook of Medical Physiology. Philadelphia, Pennsylvania: Elsevier Saunders, 2006.
2. Berk, B.C., et al. *J Clin Invest,* 2007, **117**(3), 568-75.
3. Creemers, E.E., Pinto Y.M. *Cardiovasc Res,* 2011, **89**(2), 265-72.
4. Mewton, N., et al. *J Am Coll Cardiol,* 2011, **57**(8), 891-903.
5. Hinz, B., et al. *Am J Pathol,* 2007, **170**(6), 1807-16.
6. Braunwald, E. *Am J Cardiol,* 1971, **27**(4), 416-32.
7. Delaye, J., et al. *Arch Mal Coeur Vaiss,* 1983, **76**(SI), 7-12.
8. Johnson, P.C. *Circ Res,* 1986, **59**(5), 483-95.
9. Neubauer, S. *N Engl J Med,* 2007, **356**(11), 1140-51.
10. Ingwall, J.S., Weiss R.G. *Circ Res,* 2004, **95**(2), 135-45.
11. Denolin, H., et al. *Eur Heart J,* 1983, **4**(7), 445-8.
12. Houser, S.R., et al. *Circ Res,* 2012, **111**(1), 131-50.
13. Levy, D., et al. *N Engl J Med,* 2002, **347**(18), 1397-402.
14. Roger, V.L., et al. *Circulation,* 2011, **123**(4), e18-e209.
15. Ho, K.K., et al. *Circulation,* 1993, **88**(1), 107-15.
16. McMurray, J.J., Stewart S. *Heart,* 2000, **83**(5), 596-602.
17. Lloyd-Jones, D., et al. *Circulation,* 2010, **121**(7), e46-e215.
18. McMurray, J.J.V., Pfeffer M.A. *Lancet,* 2005, **365**(9474), 1877-89.
19. Schou, M., et al. *Eur Heart J,* 2012, doi: 10.1093/eurheartj/ehs235.
20. Berry, C., et al. *Eur J Heart Fail,* 2001, **3**(3), 283-91.
21. Hunt, S.A., et al. *Circulation,* 2009, **119**(14), e391-e479.
22. Frey, N., Olson E.N. *Annu Rev Physiol,* 2003, **65**, 45-79.
23. Frey, N., et al. *Circulation,* 2004, **109**(13), 1580-9.
24. Cacciapuoti, F. *J Am Soc Hypertens,* 2011, **5**(6), 449-55.
25. Hill, J.A., Olson E.N. *N Engl J Med,* 2008, **358**(13), 1370-80.
26. Grossman, W., et al. *J Clin Invest,* 1975, **56**(1), 56-64.
27. Cokkinos, D.V., Pantos C. *Heart Fail Rev,* 2011, **16**, 1-4.
28. Díez, J. *J Clin Hypertens (Greenwich),* 2007, **9**(7), 546-50.
29. Houweling, A.C., et al. *Cardiovasc Res,* 2005, **67**(4), 583-93.
30. Hoenig, M.R., et al. *Curr Vasc Pharmacol,* 2008, **6**(4), 292-300.
31. Dai, Z., et al. *J Cardiol,* 2012, **60**(5), 416-21.
32. Duncker, D.J., et al. *Med Biol Eng Comput,* 2008, **46**(5), 485-97.
33. Shiojima, I., et al. *J Clin Invest,* 2005, **115**(8), 2108-18.
34. Mathiassen, O.N., et al. *J Hypertens,* 2007, **25**(5), 1021-6.
35. Petersen, S.E., et al. *Circulation,* 2007, **115**(18), 2418-25.
36. Ingwall, J.S. *Cardiovasc Res,* 2009, **81**(3), 412-9.
37. Beer, M., et al. *J Am Coll Cardiol,* 2002, **40**(7), 1267-74.
38. Neubauer, S., et al. *Circulation,* 1997, **96**(7), 2190-6.
39. Gupta, A., et al. *Am J Physiol Heart Circ Physiol,* 2009, **297**(1), H59-H64.
40. Holloway, C., Clarke K. *Heart Lung Circ,* 2010, **19**(3), 154-60.
41. Pohost, G.M. *J Am Coll Cardiol Img,* 2008, **1**(5), 672-8.
42. Lima, J.A., Desai M.Y. *J Am Coll Cardiol,* 2004, **44**(6), 1164-71.
43. Alfayoumi, F., et al. *Rev Cardiovasc Med,* 2007, **8**(3), 135-44.
44. Constantine, G., et al. *Lancet,* 2004, **363**(9427), 2162-71.
45. Atalay, M.K. *J Am Coll Radiol,* 2005, **2**(9), 740-8.
46. To, A.C., Desai M.Y. *Expert Rev Cardiovasc Ther,* 2012, **10**(2), 223-33.
47. Attili, A.K., et al. *Int J Cardiovasc Imaging,* 2010, **26 Suppl 1**, 27-40.
48. Finn, J.P., et al. *Radiology,* 2006, **241**(2), 338-54.

49. Al-Mallah, M.H., Shareef M.N. *Heart Fail Rev,* 2011, **16**(4), 369-80.
50. Stillman, A.E. *J Am Coll Radiol,* 2007, **4**(4), 224-6; discussion 7-8.
51. Kaufmann, P.A., Di Carli M.F. *Semin Nucl Med,* 2009, **39**(5), 341-7.
52. Majmudar, M.D., Nahrendorf M. *J Nucl Med,* 2012, **53**(5), 673-6.
53. Wollert, K.C. *Eur Heart J,* 2012, **33**(18), 2246-8.
54. Shehata, M.L., et al. *Top Magn Reson Imaging,* 2008, **19**(1), 43-57.
55. Iles, L., et al. *J Am Coll Cardiol,* 2008, **52**(19), 1574-80.
56. Witschey, W.R., et al. *J Cardiovasc Magn Reson,* 2012, **14**, 37.
57. De Smet, K., et al. *Eur J Radiol,* 2012, **81**(7), 1546-8.
58. Zia, M.I., et al. *Circ Cardiovasc Imaging,* 2012, **5**(5), 566-72.
59. Jameel, M.N., Zhang J. *Curr Cardiol Rev,* 2009, **5**(3), 243-50.
60. Faller, K.M., et al. *Heart Fail Rev,* 2012, doi: 10.1007/s10741-012-9341-z.
61. Strijkers, G.J., et al. *NMR Biomed,* 2009, **22**(2), 182-90.
62. Strijkers, G.J., et al. *Israel J of Chem,* 2003, **43**, 71-80.
63. Huang, S., et al. Proc Intl Soc Mag Reson Med, Stockholm, Sweden, 2010, 488.
64. Nielles-Vallespin, S., et al. *Magn Reson Med,* 2012, doi: 10.1002/mrm.24488.
65. Sosnovik, D.E., et al. *J Cardiovasc Magn Reson,* 2009, **11**, 47.
66. Coolen, B.F., et al. *NMR Biomed,* 2011, **24**(2), 154-62.
67. Coolen, B.F., et al. *Magn Reson Med,* 2010, **64**(6), 1658-63.
68. Coolen, B.F., et al. *NMR Biomed,* 2012, **25**(8), 969-84.
69. Geelen, T., et al. *NMR Biomed,* 2012, **25**(8), 953-68.
70. Makowski, M., et al. *Magn Reson Med,* 2010, **64**(6), 1592-8.
71. Sosnovik, D.E., et al. *Circ Cardiovasc Imaging,* 2009, **2**(6), 460-7.
72. Heijman, E., et al. *NMR Biomed,* 2007, **20**(4), 439-47.
73. Dall'armellina, E., et al. *Magn Reson Med,* 2012, **67**(2), 541-51.
74. Bakermans, A.J., et al. *Circ Cardiovasc Imaging,* 2011, **4**(5), 558-65.
75. Coolen, B.F., et al. *J Cardiovasc Magn Reson,* 2011, **13**, 56.
76. Aguor, E.N., et al. *Int J Cardiovasc Imaging,* 2012, doi: 10.1007/s10554-012-0093-6.
77. van Nierop, B.J., et al. *Magn Reson Med,* 2012, doi: 10.1002/mrm.24424.
78. Epstein, F.H., et al. *Magn Reson Med,* 2002, **47**(3), 482-91.
79. Wessels, A., Sedmera D. *Physiol Genomics,* 2003, **15**(3), 165-76.
80. Rockman, H.A., et al. *Proc Natl Acad Sci U S A,* 1991, **88**(18), 8277-81.
81. Givvimani, S., et al. *J Appl Physiol,* 2011, **110**(4), 1093-100.
82. van Deel, E.D., et al. *J Mol Cell Cardiol,* 2011, **50**(6), 1017-25.
83. Lygate, C. *Drug Discov Today Dis Models,* 2006, **3**(3), 283-90.
84. Lygate, C.A., et al. *Basic Res Cardiol,* 2006, **101**(1), 8-16.
85. van Nierop, B.J., et al. *PLoS ONE,* 2013, **8**(2), e55424.
86. Tarnavski, O., et al. *Physiol Genomics,* 2004, **16**(3), 349-60.
87. deAlmeida, A.C., et al. *J Vis Exp,* 2010, doi: 10.3791/1729.
88. Hartley, C.J., et al. *Ultrasound Med Biol,* 2008, **34**(6), 892-901.
89. Qu, J., et al. *Circ Res,* 2009, **104**(3), 365-71.
90. Souders, C.A., et al. *Am J Pathol,* 2012, **181**(4), 1226-35.
91. Chen, Y., et al. *Hypertension,* 2012, **59**(6), 1170-8.
92. Berry, J.M., et al. *Drug Discov Today Dis Models,* 2007, **4**(4), 197-206.
93. Higashiyama, H., et al. *Int J Exp Pathol,* 2007, **88**(1), 31-8.
94. van den Borne, S.W.M., et al. *Cardiovasc Res,* 2009, **84**(2), 273-82.
95. Schneider, J.E., et al. *J Cardiovasc Magn Reson,* 2006, **8**(5), 693-701.
96. Scott, A.D., et al. *Radiology,* 2009, **250**(2), 331-51.
97. Nahrendorf, M., et al. *Med Image Anal,* 2003, **7**(3), 369-75.
98. Kass, D.A., et al. *Circ Res,* 1998, **82**(4), 519-22.
99. Roth, D.M., et al. *Am J Physiol Heart Circ Physiol,* 2002, **282**(6), H2134-H40.

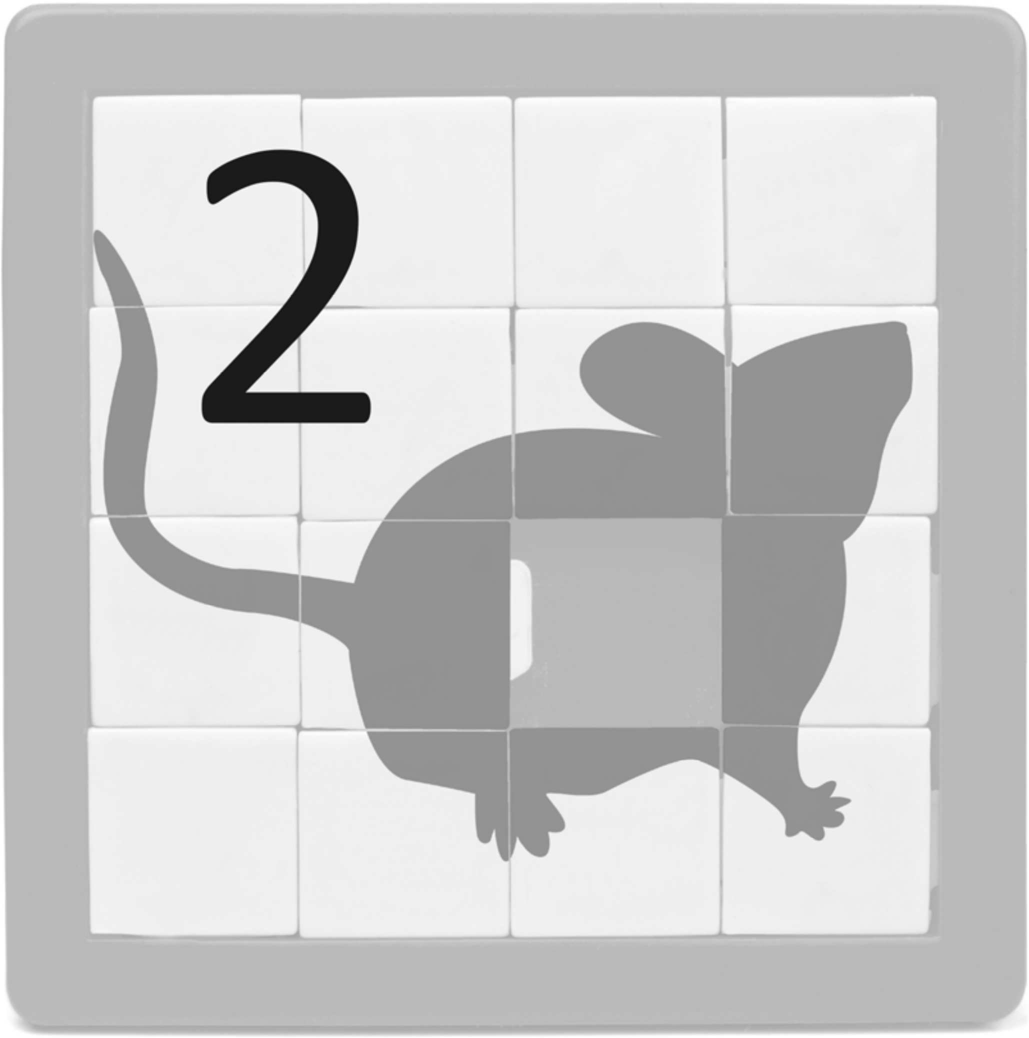

2

Phenotyping of left and right ventricular function in mouse models of compensated hypertrophy and HF with cardiac MRI

Bastiaan van Nierop, Hans van Assen, Elza van Deel,
Leonie Niesen, Dirk Duncker, Gustav Strijkers,
and Klaas Nicolay

Based on: Plos ONE, **2013**, DOI: 10.1371/journal.pone.0055424

Abstract

Background: Left ventricular (LV) and right ventricular (RV) function have an important impact on symptom occurrence, disease progression and exercise tolerance in pressure overload-induced heart failure, but particularly RV functional changes are not well described in the relevant aortic banding mouse model. Therefore, we quantified time-dependent alterations in the ventricular morphology and function in two models of hypertrophy and heart failure and we studied the relationship between RV and LV function during the transition from hypertrophy to heart failure.

Methods: MRI was used to quantify RV and LV function and morphology in healthy (n = 4) and sham operated (n = 3) C57BL/6 mice, and animals with a mild (n = 5) and a severe aortic constriction (n = 10).

Results: Mice subjected to a mild constriction showed increased LV mass ($P < 0.01$) and depressed LV ejection fraction (EF) ($P < 0.05$) as compared to controls, but had similar RVEF ($P > 0.05$). Animals with a severe constriction progressively developed LV hypertrophy ($P < 0.001$), depressed LVEF ($P < 0.001$), followed by a declining RVEF ($P < 0.001$) and the development of pulmonary remodeling, as compared to controls during a 10-week follow-up. Myocardial strain, as a measure for local cardiac function, decreased in mice with a severe constriction compared to controls ($P < 0.05$).

Conclusion: Relevant changes in mouse RV and LV function following an aortic constriction could be quantified using MRI. The well-controlled models described here, open opportunities to assess the added value of new MRI techniques for the diagnosis of heart failure and to study the impact of new therapeutic strategies on disease progression and symptom occurrence.

Introduction

Heart failure (HF) is a progressive syndrome in which the heart is no longer capable of pumping blood at a rate commensurate with the peripheral needs [1]. HF is an important cause of morbidity and mortality worldwide and results in a significant decrease in the quality of life [2-4]. In many patients HF results from sustained, systemic hypertension accompanied by a pressure overload of the left ventricle (LV) [5]. The heart initially adapts to this overload by means of hypertrophic growth. However, a broad range of concomitant maladaptive processes, including myocardial fibrosis, metabolic changes and a decreasing capillary density, eventually lead to HF [6-8].

Despite considerable progress, the mechanisms responsible for the transition from compensated hypertrophy to HF are still not completely understood [9]. In particular, the role of the right ventricle (RV) long received comparatively little attention as compared to the LV in research on various cardiac pathologies. Recently, however, there is growing awareness that RV function has an important impact on disease progression, symptom occurrence and exercise tolerance in HF patients [10,11].

The goal of this study was therefore twofold. First, to quantify longitudinal changes in LV and RV morphology as well as function during the transition from a healthy to a compensated or decompensated state of LV hypertrophy. Second, to investigate the interplay between LV and RV function during this process.

Here, the well-defined, reproducible mouse model of transverse aorta constriction (TAC) can play a prominent role [12]. Currently there is a lack of information on the long-term changes in RV function and its relation with deteriorating LV function in this model. Therefore, mice were studied with cardiac MRI both in a compensated stage of cardiac hypertrophy resulting from a mild TAC and during the transition towards a stage of HF after application of a severe TAC [13].

Methods

Ethics Statement

All animal experiments were performed according to the Directive 2010/63/EU of the European Parliament and approved by the Animal Care and Use Committee of Maastricht University.

Animal model

In this study C57BL/6 mice (♂, age 11 weeks, 23-25 grams) were used. Animals were housed under standard laboratory conditions with a 12 h light/dark cycle and were maintained on a standard diet and had access to water *ad libitum*.

For MRI a total of 22 animals were randomly separated in a control group (n = 4), a group that was sham-operated (n = 3) and in two groups which underwent a surgically induced mild (n = 5) or severe (n = 10) transverse aortic constriction (TAC), resulting in LV pressure overload [12,13]. Briefly, mice were anesthetized with 2.5 vol% isoflurane in 0.2 L min^{-1} O_2 and 0.2 L min^{-1} medical air and intubated for mechanical ventilation. Animals were placed on a heating pad to maintain body temperature at 37 °C. Buprenorphine (0.1 mg/kg s.c.) was administered for analgesia. Surgical procedures were performed using a stereo microscope (Leica M80). A small incision was made just lateral from the sternum above the first intercostal space. The aortic arch was exposed and tied off (6-0 silk suture) together with a 25G (Ø 0.50 mm) or 27G (Ø 0.42 mm) needle between the innominate artery and the left common carotid artery to induce a mild or severe TAC, respectively. The needle was immediately removed, restoring blood flow. The chest was then closed and the animals were allowed to recover in a 30 °C recovery chamber. The sham-operation was identical, but without tightening of the ligation.

MR examinations

Measurements were performed with a 9.4 T small animal MRI scanner (Bruker BioSpec, Ettlingen, Germany) equipped with a 740 mT/m gradient coil. A 72-mm-diameter quadrature transmit coil was used in combination with a 4 element phased-array receive coil (Bruker). Mice were anesthetized with isoflurane (4.0 vol% for induction, 1.5-2.0 vol% for maintenance) in medical air (0.4 L min^{-1}). The front paws were placed on ECG electrodes and a balloon pressure sensor was placed on the abdomen. Body temperature was maintained at 36-37 °C with a heating pad and monitored with a rectal temperature sensor.

Cinematographic (cine) MR images were acquired using an ECG-triggered and respiratory-gated FLASH sequence, with the following parameters: pulse repetition time (TR) = 7 ms, echo time (TE) = 1.8 ms, number of signal averages = 6, α = 15, field of view = 3x3 cm^2, matrix = 192x192, slice thickness = 1 mm, number of cardiac frames = 15-20. Measurements were performed in 2 long-axis and 5 short-axis planes, covering the LV from apex to base with interslice distance optimized for heart size.

Local cardiac function was measured from mid-ventricular short-axis tagged images. Tagging MRI was done using the FLASH sequence with a spatial modulation of magnetization (SPAMM) preparation module resulting in a sinusoidal modulation of magnetization that moves along with the cardiac tissue during the heart cycle. The preparation consisted of two Gaussian RF pulses (α = 45°, pulse width = 200 μs), separated by a gradient (duration = 200 μs) defining tag wavelength (0.5 mm) and orientation. Total duration of the preparation module was 2.7 ms. Tagged images were recorded with a reduced matrix of 192x96 (frequency x phase encoding) and reconstructed on a 384x384 matrix for data analysis. Tags were applied in horizontal and vertical directions and with 180^{o} phase shift for complementary SPAMM (CSPAMM) reconstruction [14]. Total examination time was approximately 2 hours.

Study protocol

MRI measurements were performed at 1, 2, 4, 7, 10 and 13 weeks after surgery. Cine MR images were obtained at all time points. During the first MRI experiment cine MR images of the aortic arch were acquired to confirm correct positioning of the TAC (Figure 2.1).

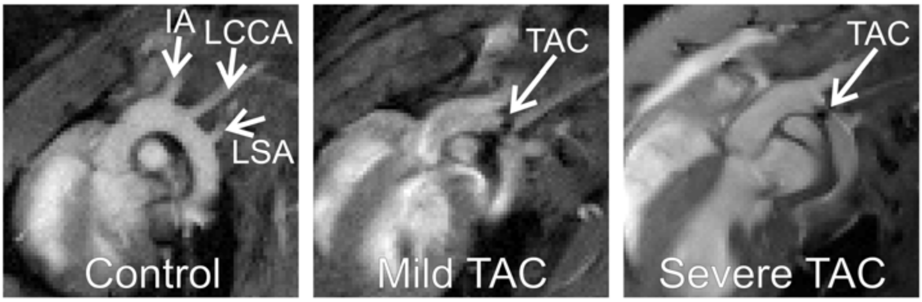

Figure 2.1. Examples of MRI scans through the aortic arch in (left) a control, (middle) mild TAC and (right) severe TAC mouse. Indicated are (IA) the innominate artery, (LCCA) left common carotid artery, (LSA) left subclavian artery, and the transverse aortic constriction (TAC).

Tagged MR images were obtained at week 2 until week 10, at which time points all animals were in experiment, to determine the relationship between local strain changes and global cardiac morphology and function. Mice with a severe TAC were euthanized 10 weeks after surgery for animal welfare reasons. Immediately after the last measurements the anesthetized animals were killed by means of perfusion of the vascular bed with phosphate buffered saline (10 mL, pH 7.4) infused via a needle penetrating the apex and exsanguination from the vena cava inferior. Next, the integrity of the aortic band was visually verified and lung wet weight (LuW) and tibia length (TL) were measured.

Data analysis

The myocardial wall was segmented semi-automatically in the cine MR images using CAAS MRV FARM (Pie Medical Imaging, The Netherlands) to obtain LV and RV volumes, and the LV and RV ejection fractions (EF) [15,16]. Papillary muscles were excluded from the lumen. Wall thickening (WT) was defined as the percentage increase in wall thickness from end-diastole to end-systole. LV mass was calculated from end-diastolic myocardial volume using a tissue density of 1.04 g/cm^3 and was normalized to TL to obtain an independent measure of hypertrophy [17]. Pulmonary remodeling and edema were evaluated from the LuW/TL ratio and lung wet weight-to-dry weight ratio (ww/dw), respectively [18].

Local tissue motion was quantified from the tagged images using a method based on optical flow theory implemented in Mathematica 7.0 (Wolfram Research Inc., Champaign, IL) [19]. Briefly, the 180° phase shifted tagged images were subtracted from their complementary counterparts to obtain CSPAMM images. The phase of the tagging pattern was extracted by spectral filtering of the 1st harmonic peak in k-space, using a Gabor filter bank [20]. Next, myocardial tissue displacements were computed from the extracted phases of the two time-series of orthogonal CSPAMM images, by solving a multi-scale version of the optical flow constraint equation. Finally, principal strains E1 and E2 were determined as read-out parameters for tissue deformation, as they report on radial wall thickening and circumferential wall shortening, respectively [21,22]. Strains were determined in end-systole with end-diastole as a reference. Strain analysis was performed in 4 segments according to AHA standards [23].

Statistics

Data are expressed as mean ± standard deviation (SD). Changes in LV and RV volumes and EF, LV mass/TL, heart rate, respiratory rate, bodyweight (BW), WT and strains were tested for statistical significance with an ANOVA for repeated measures with time and group as factor, followed by the Bonferroni post-hoc test when appropriate. In case of interaction between time and group, the effect of time was tested separately per group. Changes in LuW/TL and heart weight/TL were tested for statistical significance with a one-way ANOVA, followed by the Bonferroni post-hoc test. For survival analysis additional data from healthy (n = 48), mild TAC (n = 2) and severe TAC mice (n = 89) available from our laboratory was included. Differences between Kaplan-Meier survival curves were tested for statistical significance by means of Log Rank analysis. Calculations were performed using SPSS 19.0 (SPSS Inc., Chicago). For all tests the level of significance was set at $\alpha = 0.05$.

Results

Experimental groups

Survival analysis performed on a large cohort of mice (Figure 2.2) showed a significant difference (*P* = 0.02) in survival rate of the severe TAC mice, as compared to the control and mild TAC mice. In particular, all animals that underwent MRI in the control, sham-operated and the mild TAC group completed the experimental protocol. Possible differences in cardiac function or morphology between control and sham-operated mice were assessed in terms of LVEF and LV mass/TL (data not shown). No significant differences were detected (*P* = 0.25 and *P* = 0.76, respectively). Therefore, data of control and sham-operated groups were pooled for further analyses. One mouse with a severe TAC died within 60 min after surgery. The other animals recovered well from surgery. In this group, three mice died in the period 4-10 weeks after surgery, presumably due to acute decompensated HF or arrhythmias.

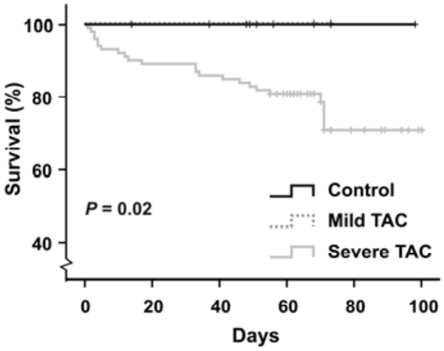

Figure 2.2. Kaplan-Meier analysis was performed based on survival data of a large cohort of healthy mice (n = 55), mild TAC (n = 5) and severe TAC mice (n = 99) available from our laboratory. Log Rank analysis showed a significant difference in survival between the severe TAC mice as compared to the control and mild TAC mice (P = 0.02).

Table 2.1 lists general physiological parameters for the experimental groups. No significant changes over time or differences between groups were detected for heart rate and respiratory rate. BW increased significantly during the course of the experiment (*P* < 0.001), but no significant differences between groups were detected. BW in the severe TAC group displayed a decreasing trend at 10 weeks, but this was not statistically significant as compared to 7 weeks after surgery (*P* = 0.91).

Impaired LV function and hypertrophy

Figure 2.3A shows representative short-axis and long-axis cine MR images obtained in the different experimental groups 10 weeks after surgery. Increased wall thickness was observed in all mice subjected to TAC, while apical aneurysms were only noted in severe TAC.

Table 2.1. General characteristics of the control animals and mice with a mild and severe constriction. Indicated are the time points relative to the time of surgery (weeks), the heart rate (HR) (min^{-1}) and respiratory rate (Resp) (min^{-1}) during the MR examination, and the body weight (BW) (g).

	Weeks	**1**	**2**	**4**	**7**	**10**	**13**
HR (min^{-1})	Control	528 ± 29	532 ± 30	524 ± 33	532 ± 28	534 ± 34	536 ± 21
	mTAC	-	520 ± 30	544 ± 30	547 ± 35	560 ± 48	556 ± 41
	sTAC	600 ± 31	592 ± 51	529 ± 61	530 ± 31	561 ± 33	-
Resp (min^{-1})	Control	74 ± 6	86 ± 23	89 ± 8	90 ± 10	90 ± 12	89 ± 9
	mTAC	-	82 ± 17	77 ± 9	81 ± 17	74 ± 16	95 ± 14
	sTAC	110 ± 15	88 ± 9	81 ± 18	89 ± 12	87 ± 12	-
BW (g)	Control	24.4 ± 0.8	25.4 ± 1.3	26.0 ± 1.2	27.0 ± 1.3	27.8 ± 1.6	28.9 ± 1.8
	mTAC	-	26.9 ± 2.2	27.6 ± 2.4	28.0 ± 2.0	29.6 ± 1.7	28.4 ± 0.9
	sTAC	24.5 ± 0.9	25.2 ± 1.1	26.5 ± 1.2	27.3 ± 1.2	25.8 ± 0.7	-

Mice with a mild TAC revealed a small increase of LV mass normalized to TL (5.4 ± 0.7 mg/mm) as compared to controls (3.9 ± 0.4 mg/mm, $P < 0.01$) (Figure 2.4). In these animals, a mild impairment of systolic function was apparent from a depressed LVEF (53 ± 10%) as compared to controls (64 ± 6%, $P < 0.05$), a trend towards increased LV end-diastolic volume (EDV) (69 ± 23 µL) as compared to controls (44 ± 5 µL, $P = 0.06$) and a slightly increased LV end-systolic volume (ESV) (35 ± 19 µL) as compared to controls (16 ± 4 µL, $P = 0.05$) (Figure 2.5). LV mass, EDV, ESV and EF did not change significantly over time in both groups.

In contrast, severe TAC resulted in a progressive increase of LV mass normalized to TL from 5.8 ± 0.6 mg/mm in week 2 to 9.1 ± 0.5 mg/mm in week 10 ($P < 0.001$). As a result of the high pressure overload a significant reduction in EF (36 ± 7%, $P < 0.001$) was apparent by week 1. No further deterioration of EF occurred between 1 and 2 weeks after surgery ($P = 1.00$). At later time points EF gradually decreased to 18 ± 5% in week 10 ($P < 0.001$). EDV and ESV remained virtually constant between week 1 and 2, but progressively increased afterwards ($P < 0.001$). In addition, starting from 4 weeks after surgery akinesia of the apex was detected in a subset of the severe TAC group (n = 3) (black arrow, Figure 2.3A) accompanied by apical aneurysms of the LV wall. Akinesia was quantified in terms of WT (Figure 2.3B).

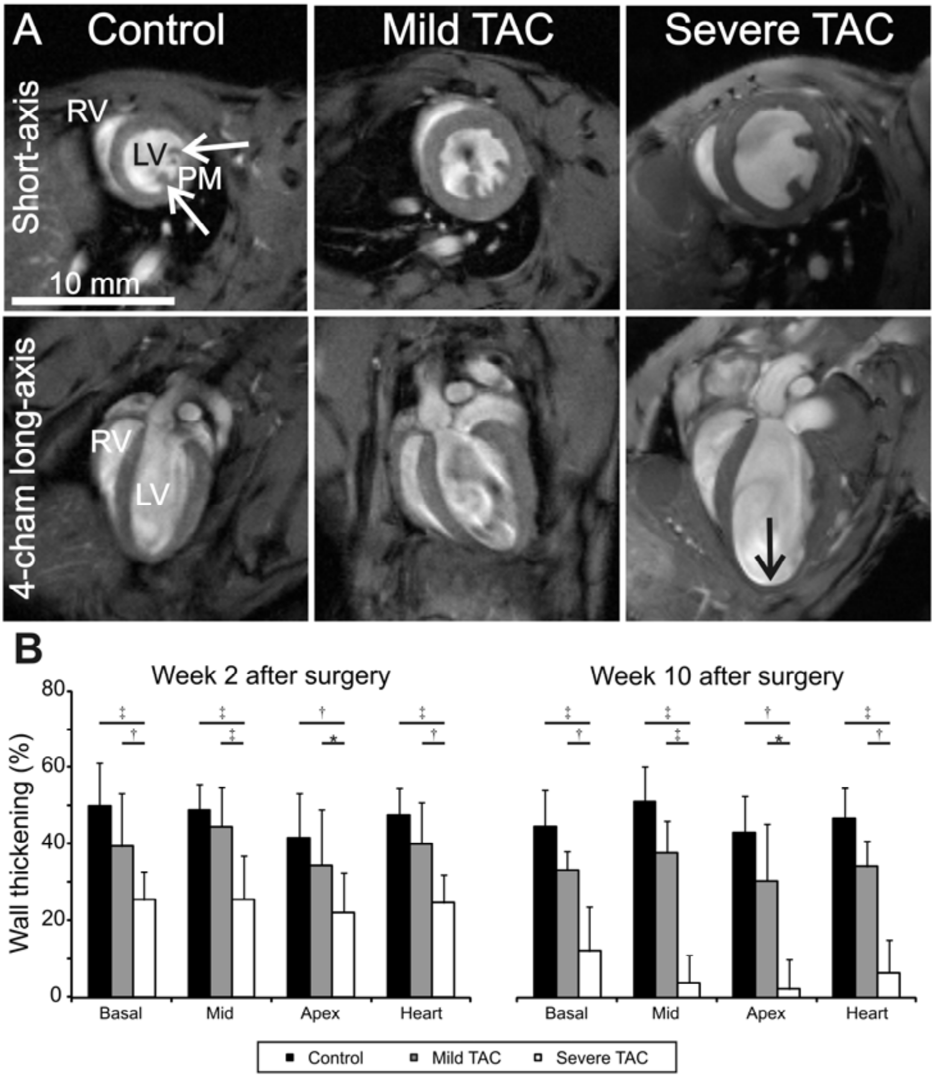

Figure 2.3. (A) Representative end-diastolic short-axis and long-axis images from control mice and mice subjected to a mild and severe aortic constriction 10 weeks after surgery. Indicated are the left ventricle (LV), right ventricle (RV), the papillary muscles (PM) and decreased apical wall thickness in the mouse with a severe TAC (↓). (B) Wall thickening (WT) in the experimental groups at 2 and 10 weeks after surgery. At 2 weeks, WT had decreased in all sections of the heart in mice with a severe TAC as compared to controls ($P < 0.01$ in all cases), but the decrease in mild TAC mice did not reach statistical significance. At 2 weeks, WT in the animals with a mild constriction was significantly different from the mice with a severe constriction in all portions of the heart ($P < 0.05$, in all cases). No significant changes over time were detected in the control and mild TAC mice, whereas WT decreased in all portions of the severe TAC hearts ($P < 0.05$, in all cases).

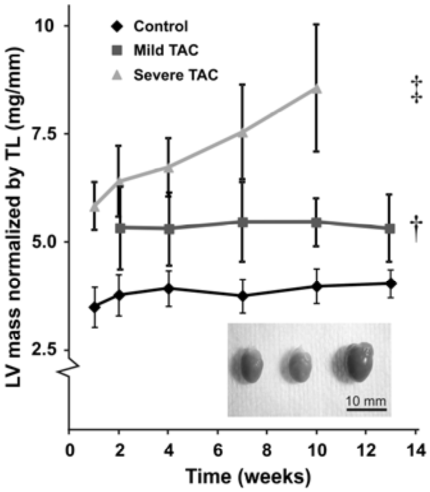

Figure 2.4. LV mass normalized to tibia length (TL) in control, mild and severe TAC mice as a function of time. Cardiac mass slightly increased in response to a mild constriction as compared to controls (*, $P < 0.05$) and progressively increased in response to a severe constriction (‡, $P < 0.001$). Mean and SD per time point are denoted by the corresponding symbol and error bars. The inset shows a photograph of (left) a control, (middle) mild TAC and (right) severe TAC heart 10 weeks (severe TAC) and 13 weeks (control and mild TAC) after surgery.

Impaired RV function and lung remodeling

Impaired LV function may induce lung remodeling and/or edema and subsequently RV failure [10]. Therefore, RV EDV, ESV and EF were also quantified over time (Figure 2.5). RVEF progressively decreased from 56 ± 10% to 18 ± 11% ($P < 0.001$) and RV ESV increased from 12 ± 2 µL to 44 ± 12 µL ($P < 0.001$) in mice with a severe TAC. In contrast, RVEF in mild TAC animals (66 ± 9%) was not depressed as compared to controls (72 ± 5%), and RV EDV (42 ± 8 µL) and ESV (14 ± 5 µL) in mild TAC animals remained unchanged as compared to RV EDV (41 ± 6 µL) and ESV (12 ±3 µL) in controls ($P > 0.05$ in all cases).

Figure 2.6 shows the relationship between RV and LVEF for all mice. RVEF was merely affected in the severe TAC mice and was preceded by a change in LVEF. This became apparent from a shift of the majority of the measurement points to the left in Figure 2.6, indicating that LVEF decreased first before deterioration of RVEF. Finally, pulmonary remodeling (Table 2.2) was observed in the severe TAC group when the mice were euthanized, indicated by an increased LuW/TL ratio as compared to controls and mild TAC ($P < 0.01$), but no increase in lung water content was observed, indicated by the lung wet weight-to-dry weight ratio.

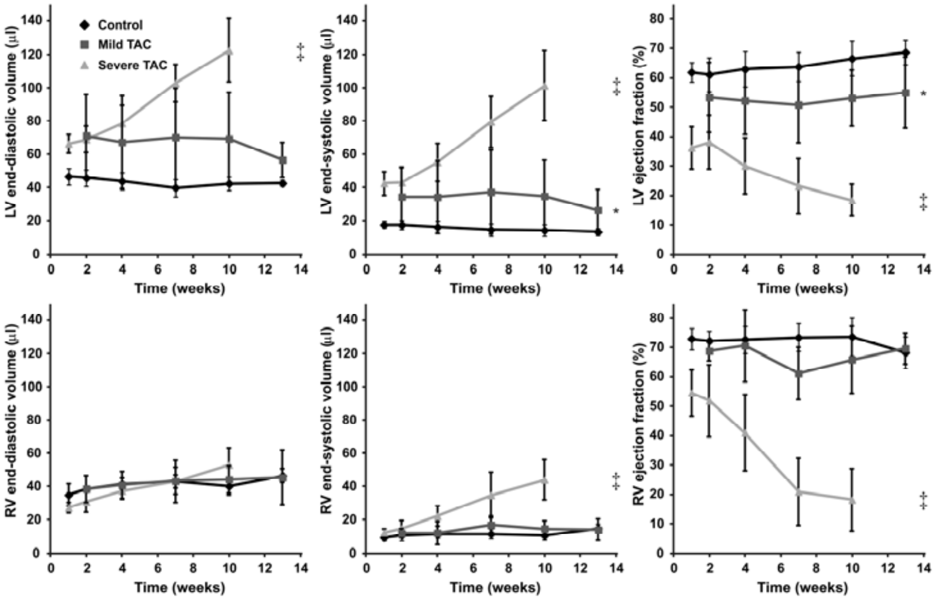

Figure 2.5. End-diastolic volume in control, mild and severe TAC mice (left column), end-systolic volume (middle column) and ejection fraction (right column) as a function of time for both the left ventricle (LV) (top row) and right ventricle (RV) (bottom row). End-diastolic and end-systolic volumes clearly show LV and RV dilation in the severe TAC mice, but not in the mild TAC mice as compared to the control animals. LV ejection fraction was slightly depressed in response to a mild constriction as compared to controls, and showed a progressive decline in time in the group with a severe constriction. RV ejection fraction remained unchanged in mice with a mild constriction of the aorta as compared to control mice, but showed a progressive decline in case of a severe aortic constriction. Mean and SD per time point are denoted by the corresponding symbol and error bars. Statistical differences as compared to the control group are indicated by * ($P < 0.05$) and ‡ ($P < 0.001$).

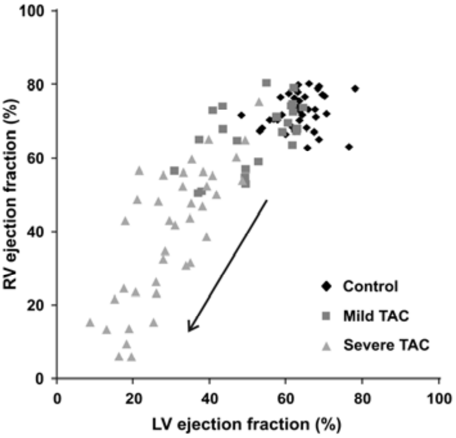

Figure 2.6. Relationship between left (LV) and right ventricular (RV) ejection fraction for all mice at all time points. The RV ejection fraction progressively decreased (black arrow) in the severe TAC group only and the changes in RV ejection fraction were preceded by a decline in LV ejection fraction apparent from the shift of the majority of the measurement points to the left.

Table 2.2. An increased lung weight-to-tibia length (LuW/TL) ratio (mg/mm) indicated the presence of pulmonary remodeling in the mice with a severe constriction, but not in the mice with a mild constriction. No differences between groups were observed in the lung water content, indicated by the absence of significant differences in the lung wet weight-to-dry weight ratio (ww/dw). Post mortem whole heart weight-to-tibia length ratio was significantly increased in severe TAC mice, but the increase in the mild TAC mice did not reach statistical significance.

Group	LuW/TL (mg/mm)	ww/dw (-)	HW/TL (mg/mm)
Control	9.4 ± 1.5	6.1 ± 0.6	7.9 ± 0.5
Mild TAC	10.4 ± 2.0	6.8 ± 1.8	10.3 ± 2.1
Severe TAC	17.5 ± 4.8†	5.6 ± 0.7	13.6 ± 2.3‡

Statistical differences as compared to the control group are indicated by † ($P < 0.01$) and ‡ ($P < 0.001$).

Myocardial principal strains

Figure 2.7 shows an example of an end-diastolic short-axis image (A) and corresponding tagged images in end-diastole (B) and end-systole (C) in a mouse with a severe TAC 10 weeks after surgery. Myocardial principal strains E1 and E2 were determined as read-out parameters for radial wall thickening and circumferential wall shortening, respectively. Analysis of the principal strains in the four segments (see Figure 2.7A) revealed no marked, regional differences between groups (data not shown), and were therefore reported for the myocardium as a whole.

Figure 2.7D shows that radial wall thickening and circumferential wall shortening were identical between the control (0.12 ± 0.03 and -0.10 ± 0.02, respectively) and mild TAC mice (0.12 ± 0.02 and -0.11 ± 0.02, respectively). Moreover, no effects of time were observed. In contrast, radial wall thickening was significantly decreased in the mice with a severe TAC as compared to control mice ($P < 0.001$) and showed a decrease from 0.09 ± 0.02 in week 2 to 0.06 ± 0.01 in week 10 ($P < 0.05$). Circumferential wall shortening was also significantly decreased in mice with a severe TAC as compared to control mice ($P < 0.01$) and showed a decrease from -0.09 ± 0.01 in week 2 to -0.06 ± 0.01 in week 10 ($P < 0.05$).

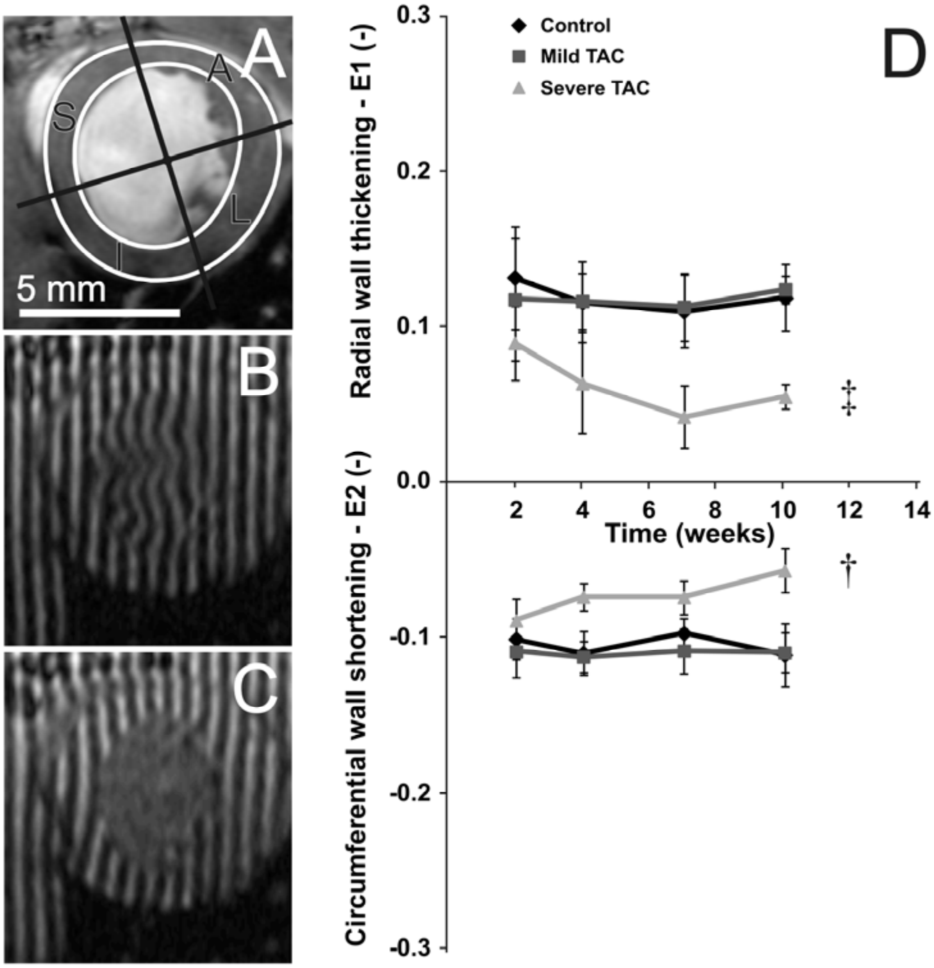

Figure 2.7 (A) Typical end-diastolic short-axis MR image of a severe TAC mouse acquired 10 weeks after surgery overlaid with endocardial and epicardial contours and the four segments used for regional quantification of myocardial principal strains. S = septum, A = anterior wall, L = lateral wall, I = inferior wall. The corresponding mid ventricular short-axis tagged MR images in end-diastole (B) and end-systole (C). Left ventricular radial wall thickening E1 and circumferential wall shortening E2 at week 2 until 10, at which all mice were in experiment (D). E1 and E2 decreased in the severe TAC mice (n = 9, $P < 0.05$), but not in the mild TAC (n = 3) mice as compared to controls (n = 7). Mean and SD per time point are denoted by the corresponding symbol and error bars. Statistical differences as compared to the control group are indicated by † ($P < 0.01$) and ‡ ($P < 0.001$).

Discussion

In this study we investigated the evolution of RV and LV function in well-controlled mouse models of compensated hypertrophy and decompensated HF as induced by two different degrees of transverse aortic constriction (TAC), using cinematographic and tagging MRI [13].

There are a number of important findings to this study. First, mice with a mild TAC revealed myocardial hypertrophy and only a slightly depressed LVEF consistent with a state of compensated hypertrophy. Second, mice subjected to a severe TAC showed progressive LV hypertrophy, increased LV volumes and a drastic decline in LV function in accordance with a condition of HF. Third, myocardial principal strains were significantly reduced in severe TAC mice as compared to controls and progressively decreased over time. Fourth, changes in RV volumes and EF could be quantified in TAC mice using cardiac MRI. Fifth, the progressive deterioration of LV function in severe TAC mice was followed in time by worsening of RV function and severe pulmonary remodeling, two important hallmarks of congestive left ventricular pump failure [10,18,24].

LV mass, end-diastolic and end-systolic volumes were slightly elevated at 2 weeks after mild TAC, after which these variables remained essentially constant. RV volumes and EF in mild TAC mice, however, were unchanged as compared to control mice. The severe TAC mice showed a progressive increase in both end-diastolic and end-systolic volumes accompanied by a decline in LVEF. In these mice also a marked increase was found in RV end-systolic volume as compared to the control mice resulting in a deteriorating RVEF. The absence of RV dilation, RV end-diastolic volumes remained unchanged, may point to impaired contractile properties rather than dilation as a cause for the impaired RV function. These mice likely also developed profound pulmonary remodeling, as indicated by a significantly increased LuW/TL ratio as compared to controls. However, no differences in lung water content were observed, indicated by a constant lung wet weight-to-dry weight ratio. This is in line with recent evidence suggesting that increased lung mass secondary to LV failure in TAC mice is caused by pulmonary remodeling with an increased percentage of fully muscularized vessels, vascular and lung fibrosis, myofibroblast proliferation, and leukyocyte infiltration, but not by an increased lung water content [18]. Finally, the severe TAC mice showed a progressive increase in LV mass. Moreover, in a subset of these mice extreme apical wall thinning and akinesia was observed. The underlying mechanisms responsible for the formation of these apical aneurysms in response to pressure overload-induced hypertrophy, however, remain to be determined. Taken together, the mild TAC mice revealed a condition of compensated hypertrophy, whereas the severe TAC mice developed overt congestive biventricular failure.

Awareness is growing that RV function has an important impact on symptom occurrence, disease progression as well as exercise tolerance in various cardiac pathologies [10]. Pulmonary hypertension is one of the most prominent causes of RV failure and is often due to LV pathologies [10]. Recent evidence suggests that the RV and LV are categorically different [10,25]. For example, both ventricles originate from different progenitor cells and sites during cardiac morphogenesis, have a different morphology and show important differences with respect to the expression of regulatory proteins in response to stressors as ischemia and hypertension. Thus, RV failure cannot be understood by straightforward extrapolation of the knowledge about LV failure. Although surgically induced TAC in mice has been extensively used as a model to study pressure overload induced LV hypertrophy and failure, data on RV function in this model is scarce [12,13,26-29]. Since RV failure in severe TAC results from LV pathology, it could also be used as a highly relevant model to study RV adaptations to LV hypertrophy and failure. Quantification of murine RV function using echocardiography is not straightforward due to the complex shape and motion of the RV. The alternative use of conductance catheters is invasive and cannot yield information on cardiac mass [30,31]. In contrast, cardiac MRI offers the possibility to quantify both RV function and potentially also RV mass and could therefore well be used to study the interplay between both ventricles, as was done in this study [16].

Cardiac strains were quantified in terms of the 2D principal strains from tagged MR images using a method based on optical flow theory. While myocardial principal strain E1 is mainly oriented in the radial direction, E2 coincides with the circumferential direction [22]. No differences were observed in both principal strains between the control and mild TAC group. Moreover, no time effect was observed in both groups, in line with the essentially constant EF. Furthermore, no differences in WT were observed between healthy and mild TAC mice, in agreement with the absence of differences in radial wall thickening E1. On the other hand, the severe TAC mice showed a significant decline of the radial wall thickening and circumferential wall shortening from week 2 to 10, which was paralleled by a large drop in EF. Finally, the lowering of radial wall thickening was reflected in a reduction in WT.

The effects of both passive and active cardiac tissue mechanics on the transition from hypertrophy to heart failure gain increased interest [32,33]. Therefore, we investigated whether early strain changes precede late changes in global cardiac morphology or function during the development of HF. However, such an effect was not observed.

Instead, changes in WT and myocardial strains developed synchronously with alterations in global cardiac parameters. These findings suggest that the added value of local strain analysis is more evident when heterogeneous myocardial contraction is anticipated, for example in the infarcted heart, as compared to pathologies with an essentially homogeneous contraction pattern, as studied here.

The septum is believed to contribute to both LV and RV function in the normal and diseased heart, although the precise mechanisms are not fully understood [30]. We therefore determined the relationship between septal principal strains and RVEF for all groups. However, in our data we did not find any clear relationship between these parameters ($r < 0.30$, in all cases). Although approximately 24% of RV ejection depends on LV contraction, the majority of RV ejection results from longitudinal shortening of the RV during systole [10]. Most likely 3D strain analysis in the septal wall will be required to determine the contribution of septal motion on RV ejection during deterioration of LV function.

The disease progression reported in this study compares well with previous data, despite the fact that the phenotype resulting from TAC surgery may vary depending on mouse strain and the surgical technique used [29]. Rothermel *et al.* induced a mild (Ø 0.42 mm) and a severe TAC (Ø 0.38 mm) in 6-8 weeks old, male C57BL/6 mice [34]. Animals with a mild TAC developed a significant increase of LV mass as compared to healthy mice, but were clinically indistinguishable. By contrast, mice subjected to a severe TAC developed signs of end-stage HF within 3 weeks. In our study 11 weeks old mice were used, necessitating the use of larger needle diameters, both for the induction of the mild and the severe TAC.

Cardiac MRI is an important clinical tool for HF diagnosis [35]. Currently, imaging biomarkers for the characterization of HF are often restricted to cardiac pathological anatomy (LV mass) and function (LVEF). However, the management of patients with hypertrophy and HF may significantly benefit from additional imaging read-outs reporting on the presence of fibrosis, a decreasing capillary density, or changes in cardiac metabolism. A range of MR techniques have recently become available for this purpose, including cardiac T_1 mapping [36,37], quantitative perfusion MRI [38,39] and MR spectroscopy for the heart [40,41]. The well-controlled disease model presented in this study might prove an important preclinical step to assess the added value of these novel imaging read-outs for HF diagnosis. Since the RV is gaining increasing attention as a potential therapeutic target, it might also be of great interest to study the effects of new therapeutic strategies on both LV and RV function in TAC mice using MRI [25]. One example is the inhibition of small molecule histone deacetylase, which has been shown to block myocardial remodeling in various HF models [42]. Such studies could also take into account potential improvements in exercise capacity related to RV function.

There are some limitations to this study. A valuable comparison of LV and RV volumes and function with, for example, conductance catheters measurements was not made. However, it was anticipated that this would require a large cohort of mice, since catheter measurements in mice are terminal. Instead, the number of mice required was minimized by choosing a longitudinal study design with readouts from noninvasive imaging. The experimental variation in for example LV mass, LV EDV and ESV increased during the course of the experiment, in particular in the severe TAC group, but was comparatively small at the start of the experiment. This suggests that within group differences in systolic pressure gradient immediately after TAC were small and that the observed variation resulted from inter animal differences, but we cannot fully exclude some variation due to small differences in pressure gradient. Although the number of mice in the sham and mild TAC groups was limited, the longitudinal study design generally is more efficient and results in increased statistical power as changes over time are assessed within the same animals.

Conclusion

In this study longitudinal MRI measurements were performed in mice subjected to a mild or severe TAC. The mice with a mild TAC developed compensated hypertrophy, whereas the mice with a severe TAC developed congestive HF. A decline in RV function was observed following the progressive deterioration of LV function, relevant for many cases where RV failure develops secondary to LV pathologies. The well-controlled aortic banding model of HF described here therefore opens opportunities to assess the added value of various new MR imaging techniques for the diagnosis of HF, to study the impact of new therapeutic strategies on disease progression and symptom occurrence in the RV and LV, and to assess the effects of pharmacological or mechanical LV unloading on the RV. Such studies might eventually lead to improvements in care for patients suffering from pressure overload-induced HF.

Acknowledgement

This research was performed within the framework of the Center for Translational Molecular Medicine, project TRIUMPH (grant 01C-103), and supported by the Dutch Heart Foundation. We gratefully acknowledge D. Veraart and J. Debets for biotechnical assistance, and W.M. Blankesteijn (Maastricht University) for discussions.

References

1. Denolin, H., et al. Eur Heart J, 1983, 4(7), 445-8.
2. Juenger, J., et al. Heart, 2002, 87(3), 235-41.
3. de Couto, G., et al. Nat Rev Cardiol, 2010, 7(6), 334-44.
4. Lloyd-Jones, D., et al. Circulation, 2010, 121(7), e46-e215.
5. McMurray, J.J., Stewart S. Heart, 2000, 83(5), 596-602.
6. Cokkinos, D.V., Pantos C. Heart Fail Rev, 2011, 16, 1-4.
7. Frey, N., Olson E.N. Annu Rev Physiol, 2003, 65, 45-79.
8. Neubauer, S. N Engl J Med, 2007, 356(11), 1140-51.
9. Mann, D.L., Bristow M.R. Circulation, 2005, 111(21), 2837-49.
10. Voelkel, N.F., et al. Circulation, 2006, 114(17), 1883-91.
11. Tourneau, T.L., et al. Minerva Cardioangiol, 2011, 59(4), 349-74.
12. Rockman, H.A., et al. Proc Natl Acad Sci U S A, 1991, 88(18), 8277-81.
13. van Deel, E.D., et al. J Mol Cell Cardiol, 2011, 50(6), 1017-25.
14. Fischer, S.E., et al. Magn Reson Med, 1993, 30(2), 191-200.
15. Heijman, E., et al. J Magn Reson Imaging, 2008, 27(1), 86-93.
16. Wiesmann, F., et al. Am J Physiol Heart Circ Physiol, 2002, 283(3), H1065-H71.
17. Manning, W.J., et al. Am J Physiol, 1994, 266(4 Pt 2), H1672-H5.
18. Chen, Y., et al. Hypertension, 2012, 59(6), 1170-8.
19. Florack, L., et al. in Proceedings of the 8th IEEE Computer Society Workshop on Mathematical Methods in Biomedical Image Analysis, Held in Conjuction with the IEEE International Conference on Computer Vision, Rio de Janeiro, Brazil, 2007, 1-8.
20. Gabor, D. J Inst Elect Eng, 1946, 93, 429-57.
21. Florack, L., van Assen H. Int J Biomed Imaging, 2010, 2010, 341242.
22. Garot, J., et al. Circulation, 2000, 101(9), 981-8.
23. Cerqueira, M.D., et al. Circulation, 2002, 105(4), 539-42.
24. Kee, K., Naughton M.T. Circ J, 2010, 74(12), 2507-16.
25. Banerjee, D., et al. Curr Heart Fail Rep, 2010, 7(4), 202-11.
26. Brede, M., et al. Circulation, 2002, 106(19), 2491-6.
27. Qu, J., et al. Circ Res, 2009, 104(3), 365-71.
28. Lygate, C. Drug Discov Today Dis Models, 2006, 3(3), 283-90.
29. Berry, J.M., et al. Drug Discov Today Dis Models, 2007, 4(4), 197-206.
30. Lindqvist, P., et al. Eur J Echocardiogr, 2008, 9(2), 225-34.
31. Jacoby, C., et al. Basic Res Cardiol, 2006, 101(1), 87-95.
32. Hankiewicz, J.H., et al. Am J Physiol Heart Circ Physiol, 2008, 294(1), H330-H6.
33. Costandi, P.N., et al. Am J Physiol Heart Circ Physiol, 2006, 291(6), H2971-H9.
34. Rothermel, B.A., et al. Physiol Genomics, 2005, 23(1), 18-27.
35. Karamitsos, T.D., et al. J Am Coll Cardiol, 2009, 54(15), 1407-24.
36. Coolen, B.F., et al. NMR Biomed, 2011, 24(2), 154-62.
37. Iles, L., et al. J Am Coll Cardiol, 2008, 52(19), 1574-80.
38. van Nierop, B.J., et al. Magn Reson Med, 2012, doi: 10.1002/mrm.24424.
39. Vandsburger, M.H., et al. Magn Reson Med, 2010, 63(3), 648-57.
40. Bottomley, P.A. NMR Spectroscopy of the Human Heart. Encyclopedia of Magnetic Resonance: John Wiley & Sons, Ltd, 2007.
41. Gupta, A., et al. Am J Physiol Heart Circ Physiol, 2009, 297(1), H59-H64.
42. Lemon, D.D., et al. J Mol Cell Cardiol, 2011, 51(1), 41-50.

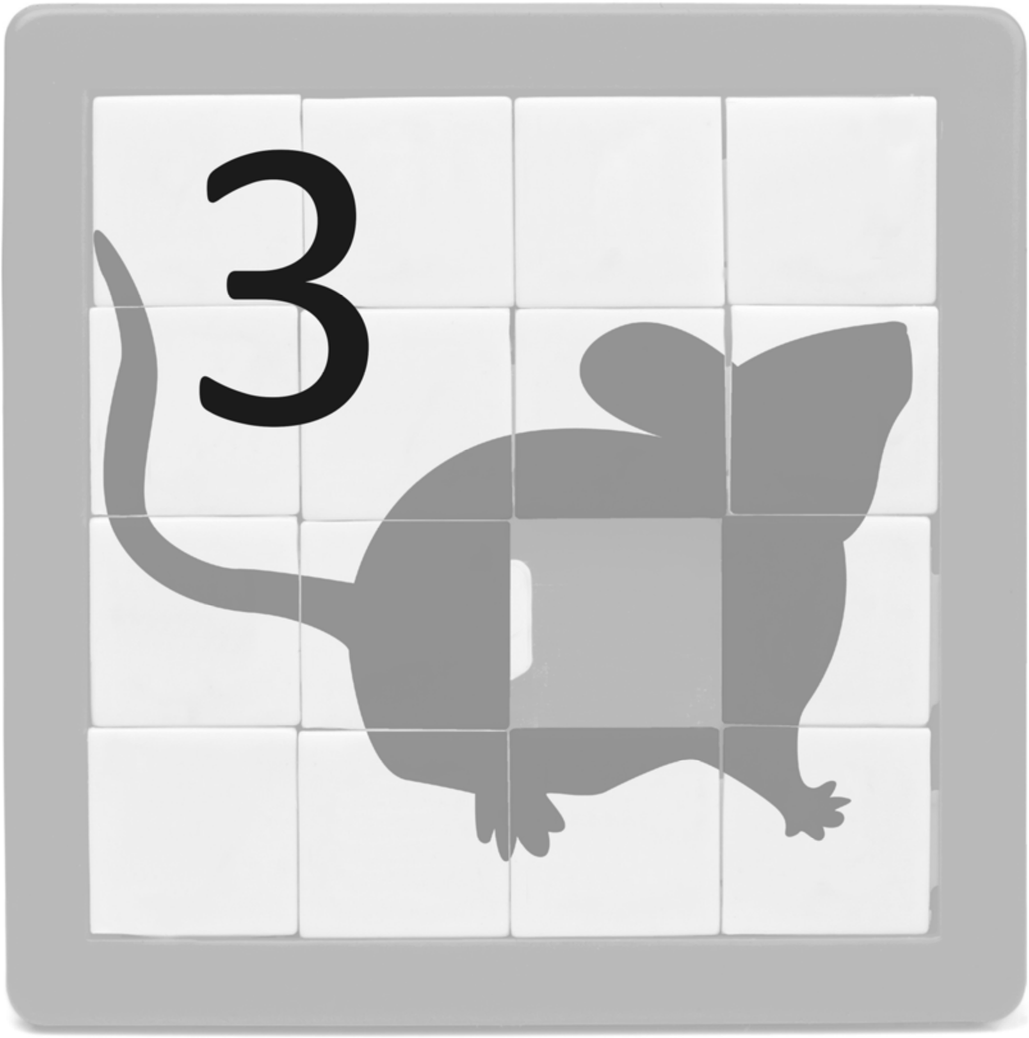

3

Quantitative first-pass perfusion MRI of the mouse myocardium

Bastiaan van Nierop, Bram Coolen, Wouter Dijk, Arjan
Hendriks, Larry de Graaf, Klaas Nicolay,
and Gustav Strijkers

Based on: Magnetic Resonance in Medicine, **2012**, DOI: 10.1002/mrm.24424

Abstract

Objective: In this study we present a first-pass perfusion imaging protocol to determine quantitative regional perfusion values (in mL min^{-1} g^{-1}) of the mouse myocardium.

Methods: Perfusion was quantified using a Fermi constrained deconvolution of the myocardial tissue response with the arterial input function. A dual-bolus approach was implemented.

Results: Experimental evidence is presented for the linearity of signal intensity in the LV lumen during the prebolus (r = 0.99, $P < 0.001$) and in the myocardium during the full-bolus injection (r = 0.99, $P < 0.01$) as function of $Gd(DTPA)^{2-}$ injection concentration employed. The prebolus was used to reconstruct a non-saturated arterial input function. Regional perfusion values proved repeatable in a cohort of nine healthy C57BL/6 mice. The perfusion values over two measurements with a one-week interval were 7.3 ± 0.9 and 7.2 ± 0.6 mL min^{-1} g^{-1}, respectively. No significant effects of time and myocardial region were observed. The between-session coefficient of variation was only 6%, while the inter-animal coefficient of variation was 11% and 8% for the separate experiments.

Conclusion: We expect that the first-pass perfusion method presented here will be useful in preclinical studies of pathologies that are accompanied by myocardial perfusion deficits and valuable to assess the impact of pro-angiogenic therapy after myocardial infarction.

Introduction

Dynamic MR imaging of the first-passage of a Gd(DTPA)$^{2-}$ bolus can be used to determine myocardial perfusion [1-3]. Clinically, perfusion MRI and late-gadolinium-enhancement (LGE) MRI are very valuable tools and increasingly used as diagnostic readouts in patients with suspected coronary artery disease [4]. Also, in preclinical studies of mouse models of myocardial disease a time-efficient quantitative first-pass perfusion method that can be integrated into a multi-parametric cardiac MRI protocol is highly desired. Therefore, the aim of this study was to design a quantitative first-pass perfusion method for the mouse myocardium and to assess the repeatability of regional perfusion values in a cohort of healthy mice.

The method builds on the semi-quantitative first-pass perfusion technique previously introduced by Coolen *et al.* [5]. In that study, the key innovation was a rapid image acquisition enabled by parallel imaging and GRAPPA reconstruction during the Gd(DTPA)$^{2-}$ infusion. The resulting temporal resolution of one image every three mouse heart beats was sufficiently fast to accurately capture the first-passage of the bolus of contrast agent. The up-slope of the signal from the left-ventricular (LV) myocardial time-course was normalized to the up-slope of the LV lumen blood signal time-course and served as a semi-quantitative measure for myocardial perfusion.

In this study, quantitative myocardial perfusion values (in mL min^{-1} g^{-1}) were obtained from a Fermi-constrained deconvolution of the measured myocardial tissue response with the arterial input function (AIF) measured in the LV lumen [6]. This method relies on the assumption that the signal intensities in both the LV lumen and myocardium scale linearly with contrast agent concentration. However, to obtain sufficient signal change of myocardial tissue during the first-passage, a bolus injection with a high contrast agent concentration was required, which inevitably led to saturation of the AIF and possibly even of the myocardial signal [7]. To overcome this problem a low-dose prebolus measurement was added from which the AIF was reconstructed [8]. Contrast agent concentrations in the prebolus and full-bolus were varied to determine the relationship with the LV lumen and myocardial signal changes, respectively. Subsequently, repeatability of the regional quantitative perfusion values was investigated in nine healthy mice, which were measured two times with a one-week interval.

Methods

Animal handling

A total of 31 C57BL/6 mice (♂, age 11 weeks, 24-27 grams) were included in this study. Animals were housed under standard laboratory conditions with a 12 hour light/dark cycle and were maintained on a standard diet with access to water *ad libitum*. All animal experiments were performed according to a protocol approved by the Animal Care and Use Committee of Maastricht University.

MR examinations

All MR images were acquired with a 9.4 T small animal MRI scanner (Bruker BioSpec, Ettlingen, Germany) equipped with a 740 mT/m gradient coil. A 72-mm-diameter quadrature transmit coil was used in combination with a 4 element phased-array receive coil (Bruker). Mice were anesthetized with isoflurane (4.0 vol% for induction, 1.5-2.0 vol% for maintenance) in medical air (0.4 L min^{-1}). The front paws were placed on ECG electrodes and a balloon pressure sensor was placed on the abdomen. Body temperature was maintained at 36-37^{o}C with a heating pad and monitored with a rectal temperature sensor. An infusion pump (Chemyx Fusion 100, flow rate: 2 mL min^{-1}) was used to ensure repeatable tail vein infusion of $Gd(DTPA)^{2-}$ (Bayer HealthCare Pharmaceuticals, Mijdrecht, The Netherlands) in 0.9% NaCl (Figure 3.1). The flow rate was optimized previously and it was found that higher flow rates were poorly tolerated by the mice [5]. In a pilot experiment the accuracy of the infused volumes was confirmed with a microbalance. Moreover, the actual flow rate was confirmed with a high-speed camera during the infusion of a prebolus and a full-bolus containing a colored dye in mice (n = 2). Mid-ventricular, short-axis first-pass perfusion images were acquired using an ECG-triggered, segmented saturation-recovery FISP sequence, with the following acquisition parameters: pulse repletion time (TR) = 1.18 ms, echo time (TE) = 0.51 ms, field of view = 3x3 cm^2, matrix = 64x39 (3 segments, acquired over three consecutive heart beats), GRAPPA parallel acceleration factor = 1.64, reconstruction matrix = 128x128, slice thickness = 1.5 mm, excitation pulse (0.3 ms Gauss pulse, α = 15°), saturation pulse (2 ms Gauss pulse, α = 90°) [5].

Linearity of signal intensity with $Gd(DTPA)^{2-}$ concentration

Mice (n = 10) underwent up to three MRI sessions with one-week intervals. To assess linearity of the arterial input function signal intensity with $Gd(DTPA)^{2-}$ concentration, at each session one 25 µL prebolus of $Gd(DTPA)^{2-}$ (concentration in the injection fluid: 15, 30, 40 or 60 mM) or saline was infused. Only a single bolus was injected per session

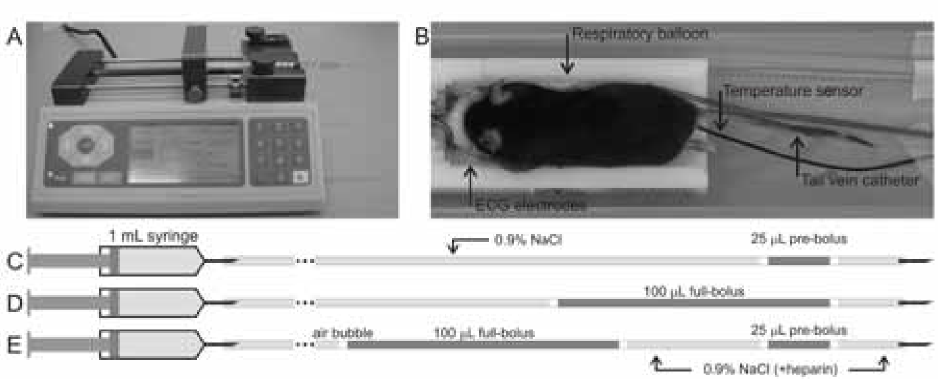

Figure 3.1. (A) Photograph of the infusion pump and (B) a mouse in the animal cradle. The ECG electrodes, the respiratory balloon, the rectal temperature sensor and the polyethylene tail vein catheter (0.4 mm inner diameter) are indicated with arrows. For each experiment one infusion line was preloaded with a 25 µL prebolus, a 100 µL full-bolus or a prebolus and full-bolus to test the linearity of signal intensity with $Gd(DTPA)^{2-}$ concentration for (C) the prebolus and (D) the full-bolus and (E) to test the perfusion quantification repeatability. A small air-bubble before and after each bolus prevented contrast agent dispersion in the surrounding saline solution.

resulting in a constant anesthesia period for all mice. This protocol also prevented experimental variation as a consequence of $Gd(DTPA)^{2-}$ accumulation.

In a separate experiment mice (n = 10) underwent up to four MRI sessions with one-week intervals. To assess linearity of the myocardial signal intensity with $Gd(DTPA)^{2-}$ concentration, at each session one 100 µL full-bolus of $Gd(DTPA)^{2-}$ (concentration in the injection fluid: 15, 30, 40 or 60 mM) was infused.

Repeatability of regional perfusion quantification

Mice (n = 9) underwent two MRI sessions with a one-week interval. At each session first-pass perfusion images were acquired with a prebolus (25 µL, 40 mM) and a full-bolus (100 µL, 40 mM). In between both boluses a 20 min waiting time ensured a sufficient degree of $Gd(DTPA)^{2-}$ clearance. LV function and mass were quantified during these 20 min. To this end 2 long-axis and a stack of 5 short-axis cinematographic (cine) MR images were obtained with 15-18 frames covering the complete cardiac cycle using an ECG-triggered and respiratory-gated FLASH sequence, as described previously [9,10].

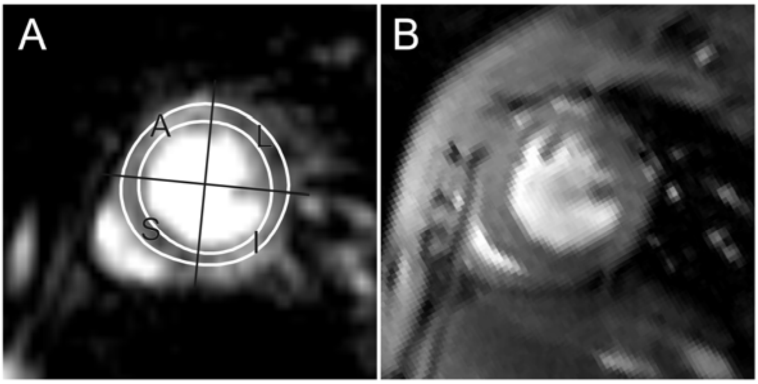

Figure 3.2. (A) Mid ventricular short-axis image during diastole overlaid with endocardial and epicardial contours and the four segments used for regional quantification of myocardial perfusion. S = septum, A = anterior wall, L = lateral wall, I = inferior wall. (B) Corresponding cinematographic diastolic short-axis image.

Data analysis

Signal intensity time curves from the LV blood pool and the LV myocardium were obtained using home-built software in Matlab (The Mathworks, Inc.). The regions-of-interest were slightly adjusted per frame to correct for small translational respiratory movement of the heart. Pre-injection baseline signal intensity was subtracted from the signal intensity time curve and subsequently the curves were normalized to the pre-injection baseline signal to correct for signal reception inhomogeneities introduced by the RF receive surface coil.

A γ-variate function was fitted to the signal intensity time curve to analyze the linearity between the LV lumen and myocardial signal intensities and $Gd(DTPA)^{2-}$ prebolus and full-bolus injection concentrations, respectively. From the fittings the mean transit time (MTT) and the area under the curve (AUC) were extracted. For perfusion quantification in the LV tissue, a non-saturated AIF was reconstructed from four time-shifted γ-variate prebolus fits, as described previously [8]. Next, myocardial tissue perfusion (mL min^{-1} g^{-1}) was quantified using a Fermi constrained deconvolution of the myocardial tissue response from the full-bolus with the AIF [6] using a Levenberg-Marquardt least squares fitting algorithm. For regional perfusion analysis the LV myocardium was divided in four segments (Figure 3.2), as proposed previously [11].

Statistics

Data are expressed as mean ± standard deviation (SD). Linearity of the AUC with concentration Gd(DTPA)$^{2-}$ in the injection solutions was assessed by performing linear regression analysis without offset. The AUC for the varying concentrations Gd(DTPA)$^{2-}$ in the full-bolus and the mean transit times for varying Gd(DTPA)$^{2-}$ concentrations in the injection solutions of both the prebolus and full-bolus injections, were compared with a one-way ANOVA. Changes in respiratory rate and cardiac parameters in the final experiment were tested for statistical significance with a two-sided, paired Student *t*-test. Finally, repeatability of the perfusion quantification was assessed by performing an ANOVA for repeated measures with time and region as factors, followed by a Bonferroni post-hoc test, and by means of Bland-Altman analysis [12]. Calculations were performed using SPSS 19.0 (SPSS Inc., Chicago). For all tests the level of significance was set at $\alpha = 0.05$.

Results

A series of representative myocardial first-pass perfusion images of a prebolus and full-bolus experiment are shown in Figure 3.3, at various time points before and after injection of the contrast agent. Blood and myocardial signal were appropriately nulled before contrast agent injection. For both the prebolus and full-bolus measurements one can observe the arrival of the contrast agent in the right ventricle (5.4 s), in the left ventricle (5.8 s), and in the myocardium (>6.2 s). For the prebolus only minor signal enhancement was observed in the myocardium and signal intensity in the whole image returned quickly to baseline levels, indicating fast clearance of the low volume prebolus.

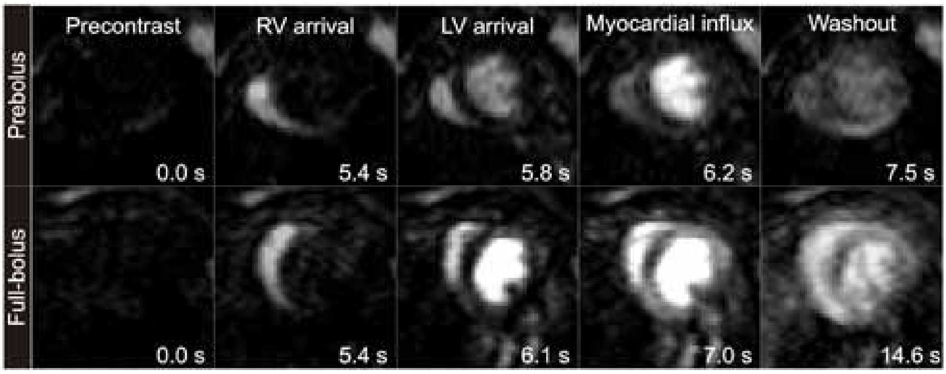

Figure 3.3. Time series of cardiac images during the first-passage of a prebolus (top row, 25 µL, 40 mM Gd(DTPA)$^{2-}$) and a full-bolus (bottom row, 100 µL, 40 mM Gd(DTPA)$^{2-}$). From left to right: precontrast, RV arrival, LV arrival, myocardial influx, and washout.

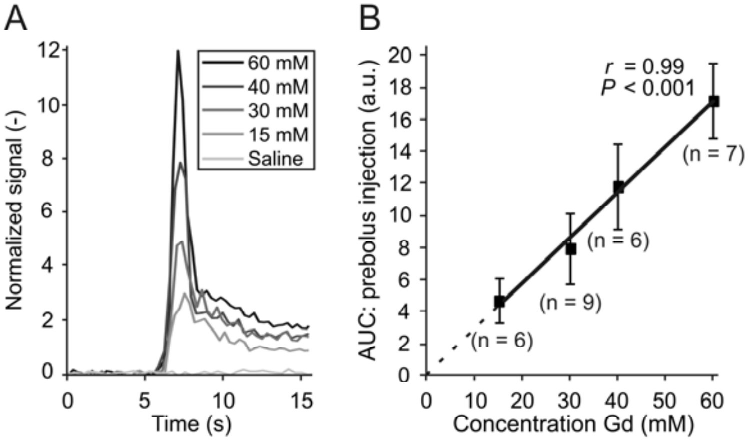

Figure 3.4. (A) Examples of LV lumen signal intensity (SI) time curves of the prebolus with varying $Gd(DTPA)^{2-}$ concentrations. (B) Group-averaged area under the curve (AUC) of the fitted γ-variate function as function of infusion solution $Gd(DTPA)^{2-}$ concentration. Error bars indicate SD for the indicated number of independent measurements. The solid line is a linear fitting.

Linearity of signal intensity with $Gd(DTPA)^{2-}$ concentration

The LV lumen signal intensity changes induced by the 25 μL prebolus were proportional to the infusion solution $Gd(DTPA)^{2-}$ concentration (Figure 3.4A). Control injections with saline (n = 2) did not result in a signal change. A very strong linear correlation (r = 0.99, $P < 0.001$) was found between the AUC and the prebolus infusion solution $Gd(DTPA)^{2-}$ concentration (Figure 3.4B). The MTT for the prebolus injections was not affected by $Gd(DTPA)^{2-}$ concentration ($P > 0.05$), with an average value of 1.5 ± 0.5 s (n = 28).

The maxima of the signal intensity time curves obtained in the LV myocardium resulting from the 100 μL full-bolus increased proportional with the infusion solution $Gd(DTPA)^{2-}$ concentration up to 40 mM $Gd(DTPA)^{2-}$ (Figure 3.5A). Infusion of a 60 mM full-bolus resulted in a similar signal intensity time curve as injection with 40 mM. One-way ANOVA analysis followed by a Bonferroni post-hoc test revealed significant differences between the AUC of the 15 mM, 30 mM and the 40 mM full-bolus (Figure 3.5B, $P < 0.01$ in all cases), but not between the 40 mM and 60 mM full-bolus (P = 0.47). A linear correlation (r = 0.99, $P < 0.01$) was observed between the AUC and the full-bolus infusion solution $Gd(DTPA)^{2-}$ concentration up to 40 mM $Gd(DTPA)^{2-}$. The MTTs for the full-boluses with varying $Gd(DTPA)^{2-}$ concentrations were not significantly different, with an average value of 5.5 ± 0.8 s (n = 34).

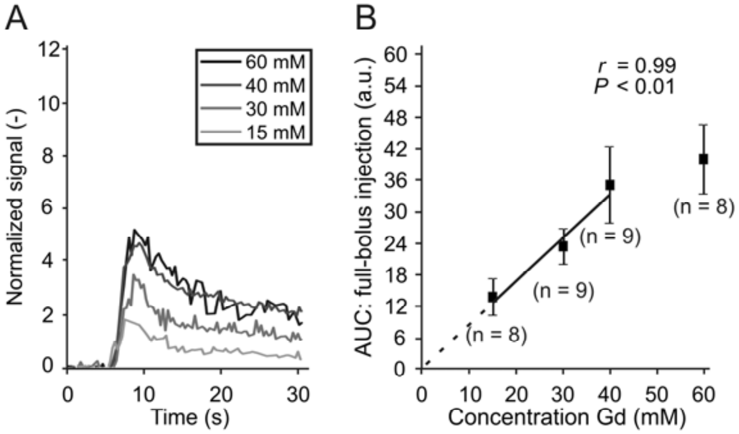

Figure 3.5. (A) Examples of LV myocardial signal intensity (SI) time curves of the full-bolus with varying infusion solution Gd(DTPA)$^{2-}$ concentrations. (B) Group-averaged area under the curve (AUC) of the fitted γ-variate functions as function of the Gd(DTPA)$^{2-}$ concentration. Error bars indicate SD for the indicated number of independent measurements. The solid line is a linear fitting to the 15, 30 and 40 mM data points.

Based on the above assessment of linearity of signal intensities with Gd(DTPA)$^{2-}$ concentration in the infusion solutions, a concentration of 40 mM Gd(DTPA)$^{2-}$ in prebolus and full-bolus solutions was chosen for the perfusion quantification experiments described below, which ensured the highest signal-to-noise ratio in the lumen and myocardium, while guaranteeing linearity with concentration.

Regional perfusion quantification

Global functional LV cardiac parameters were assessed at week 1 and 2 by cine MRI to rule out that differences in cardiac function could have biased the assessment of perfusion quantification repeatability (Table 3.1). None of the investigated parameters (heart rate, respiratory rate, EDV, ESV, SV, CO, and LV mass) were significantly different between the two measurements (n = 9).

Repeated signal intensity versus time curves in the LV lumen for the prebolus and full-bolus of a representative mouse that was included in the repeatability measurements are shown in Figure 3.6A and Figure 3.6B. Regional signal intensity versus time curves in the myocardium of the same mouse after injection of the full-bolus for the repeated measurements are depicted in Figure 3.6C. These graphs qualitatively illustrate the good repeatability of the measurements. From the prebolus measurement a non-saturated AIF was reconstructed as exemplified in Figure 3.7.

Next, myocardial tissue perfusion (in mL min^{-1} g^{-1}) was quantified regionally for each mouse at the two measurement time points using a Fermi constrained deconvolution of the myocardial tissue response from the full-bolus with the reconstructed AIF (Figure 3.8). The resulting quantitative perfusion values in the different wall sections at both time points are plotted in Figure 3.9A. Average perfusion values at week 1 and 2 were 7.3 ± 0.9 and 7.2 ± 0.6 mL min^{-1} g^{-1}, respectively. An ANOVA for repeated measures analysis, followed by a Bonferroni post-hoc test, revealed no significant effect of both time and region on the perfusion values.

Table 3.1. Global LV cardiac parameters determined from cine MRI of the cohort of healthy mice (n = 9) at week 1 and 2. HR = heart rate, Resp = respiratory rate, EDV = end-diastolic volume, ESV = end-systolic volume, SV = stroke volume, CO = cardiac output, and LV mass = left ventricular myocardial mass. For all parameters there was no statistical difference between measurements at week 1 and 2.

	Week 1	**Week 2**
HR (min^{-1})	513 ± 40	513 ± 51
Resp (min^{-1})	54 ± 10	52 ± 6
EDV (µL)	60.2 ± 5.7	63.8 ± 7.6
ESV (µL)	19.8 ± 2.4	19.0 ± 2.7
SV (µL)	40.4 ± 4.0	44.8 ± 5.5
CO (mL min^{-1})	20.7 ± 2.8	22.8 ± 3.0
LV mass (mg)	77.1 ± 4.5	77.7 ± 3.8

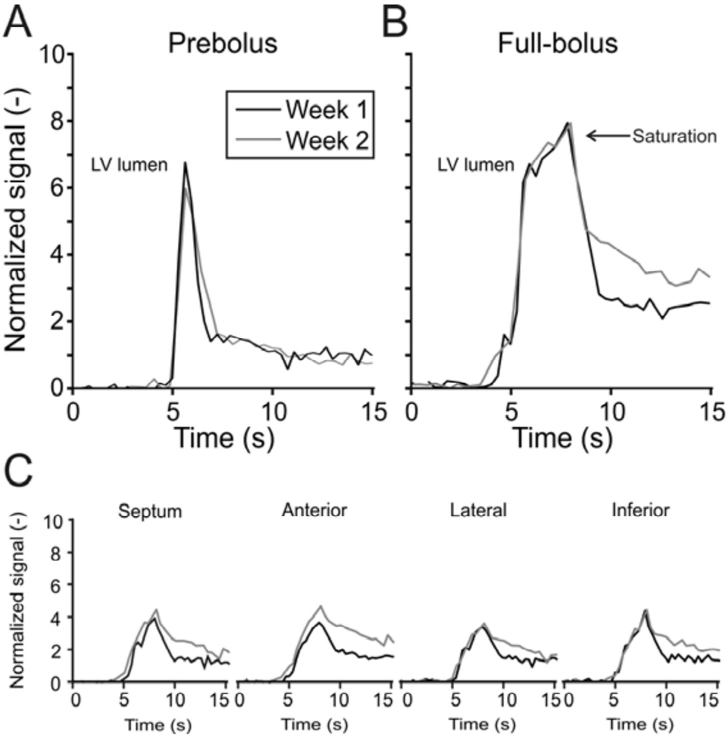

Figure 3.6. (A) Example of two SI time curves in the LV lumen obtained from a prebolus and (B) from a full-bolus injection at week 1 and 2 in the same mouse. Signal intensity is saturated around the peak enhancement in the full-bolus (arrow). (C) Myocardial enhancement in the septum, and the anterior, lateral and inferior wall by full-bolus injections at week 1 and 2 in the same mouse. Qualitatively there is excellent agreement between both experiments.

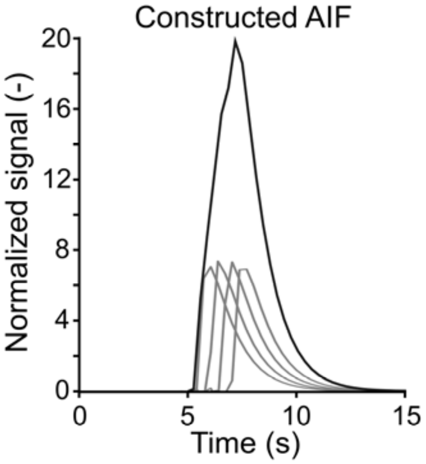

Figure 3.7. Reconstruction of a non-saturated AIF from four γ-variate fits of the prebolus intensity-time curves. The four prebolus curves were shifted in time to match the MTT of the full-bolus injection.

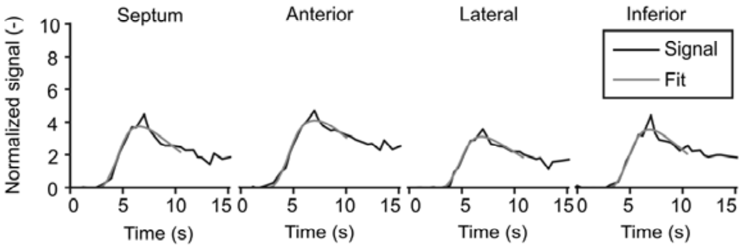

Figure 3.8. Measured myocardial tissue responses in the four wall segments and the corresponding modeled signal responses, obtained from the Fermi constrained deconvolution of the myocardial tissue responses with the arterial input function.

Repeatability of perfusion quantification

To assess repeatability of the perfusion quantification Bland-Altman analysis was performed (Figure 3.9B). The mean difference between week 1 and 2 was close to zero for all LV segments, indicating the absence of systematic errors. Furthermore, the limits of agreement between both measurements, expressed as percentage of the myocardial perfusion, were found to be 25%, 21%, 32% and 40% in the septum and in the anterior, lateral and inferior wall sections, respectively. Inter-animal coefficient of variation (CV) values were found similar for the first (CV = 11%) and second (CV = 8%) measurement. Between-session CV of week 1 and 2 was 6%.

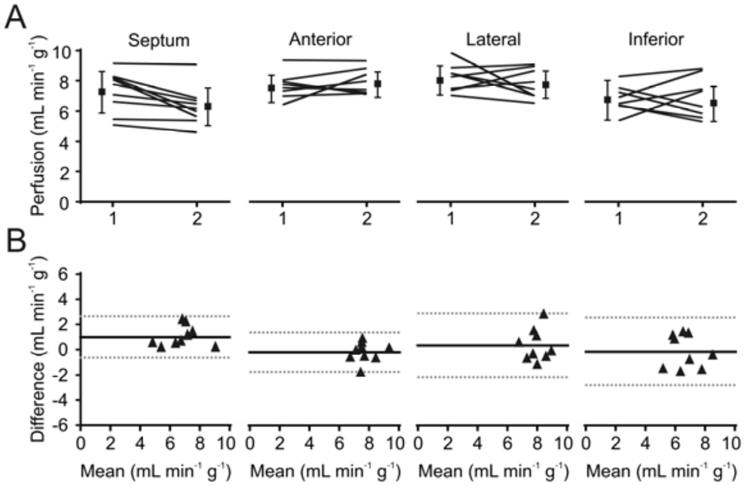

Figure 3.9. (A) Perfusion values in the septum and the anterior, lateral and inferior wall of the left ventricle of the individual mice at week 1 and 2. Mean and SD per time point are denoted by the error bars. (B) Bland-Altman plots of the differences between week 1 and 2. Indicated are the mean difference (solid line) and the limits of agreement (dashed lines) defined as ± 2 SD of the differences.

Discussion

To obtain a repeatable perfusion quantification method for the mouse myocardium, several steps were performed within this study. First, we provided direct experimental evidence for linearity of mouse LV lumen and myocardium signal intensity time-course area with $Gd(DTPA)^{2-}$ injection concentration. Second, we showed that from a prebolus measurement a non-saturated AIF could be reconstructed. Third, regional perfusion values in mouse myocardium were quantified using a Fermi-constrained deconvolution of the myocardial tissue response with the non-saturated AIF. Finally, the regional quantitative perfusion values proved repeatable over two measurements with one-week intervals.

The Fermi-constrained deconvolution method for perfusion estimation requires a non-saturated AIF and assumes linearity of signal changes in the myocardium with $Gd(DTPA)^{2-}$ concentration [6]. We provided direct experimental evidence that for the 100 µL full-bolus, the LV myocardial signal varied linearly with injection concentration up to 40 mM $Gd(DTPA)^{2-}$. However, for the full-bolus the AIF in the LV lumen was saturated (Figure 3.6B). Therefore, a non-saturated AIF was reconstructed from a 25 µL prebolus injection, an approach that was introduced previously for humans [8]. An alternative approach would be to use equal infusion volumes for both boluses with a lower prebolus $Gd(DTPA)^{2-}$ infusion concentration without the need to time shift four prebolus intensity-time curves for reconstruction of the AIF [13]. However, we preferred the current approach as it minimized the total infusion volume.

The LV lumen MTT values for both the preboluses and full-boluses, were independent of the $Gd(DTPA)^{2-}$ infusion concentration, proving that $Gd(DTPA)^{2-}$ injection concentration had no influence on the shape of the AIF and the myocardial tissue response curves. This is in agreement with findings by Epstein *et al.* who showed that, provided that the dispersion time of the contrast agent bolus in the vasculature and lungs is large as compared to the injection time, the LV contrast agent concentration curve amplitude scales with $Gd(DTPA)^{2-}$ concentration and its width remains essentially constant [14]. The injection volume ratio of full-bolus and prebolus was 4, whereas the average ratio of the full-bolus and prebolus LV lumen MTT was 3.7 ± 1.3, which suggests that the influence of dispersion is approximately equal for the prebolus and full-bolus. Taken together, the above considerations justified the reconstruction of the non-saturated AIF from four time-shifted prebolus curves.

Quantitative determination of myocardial perfusion proved highly repeatable in a cohort of healthy mice. An ANOVA for repeated measures revealed no difference in subsequent perfusion measurements and the between-session CV was only 6%. As a reference, in a longitudinal study of mouse myocardial infarction, the infarct perfusion values changed from 1 to 3 mL min^{-1} g^{-1} over time [15], which is much higher than the CV. Additionally, the inter-animal CV was 11 and 8% for the experiments at week 1 and 2, respectively. Healthy mouse myocardium has a perfusion of approximately 7 mL min^{-1} g^{-1} and changes in perfusion due to pathology, for example due to myocardial infarction, can be much higher than these inter-animal CV values. Fujii *et al.* observed a prominent increase in myocardial blood flow velocity, as a measure for perfusion, following ultrasound-targeted angiogenic-gene delivery in an infarct mouse model [16]. Our perfusion quantification method therefore seems not only suitable for longitudinally studying perfusion impairments in mouse models of myocardial disease, but potentially also to study the impact of promotion of angiogenesis on myocardial perfusion.

Previously, regional perfusion differences were reported using an arterial spin labeling (ASL) technique by Kober *et al.*, who observed a perfusion gradient between the septum and the lateral wall, dependent on the isoflurane levels employed for anesthesia [17]. Also, regional heterogeneity of myocardial perfusion has been observed using microsphere techniques in small animals and using first-pass perfusion MRI in humans [18,19]. The results from our measurements indeed suggest the presence of small regional perfusion differences, in particular between the septum and inferior wall as compared to the anterior and lateral wall. However, these differences did not reach statistical significance. Finally, somewhat larger variability of the perfusion estimates was observed in the lateral and inferior wall as compared to the septum and anterior wall, presumably due to a lower SNR in these regions caused by the use of a phased-array receive surface coil.

Isoflurane is well suitable for cine MRI in mice, because it has little influence on cardiac functional parameters [20]. However, isoflurane has vasodilatory properties, which could lead to a dose-dependent increase in mouse myocardial perfusion [17]. Therefore, anesthetic conditions were carefully controlled and monitored, which assured comparable experimental conditions between the different animals and the measurement sessions (Table 3.1). This is a common approach for preclinical myocardial perfusion studies. In mice, resting-state perfusion values under isoflurane anesthesia were measured ranging from 4.7 to 7.1 mL min^{-1} g^{-1} [15,17,21-23]. Also, using fluorescent microspheres and ketamine anesthesia a myocardial perfusion value of 6.4 ± 0.4 mL min^{-1} g^{-1} was found [24]. These values correspond to ours very well. Apart from resting-state perfusion it would be interesting to measure the perfusion under maximal vasodilation by pharmacological intervention to determine the perfusion reserve [17,25-27]. Since this experiment requires two dual-bolus infusions during one session, the effects of the resulting prolonged anesthesia duration and potential accumulation of Gd(DTPA)$^{2-}$ on the repeatability of the method need to be considered carefully.

A distinct advantage of the ASL technique is that myocardial perfusion maps are obtained, while analysis of first-pass perfusion data becomes more biased by noise for smaller regions-of-interest or when performing pixel-wise analysis [15,23,28-32]. On the other hand, obtaining accurate mouse myocardial T_1 maps is not straightforward, complicating perfusion quantification using ASL. Typical acquisition times of preclinical ASL measurements are long (25-60 min), although recently a method was presented to decrease this to 15 min [29]. In contrary, first-pass perfusion measurements are obtained in less than 2 minutes. This results in much shorter anesthesia duration for diseased mice and allows for easy incorporation of first-pass perfusion measurements into multi-parametric imaging protocols, for example containing a late gadolinium enhanced scan for infarct size quantification, cinematographic MRI to quantify LV systolic function or MR spectroscopy to quantify the energy status of the heart.

We have used a Fermi constrained deconvolution model to quantify myocardial perfusion. A recent study suggested that under resting conditions Fermi modeling performed equally well as two-compartment modeling, model-independent analysis and Patlak plot analysis [33]. Nevertheless, for robust performance of the Fermi modeling there are two basic assumptions that need to be addressed. First, it is required that the vascular-extravascular exchange of water is in the slow-exchange limit, i.e., the vascular and extravascular signals can be regarded as distinct [6]. It was estimated using various considerations that the peak concentration of Gd(DTPA)$^{2-}$ in the vascular compartment after injection of the 100 µL and 40 mM full-bolus is approximately 1.9 mM (see Appendix). With blood T_1 = 2400 ms, tissue T_1 = 1760 ms, and Gd(DTPA)$^{2-}$ r_1 = 4 mM^{-1} s^{-1} [34-36] the difference in vascular and extravascular relaxation rate constant becomes 7.4 s^{-1}, which is of similar magnitude as the vascular-extravascular water exchange rate constant 7 s^{-1} [36]. The vascular-extravascular exchange of magnetization is therefore in the intermediate-exchange regime. Nevertheless, the effects of water exchange are minimized by the MRI sequence with a short saturation time of 60 ms and therefore the assumption of slow exchange is justified. Second, it is required for Fermi fitting that during the first-passage of the bolus Gd(DTPA)$^{2-}$ remains in the vasculature. This condition may not have been fully satisfied in our experiments based on the following observation. For a full-bolus of 40 mM Gd(DTPA)$^{2-}$ we detected saturation of the LV lumen signal (Figure 3.6B), but for the same concentration the myocardial tissue response was not saturated (Figure 3.5B). This implies that contrast agent in the vascular compartment was diluted during myocardial passage, which may have resulted from extravasation of contrast agent from the vascular compartment or additional dispersion in the coronary bed. Two-compartment modeling may be used to include the effects of extravasation of Gd(DTPA)$^{2-}$ during first-passage [37].

There are some limitations to this study. First, absolute perfusion values were not validated by a gold-standard method, for example using fluorescent or radioactive microspheres [27]. The microsphere technique for mice is highly invasive and experimentally very difficult and we anticipate that validation of the perfusion values would require a large cohort of animals [23,27]. Moreover, regional differences in microsphere density, which are likely to occur in small mouse myocardial tissue sections complicate the validation [38]. We therefore chose to focus on the repeatability of the first-pass myocardial perfusion method and compare quantitative values to well-documented literature on perfusion in healthy mice. Second, the temporal resolution was limited to one image every 3 heartbeats. For accurate human myocardial perfusion quantification one image every heartbeat is considered imperative, since the bolus typically is delivered over only a few heartbeats [39]. Given the average mouse heart rate (513 min^{-1}), prebolus MTT (1.5 s) and full-bolus MTT (5.5 s) in our study, the first-passage of the prebolus and full-bolus were sampled with approximately 4 and 16 images, respectively. Therefore, the first-passage of both boluses was effectively captured, thus enabling repeatable perfusion quantification.

Conclusion

In summary, quantitative regional perfusion values with good repeatability were obtained in the healthy mouse myocardium with a first-pass perfusion MRI technique, using a dual-bolus approach in combination with a Fermi constrained deconvolution model for perfusion quantification. This method opens new opportunities to quantify regional perfusion deficits in various mouse models of cardiac pathology. Moreover, first-pass perfusion measurements could help quantify, for example, the impact of pro-angiogenic therapy on the perfusion in mouse models of myocardial infarction. Importantly, because of the short duration of the first-pass perfusion measurements, also complementary data can be obtained within the same examination, for example using cinematographic MRI, as well as T_1 and T_2 mapping.

Acknowledgement

This research was performed within the framework of the Center for Translational Molecular Medicine, project TRIUMPH (grant 01C-103), and supported by the Dutch Heart Foundation. This work was supported by VIDI grant (number: 700.58.421) from the Netherlands Organization for Scientific Research (NWO), and VIDI grant (number: 07952) from the Dutch Technology Foundation STW, applied science division of NWO and the Technology Program of the Ministry of Economic Affairs. We thank L.B.P. Niesen and D. Veraart for biotechnical assistance and Prof. C. Springer Jr. for critically reading the manuscript.

Appendix

Estimations of blood Gd(DTPA)$^{2-}$ concentration

After injection of a full-bolus in the tail vein the contrast agent is dispersed in the vasculature of the mouse. As a result, the peak Gd(DTPA)$^{2-}$ concentration in the LV lumen and coronary vasculature is considerably lower than the injection concentration (40 mM).

We have used two approaches to estimate the concentration of contrast agent in the coronary circulation after injection of a 100 µL full-bolus of 40 mM Gd(DTPA)$^{2-}$. First, the dilution can be estimated using the cardiac output of the left ventricle (µL s^{-1}) multiplied by the mean transit time (MTT) (s) of the bolus. The average cardiac output was 380 µL s^{-1} and the average MTT 5.5 s. Therefore, the full-bolus containing 40 mM Gd(DTPA)$^{2-}$ is diluted approximately (380 x 5.5)/100 ≈ 21 times, resulting in an average Gd(DTPA)$^{2-}$ concentration of about 1.9 mM.

Second, the peak Gd(DTPA)$^{2-}$ concentration can be estimated from the LV lumen signal intensity time curves of two low-dose bolus injections, which differ in volume by a factor 2, as described by Epstein *et al.* [14]. Assuming that the MTTs of both boluses are equal, which holds if the dispersion of the bolus is large as compared to the injection time, and that the peak amplitudes of the boluses scale with injection volume, peak Gd(DTPA)$^{2-}$ concentration can be estimated from

$$c_{LV}(t) \approx \frac{nM_0 s(t)}{CO\int s(t)dt} \qquad [1]$$

Here, C_{LV}(t) is the Gd(DTPA)$^{2-}$ concentration at time *t,* CO is the cardiac output (mL s^{-1}), M_0 the number of mmol of Gd(DTPA)$^{2-}$, *n* is the injection volume ratio of the two bolus injections, and *s*(t) is the signal intensity time curve of the bolus with the lowest volume. Four 25 µL (15 mM Gd(DTPA)$^{2-}$, MTT = 1.5 s) and four 50 µL (15 mM Gd(DTPA)$^{2-}$, MTT = 1.9 s) boluses were injected in a separate cohort of mice (Figure 3.10). From the resulting normalized signal intensity time curves in Figure 3.10 and Equation 1, we estimated that the LV lumen blood peak Gd(DTPA)$^{2-}$ concentration for the full 100 µL bolus containing 40 mM was 1.8 mM, in excellent agreement with the estimation based on cardiac output.

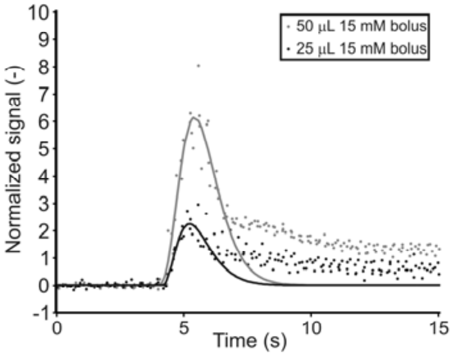

Figure 3.10. Averaged signal intensity time curves in the LV lumen of the four 25 µL and four 50 µL, 15 mM bolus injections. The solid lines are γ-variate fits to the data.

References

1. Atkinson, D.J., et al. Radiology, 1990, 174(3 Pt 1), 757-62.
2. Jerosch-Herold, M. J Cardiovasc Magn Reson, 2010, 12, 57.
3. Kellman, P., Arai A.E. J Cardiovasc Magn Reson, 2007, 9(3), 525-37.
4. Greenwood, J.P., et al. Lancet, 2012, 379(9814), 453-60.
5. Coolen, B.F., et al. Magn Reson Med, 2010, 64(6), 1658-63.
6. Jerosch-Herold, M., et al. Med Phys, 1998, 25(1), 73-84.
7. Canet, E., et al. J Magn Reson Imaging, 1995, 5(4), 411-5.
8. Köstler, H., et al. Magn Reson Med, 2004, 52(2), 296-9.
9. Heijman, E., et al. NMR Biomed, 2007, 20(4), 439-47.
10. Schneider, J.E., et al. J Cardiovasc Magn Reson, 2006, 8(5), 693-701.
11. Cerqueira, M.D., et al. Circulation, 2002, 105(4), 539-42.
12. Bland, J.M., Altman D.G. Lancet, 1986, 1(8476), 307-10.
13. Ishida, M., et al. J Cardiovasc Magn Reson, 2011, 13, 28.
14. Epstein, F.H., et al. Magn Reson Med, 2002, 47(3), 482-91.
15. Vandsburger, M.H., et al. Magn Reson Med, 2010, 63(3), 648-57.
16. Fujii, H., et al. J Am Coll Cardiol Img, 2009, 2(7), 869-79.
17. Kober, F., et al. Magn Reson Med, 2005, 53(3), 601-6.
18. Stapleton, D.D., et al. Microcirculation, 1995, 2(3), 277-82.
19. Muehling, O.M., et al. J Cardiovasc Magn Reson, 2004, 6(2), 499-507.
20. Roth, D.M., et al. Am J Physiol Heart Circ Physiol, 2002, 282(6), H2134-H40.
21. Antkowiak, P., et al. J Cardiovasc Magn Reson, 2010, 12(Suppl 1), M10.
22. Makowski, M., et al. Magn Reson Med, 2010, 64(6), 1592-8.
23. Streif, J.U.G., et al. Magn Reson Med, 2005, 53(3), 584-92.
24. Trabold, F., et al. Hypertension, 2002, 40(1), 90-5.
25. Petersen, S.E., et al. Circulation, 2007, 115(18), 2418-25.
26. Hoenig, M.R., et al. Curr Vasc Pharmacol, 2008, 6(4), 292-300.
27. Jacquier, A., et al. NMR Biomed, 2011, 24(9), 1047-53.
28. Zarinabad, N., et al. Magn Reson Med, 2012, 68(6), 1994-2004.
29. Campbell-Washburn, A.E., et al. Magn Reson Med, 2012, 69(1), 238-47.
30. Kober, F., et al. Magn Reson Med, 2004, 51(1), 62-7.
31. Belle, V., et al. J Magn Reson Imaging, 1998, 8(6), 1240-5.
32. Vandsburger, M.H., et al. Eur Heart J, 2007, 28(22), 2792-8.
33. Pack, N.A., DiBella E.V.R. Magn Reson Med, 2010, 64(1), 125-37.
34. Coolen, B.F., et al. NMR Biomed, 2011, 24(2), 154-62.
35. Dobre, M.C., et al. Magn Reson Imaging, 2007, 25(5), 733-5.
36. Donahue, K.M., et al. Magn Reson Med, 1994, 32(1), 66-76.
37. Tofts, P.S., et al. J Magn Reson Imaging, 1999, 10(3), 223-32.
38. Decking, U.K.M., et al. Am J Physiol Heart Circ Physiol, 2004, 287(3), H1132-H40.
39. Kroll, K., et al. Am J Physiol, 1996, 271(4 Pt 2), H1643-55.

4

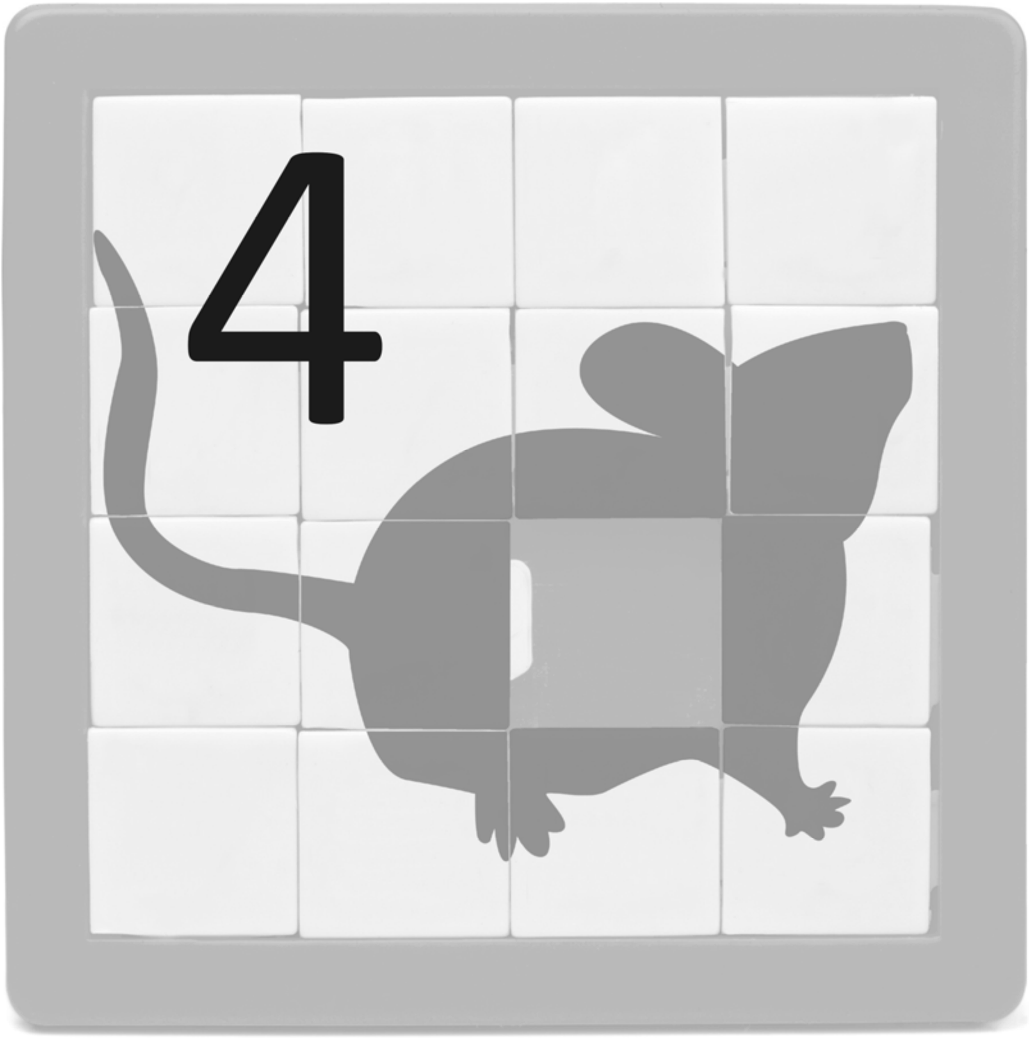

Myocardial perfusion MRI shows impaired perfusion of the mouse hypertrophic left ventricle

Bastiaan van Nierop, Bram Coolen, Wouter Dijk,
Elza van Deel, Dirk Duncker, Klaas Nicolay,
and Gustav Strijkers

Abstract

Background: There is growing consensus that myocardial perfusion deficits play a pivotal role in the transition from compensated to overt decompensated hypertrophy. Thus far myocardial perfusion deficits were not systematically studied in the highly relevant model of pressure overload induced hypertrophy and heart failure by transverse aortic constriction (TAC).

Methods: Regional left ventricular (LV) myocardial perfusion (mL min^{-1} g^{-1}) was assessed in healthy mice (n = 6) and mice with TAC (n = 14). A dual-bolus first-pass perfusion MRI technique was employed to longitudinally quantify myocardial perfusion values between one and ten weeks after surgery. LV function and morphology were quantified from cinematographic MRI.

Results: Myocardial rest perfusion values in both groups did not change significantly over time, in line with the essentially constant global LV function and mass. Myocardial perfusion was significantly decreased in TAC mice (4.2 ± 0.9 mL min^{-1} g^{-1}) in comparison to controls (7.6 ± 1.8 mL min^{-1} g^{-1}) ($P = 0.001$). No significant regional differences in perfusion were observed within the LV wall. Importantly, increased LV volumes and mass, and decreased ejection fraction correlated with decreased myocardial perfusion ($P < 0.001$, in all cases). Total LV blood flow was decreased in TAC mice (0.5 ± 0.1 mL min^{-1}, $P < 0.001$) in comparison to control mice (0.7 ± 0.2 mL min^{-1}).

Conclusion: Myocardial perfusion in TAC mice was significantly reduced as compared to healthy controls. Perfusion was proportional to LV volume and mass, and related to decreased LV ejection fraction. Furthermore, this study demonstrates the potential of quantitative first-pass contrast-enhanced MRI for the study of perfusion deficits in the diseased mouse heart.

Introduction

Heart failure (HF) is a progressive syndrome in which the heart is no longer capable of pumping blood at a rate commensurate with the peripheral needs [1]. HF is an important cause of morbidity and mortality worldwide [2-4]. In many patients HF results from sustained, systemic hypertension resulting in chronic left ventricular (LV) pressure overload [5]. The heart initially adapts to this overload by means of hypertrophic growth. However, a broad range of concomitant maladaptive processes, including increased collagen deposition, metabolic changes and microvascular remodeling, eventually may lead to HF [6-8].

It has long been appreciated that pressure-overload induced LV hypertrophy is associated with alterations in the coronary microvasculature [9-12]. The pressure-overload hypertrophied LV is characterized by perivascular fibrosis and arterial medial hypertrophy, while vascular densities are lower as neovascularization does not occur commensurate with myocardial growth [13,14]. These abnormalities force the myocardium to recruit its vasodilator reserve already under resting conditions, which occurs at the expense of its ability to increase myocardial blood flow in response to a stressor or vasodilator [15-17]. The resultant myocardial perfusion abnormalities during increased oxygen demands likely have a negative impact on cardiac function. However, the precise role of impaired perfusion in the development of HF remains incompletely understood. For example, it is unclear whether impaired perfusion is merely a consequence of hypertrophy or actually drives maladaptive remodeling.

Transverse aortic constriction (TAC) in mice is a highly relevant model of pressure overload induced hypertrophy and plays an important role in preclinical research to unravel the precise role of microvascular dysfunction in HF development [17-21]. The relationship of LV hypertrophy and decline in LV function with regional changes in myocardial perfusion is not well established for this model. One reason might be that quantitative myocardial perfusion measurements in mice are experimentally very challenging. Furthermore, classical microsphere-based perfusion quantification in the mouse heart is invasive and therefore conducted under non-physiological conditions [22,23]. Also, the latter suffers from sampling errors due to the small mouse heart size [24].

Recently, first-pass perfusion MRI protocols have become available enabling noninvasive quantification of mouse heart perfusion values (in mL min^{-1} g^{-1}) *in vivo* [25,26]. Makowski *et al.* already showed a significantly decreased perfusion in the mouse infarct area in comparison to other heart wall segments [26]. More recently, we showed that the first-pass perfusion measurements are highly repeatable and that one can determine heart anatomy and function during the same MRI session [27]. This offers the unique opportunity to relate microvascular, functional and hypertrophic adaptations in the same mouse under identical conditions in a longitudinal fashion.

The aim of this study was therefore to apply first-pass perfusion MRI to quantify LV regional myocardial perfusion in a cohort of healthy mice and littermates that underwent TAC resulting in LV pressure overload induced hypertrophy. Perfusion values were related to global LV function and morphology as obtained from cinematographic MRI. Measurements were performed 1, 2, 4, 7 and 10 weeks after TAC.

Methods

Animal handling

A total of 20 C57BL/6 mice (♂, age 11 weeks, 24-26 grams) were included in this study. Animals were housed under standard laboratory conditions with a 12 hour light/dark cycle and were maintained on a standard diet with access to water *ad libitum*. All animal experiments were performed according to the Directive 2010/63/EU of the European Parliament and approved by the Animal Care and Use Committee of Maastricht University.

Animal model

Mice were randomly separated in a control group (n = 6) and a group that was subjected to TAC (n = 14), resulting in LV pressure overload [21,28]. Briefly, mice were anesthetized with 2.5 vol% isoflurane in 0.2 L min^{-1} O_2 and 0.2 L min^{-1} medical air and intubated for mechanical ventilation. Animals were placed on a heating pad to maintain body temperature at 37 °C. Buprenorphine (0.1 mg/kg s.c.) was administered for analgesia. Surgical procedures were performed using a stereo microscope (Leica M80). A small incision was made just lateral from the sternum above the first intercostal space. The aortic arch was exposed and tied off (6-0 silk suture) together with a 27G (Ø 0.42 mm) needle between the innominate artery and the left common carotid artery. The needle was immediately removed, restoring blood flow. The chest was then closed and the animals were allowed to recover in a 30 °C recovery chamber.

MR examinations

All MR images were acquired as previously described [25,27,29]. Briefly, a 9.4 T small animal MRI scanner (Bruker BioSpec, Ettlingen, Germany) was used equipped with a 740 mT/m gradient coil. A 72-mm-diameter quadrature transmit coil was used in combination with a 4 element phased-array receive coil (Bruker). Mice were anesthetized with isoflurane (4.0 vol% for induction, 1.5-2.0 vol% for maintenance) in medical air (0.4 L min^{-1}). The front paws were placed on ECG electrodes and a balloon pressure sensor was placed on the abdomen. Body temperature was maintained at 36-37^{o}C with a heating pad and monitored with a rectal temperature sensor. An infusion pump (Chemyx Fusion 100, flow rate: 2 mL min^{-1}) was used to ensure repeatable tail vein infusion of Gd(DTPA)$^{2-}$ (Bayer HealthCare Pharmaceuticals, Mijdrecht, The Netherlands) in 0.9% NaCl. Four-chamber, long-axis first-pass perfusion images were acquired using an ECG-triggered, segmented saturation-recovery FISP sequence, with the following acquisition parameters: pulse repletion time (TR) = 1.18 ms, echo time (TE) = 0.51 ms, field of view = 3X3 cm^{2}, matrix = 64X39 (3 segments, acquired over three consecutive heart beats), GRAPPA parallel acceleration factor = 1.64, reconstruction matrix = 128x128, slice thickness = 1.5 mm, excitation pulse (0.3 ms Gauss pulse, α = 15°), saturation pulse (2 ms Gauss pulse, α = 90°).

Study protocol

MRI measurements were performed 1, 2, 4, 7 and 10 weeks after surgery. At each session first-pass perfusion images were acquired with a prebolus (25 µL, 40 mM Gd(DTPA)$^{2-}$) and a full-bolus (100 µL, 40 mM Gd(DTPA)$^{2-}$). Perfusion quantification was successful in 29/30 measurements in control mice and 59/70 in TAC mice. Missing measurements were caused by death of mice in between measurements, unsuccessful contrast agent infusion or poor first-pass MR image quality as a result of ECG distortions. In between both boluses a 20 min waiting time ensured sufficient clearance of Gd(DTPA)$^{2-}$ [27]. LV function and mass were quantified during these 20 min. To this end 2 long-axis and a stack of 5 short-axis cinematographic (cine) MR images were obtained with 15-18 frames covering the complete cardiac cycle using an ECG-triggered and respiratory-gated FLASH sequence, as described previously [30,31]. Immediately after the last measurements the anesthetized animals were killed by means of perfusing the vascular bed with phosphate buffered saline (10 mL, pH 7.4) infused via a needle penetrating the apex and exsanguination from the vena cava inferior. Next, the integrity of the TAC was visually verified and heart wet weight, lung wet weight (LuW), and tibia length (TL) were measured.

Data analysis

Myocardial perfusion (mL min^{-1} g^{-1}) was quantified as described in more detail previously [27]. Briefly, signal intensity (SI) time curves from the LV blood pool and the LV myocardium were obtained from a conservative segmentation using home-built software in Matlab (The Mathworks, Inc.). The regions-of-interest were slightly adjusted per frame to correct for small position changes of the heart due to respiration. Pre-injection baseline signal intensity was subtracted from the signal intensity time curve and subsequently the curves were normalized to the pre-injection baseline signal to correct for signal reception inhomogeneities introduced by the RF receive surface coil. For perfusion quantification in the LV tissue, a non-saturated AIF was reconstructed from four time-shifted γ-variate prebolus fits [32]. Next, myocardial tissue perfusion was quantified using a Fermi constrained deconvolution of the myocardial tissue response from the full-bolus with the AIF using a Levenberg-Marquardt least squares fitting algorithm [33]. For regional perfusion analysis the LV myocardium was divided in five segments (Figure 4.1) [34]. From the γ-variate fittings also the mean transit time (MTT) and the area under the curve (AUC) were extracted. The myocardial wall was segmented semi-automatically in the cine MR images using CAAS MRV FARM (Pie Medical Imaging, The Netherlands) to obtain LV function and mass [35]. Whole heart blood flow was calculated by multiplying perfusion with LV mass. Myocardial stroke work was estimated by multiplying stroke volume and mean aortic pressure proximal to the TAC, using 83 ± 5 mmHg in control and 83 ± 4 mmHg in TAC mice based on data from van Deel *et al.* [21]. Finally, the relationship between the cardiac output (CO) and the concentration of the contrast agent over the first-pass $c_a(t)$ was assessed using the Stewart-Hamilton equation [36]

$$CO = \frac{M}{\int c_a(t)dt} \tag{1}$$

in which M is the injected amount of the tracer.

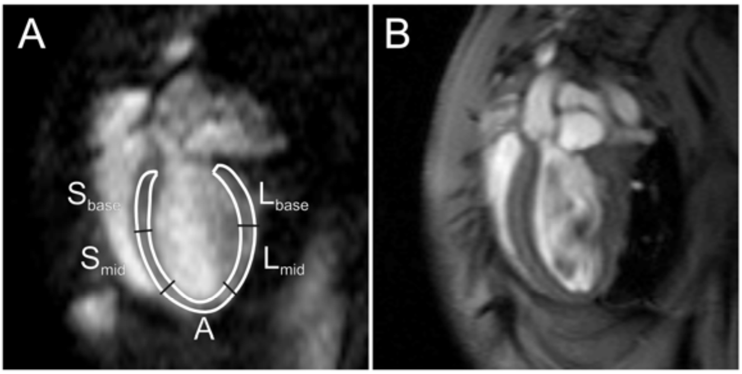

Figure 4.1. (A) Four-chamber long-axis image during diastole overlaid with endocardial and epicardial contours and the five segments used for regional quantification of myocardial perfusion. S_{base} = septum (basal part), S_{mid} = septum (midventricular part), A = apex, L_{base} = lateral wall (basal part), L_{mid} = lateral wall (midventricular part). (B) Corresponding cinematographic diastolic four-chamber long-axis image.

Statistics

Data are expressed as mean ± standard deviation (SD). Differences in LV mass/TL, LVEF, stroke volume (SV), cardiac output (CO), heart rate (HR), respiratory rate (Resp) and bodyweight (BW) were tested for statistical significance with an ANOVA for repeated measures with group being control and TAC as factor, followed by the Bonferroni post-hoc test when appropriate. In case of interaction between time and group, the effect of time was tested separately per group. Differences in perfusion were tested for statistical significance with an ANOVA for repeated measures with region and group as factor, followed by the Bonferroni post-hoc test when appropriate. In TAC mice only linear regression analysis with offset was used to relate myocardial perfusion to LV parameters (EDV, ESV, EF, and LVmass), to relate blood flow to CO, and to stroke work. Changes in LuW/TL, HW/TL, blood flow, and blood flow to the heart as percentage of CO were tested for statistical significance with a one-sided Student's *t*-test. Calculations were performed using SPSS 19.0 (SPSS Inc., Chicago). For all tests the level of significance was set at $\alpha = 0.05$.

Results

All control mice completed the experimental protocol. Two mice died during the course of the experiment at 2 and 7 weeks after TAC, respectively. General animal characteristics are given in Table 4.1. Mouse bodyweight increased over time ($P < 0.001$), however, no significant differences between groups were detected. No differences in heart rate or respiratory rate as measured during MRI scanning were detected between control and TAC mice.

LV functional parameters were determined from cinematographic MR images (Figure 4.2). Impaired systolic function in the TAC mice was apparent from an increased EDV ($P < 0.01$) and ESV ($P < 0.01$), and a decreased EF ($P < 0.001$) as compared to control mice (Figure 4.3). In TAC mice EDV increased over time from 78 ± 10 µL to 92 ± 19 µL ($P < 0.01$), whereas ESV (53 ± 14 µL) and EF (39 ± 8%) remained constant over time. No significant changes over time were detected for EDV (70 ± 11 µL), ESV (25 ± 8 µL) and EF (65 ± 6%) in the control mice. Myocardial hypertrophy in TAC mice was apparent from an increased LV mass normalized to TL as compared to controls ($P < 0.001$). In control mice LV mass normalized to TL (5.3 ± 0.4 mg/mm) remained constant over time, whereas LV mass in TAC mice gradually increased ($P < 0.001$) from 6.1 ± 0.8 mg/mm (week 1) to 7.4 ± 0.9 mg/mm (week 10). Moreover, SV was decreased in TAC mice (33 ± 7 µL) as compared to control mice (45 ± 7 µL) ($P < 0.001$), and CO was also decreased in TAC mice (17 ± 3 mL min^{-1}) as compared to controls (23 ± 3 mL min^{-1}) ($P < 0.001$). No significant changes over time were detected in both groups for SV and CO.

Table 4.1. Mouse body weight measured before the MRI measurements, and heart rate and respiratory rate as determined during the MRI measurements at the different time points in the study. Bodyweight = BW, HR = heart rate, Resp = respiratory rate. For all parameters no differences between groups were detected. BW increased over time ($P < 0.001$), HR was constant over time, but Resp at week 2 was somewhat lower as compared to week 3 and 5 ($P < 0.05$).

	Weeks	**1**	**2**	**4**	**7**	**10**
BW (g)	Control	25.9 ± 2.0	26.7 ±1.6	26.8 ± 1.4	27.1 ± 1.5	29.0 ± 1.7
	TAC	24.6 ± 1.6	25.6±1.4	26.3 ± 1.0	26.9 ± 1.1	27.6 ± 1.2
HR (min^{-1})	Control	515 ± 43	523 ± 29	503 ± 35	550 ± 31	524 ± 39
	TAC	529 ± 40	534 ± 25	545 ± 23	539 ± 46	531 ± 28
Resp (min^{-1})	Control	63 ± 8	48 ± 4	71 ± 16	58 ± 7	62 ± 11
	TAC	58 ± 9	56 ± 9	68 ± 9	63 ± 11	69 ± 12

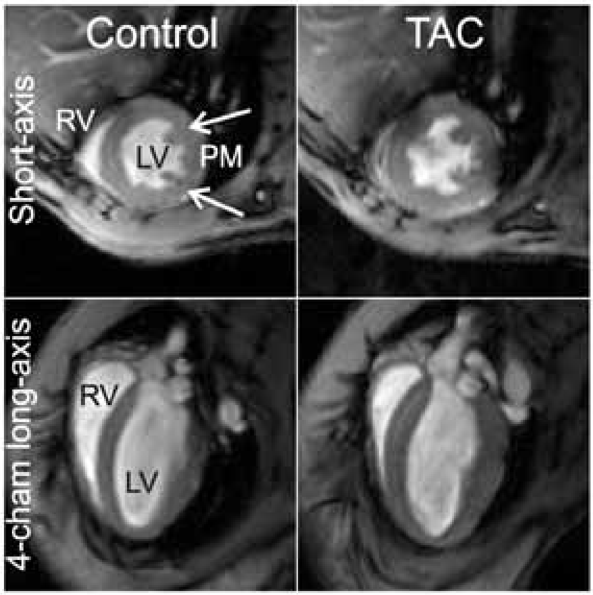

Figure 4.2. Representative end-diastolic short-axis and long-axis images from a control heart and a TAC heart obtained 10 weeks after surgery.

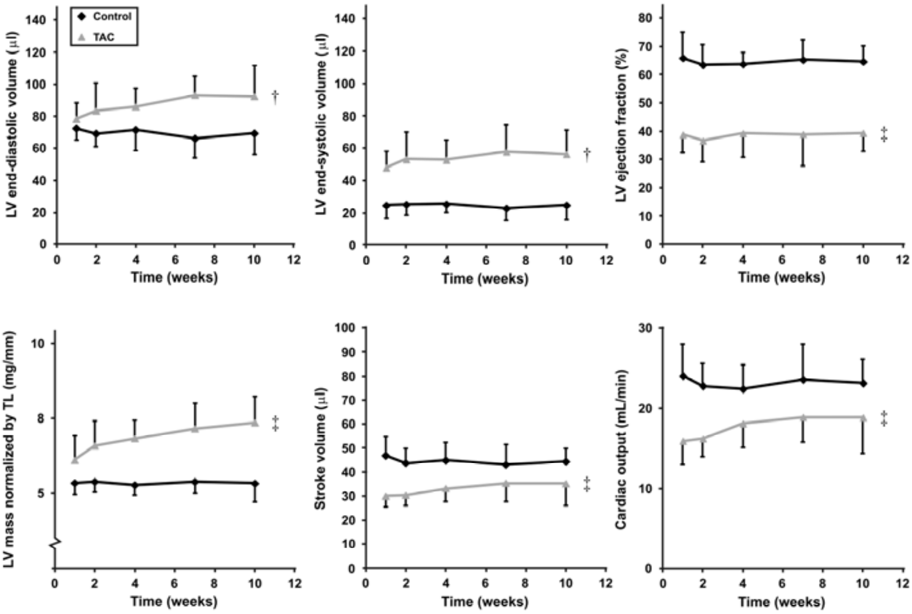

Figure 4.3. Left ventricular (LV) end-diastolic volume (top left), end-systolic volume (top middle), ejection fraction (top right), LV mass normalized to tibia length (TL) (bottom left), stroke volume (bottom middle) and cardiac output (bottom right) in control and TAC mice as a function of time. End-diastolic volume ($P < 0.01$) and end-systolic volume ($P < 0.01$) were increased in TAC mice pointing to LV dilatation as compared to controls. Impaired systolic function in TAC mice was apparent from a decreased ejection fraction ($P < 0.001$) as compared to controls. LV hypertrophy in TAC mice was apparent from increased LV mass normalized to TL as compared to controls ($P < 0.001$). Both stroke volume and cardiac output were decreased as a result of TAC ($P < 0.001$) as compared to controls. Moreover, in TAC mice end-diastolic volume ($P < 0.01$) and LV mass ($P < 0.001$) gradually increased over time. Mean and SD per time point are denoted by the corresponding symbol and error bars. Statistical differences as compared to the control group are indicated by † ($P < 0.01$) and ‡ ($P < 0.001$).

Post-mortem whole heart weight was increased in TAC mice as compared to controls (*P* < 0.001) (Table 4.2). LuW/TL ratio, which was used as a measure for pulmonary remodeling, was only increased in three TAC mice. As a result, the apparent increase of LuW/TL in TAC mice did not reach statistical significance.

Table 4.2. Three TAC mice developed a large lung weight-to-tibia length (LuW/TL) ratio (mg/mm) of 18.2, 23.3 and 33.5 mg/mm as compared to 10.6 ± 1.7 mg/mm for the other mice in the group. This resulted in a slightly elevated group-averaged LuW/TL ratio in the TAC mice, but the differences did not reach statistical significance (P = 0.11). Heart mass as determined post mortem normalized to TL (mg/mm) was increased in TAC mice as compared to controls.

Group	Heart mass/TL (mg/mm)	LuW/TL (mg/mm)
Control	9.3 ± 0.9	10.0 ± 0.9
TAC	13.2 ± 1.8‡	13.7 ± 7.0

Statistical differences as compared to the control group are indicated by ‡ (*P* < 0.001).

A series of representative myocardial first-pass perfusion images of a prebolus and full-bolus experiment in a control and a TAC mouse are shown in Figure 4.4. The pictures depict images acquired before and at different time points after injection of a small and a relatively large quantity of the contrast agent, respectively. Blood and myocardial signals were appropriately nulled before contrast agent injection. For both the prebolus and full-bolus measurements one can observe the arrival of the contrast agent in the right ventricle, in the left ventricle, and in the myocardium. For the prebolus only minor signal enhancement was observed in the myocardium and signal intensity in the whole image returned quickly to values close to baseline levels, indicating strong dilution and fast clearance of the low volume prebolus.

The mean transit time (MTT) characterizes the average time the tracer requires to pass through a region of interest. MTTs of the LV lumen signal from the prebolus in the control mice (1.3 ± 0.5 s) and TAC mice (1.4 ± 0.6 s) were not significantly different. Also, the MTT of the LV lumen signal from the full-bolus in the control mice (4.8 ± 0.7 s) and TAC mice (4.5 ± 0.6 s) were statistically the same.

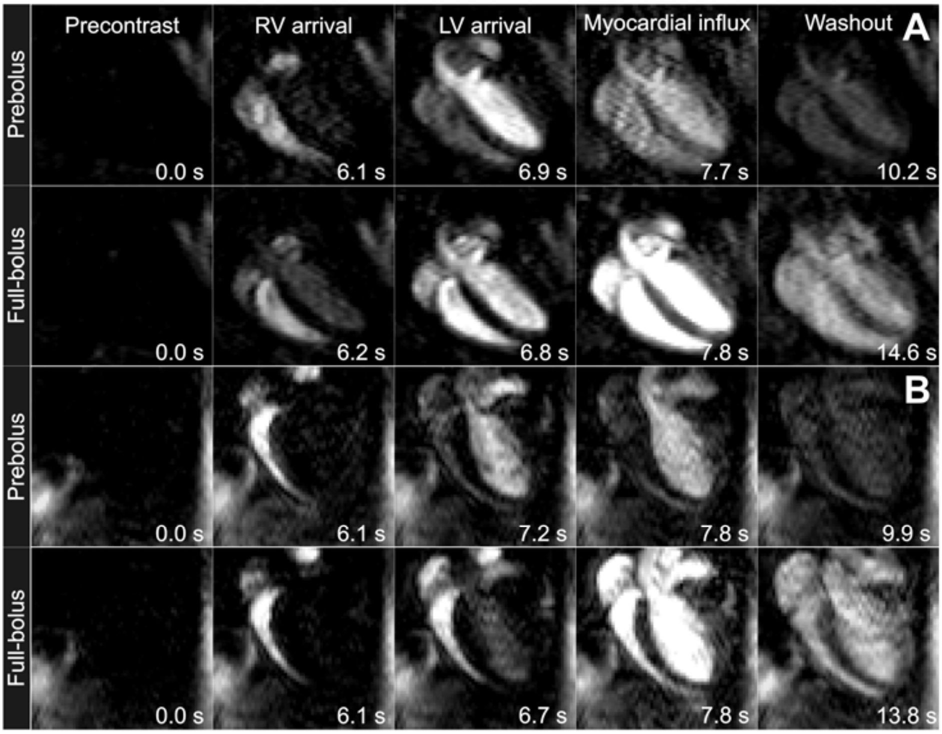

Figure 4.4. Time series of cardiac images obtained during the first-passage of a prebolus (25 µL, 40 mM Gd(DTPA)$^{2-}$) and a full-bolus (100 µL, 40 mM Gd(DTPA)$^{2-}$) in a control (two top rows) and TAC mouse (two bottom rows). From left to right: precontrast, RV arrival, LV arrival, myocardial influx, and washout. Indicated are the time points at which each image was acquired with respect to the precontrast image.

Figure 4.5A displays two examples of arterial input functions (AIF) for a control and a TAC mouse, which served as input for the Fermi analysis to model the measured myocardial tissue response and quantify the perfusion. The TAC mouse AIF was notably higher than that of the control mouse, which was also the case for the group averaged areas under the curve as a measure of the AIF amplitude (61.9 ± 32.5 versus 41.2 ± 9.9 for TAC and controls, respectively). The higher AIF was related to a decreased CO for TAC mice via the Stewart-Hamilton relationship (Equation 1), which is shown for all mice in Figure 4.5B.

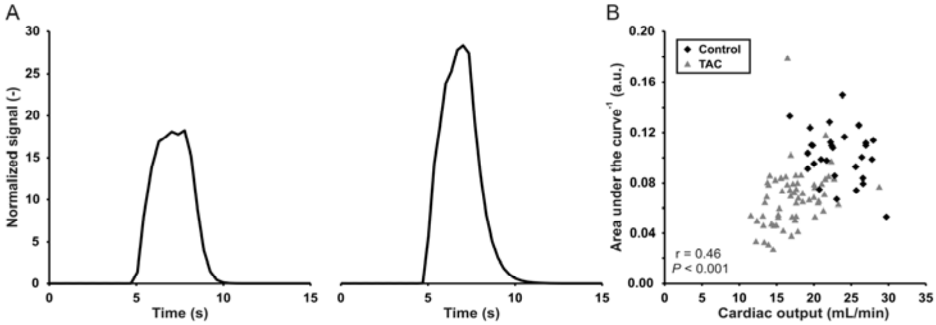

Figure 4.5. (A) Examples of an arterial input function (AIF) in a control (left) and TAC mouse (right), which were reconstructed from the prebolus intensity-time curves. The AUC in the AIF of the TAC mouse was larger as compared to the one in the control mouse. (B) Relationship between the cardiac output and the reciprocal of the area under the curve (AUC) in control and TAC mice for the prebolus injection. When assuming a linear relationship between both parameters, a moderate relationship was obtained (r = 0.46, *P* < 0.001).

Having established that prebolus and full-bolus injections in both groups of mice resulted in consistent signal-intensity time curves with similar MTTs and AIFs that followed the Stewart-Hamilton relation, myocardial tissue perfusion (in mL min^{-1} g^{-1}) was quantified regionally for each mouse. Figure 4.6 shows fits of the regional myocardial tissue response curves for two representative cases of a control and a TAC mouse.

Figure 4.7 summarizes the group-averaged regional perfusion values as function of time for TAC and control mice. Overall, no significant changes of myocardial perfusion with time were detected for both TAC and control hearts. No regional differences in perfusion values within the two groups were observed. Unexpectedly, low perfusion values were found in some segments in control mice at week 4, which we attribute to experimental difficulties at that specific time point (see Discussion). Most importantly, myocardial perfusion in TAC mice was consistently lower than in control mice. Region- and time-averaged perfusion in TAC mice was 4.2 ± 0.9 mL min^{-1} g^{-1}, while 7.6 ± 1.8 mL min^{-1} g^{-1} for controls (*P* = 0.001).

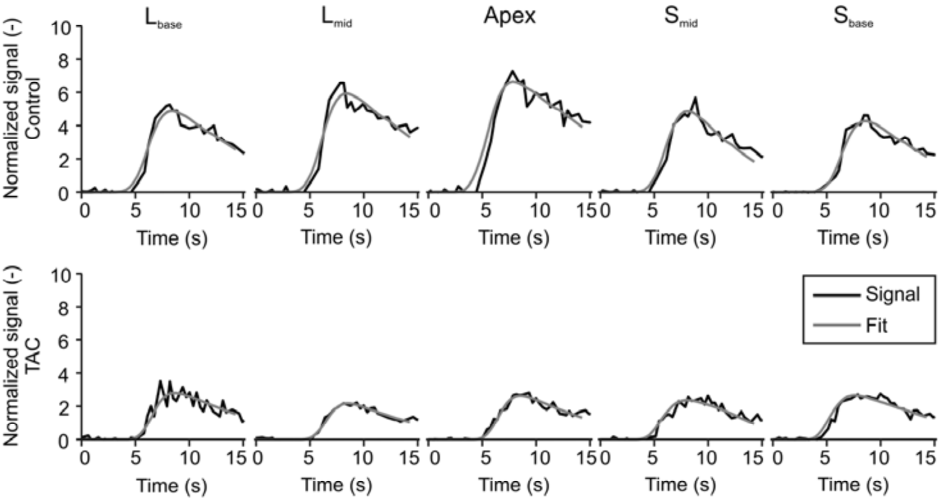

Figure 4.6. Measured myocardial tissue responses in the five wall segments and the corresponding modeled signal responses, obtained from the Fermi-constrained deconvolution of the myocardial tissue responses with the AIF in control (top row) and TAC mice (bottom row). S_{base} = septum (basal part), S_{mid} = septum (midventricular part), A = apex, L_{base} = lateral wall (basal part), L_{mid} = lateral wall (midventricular part). These segments are depicted in Figure 4.1.

In order to examine the relationship between the observed decreased perfusion values to the severity of hypertrophy and decline in function in individual mice, perfusion values of the entire LV were correlated to several functional parameters in Figure 4.8. Decreased myocardial perfusion in TAC mice was correlated to increased LV mass (r = -0.52, $P < 0.001$), increased LV EDV (r = -0.54, $P < 0.001$), increased ESV (r = -0.61, $P < 0.001$), and decreased LVEF (r = 0.51, $P < 0.001$). Whole heart blood flow, calculated by multiplying perfusion with LV mass as measure for the total amount of blood supplied to the LV, was decreased in TAC mice (0.5 ± 0.1 mL min^{-1}) as compared to control mice (0.7 ± 0.2 mL min^{-1}) ($P < 0.001$), but whole heart blood flow in TAC mice was not associated with a decreased CO ($P > 0.05$). The reduction in blood flow to the heart expressed as percentage of the CO in TAC mice (2.9 ± 0.7%) as compared to controls (3.2 ± 0.9%) showed a trend towards significance ($P = 0.07$). Myocardial stroke work, i.e., the work done by the LV to pump a certain amount of blood into the aorta, was estimated by multiplying stroke volume and mean aortic pressure, as measure for the force delivered by the LV. Stroke work in TAC mice (2728 ± 540 µL·mmHg) was decreased as compared to control mice (3681 ± 583 µL·mmHg, $P < 0.001$), but myocardial stroke work in TAC mice was not significantly correlated to blood flow (Figure 4.8).

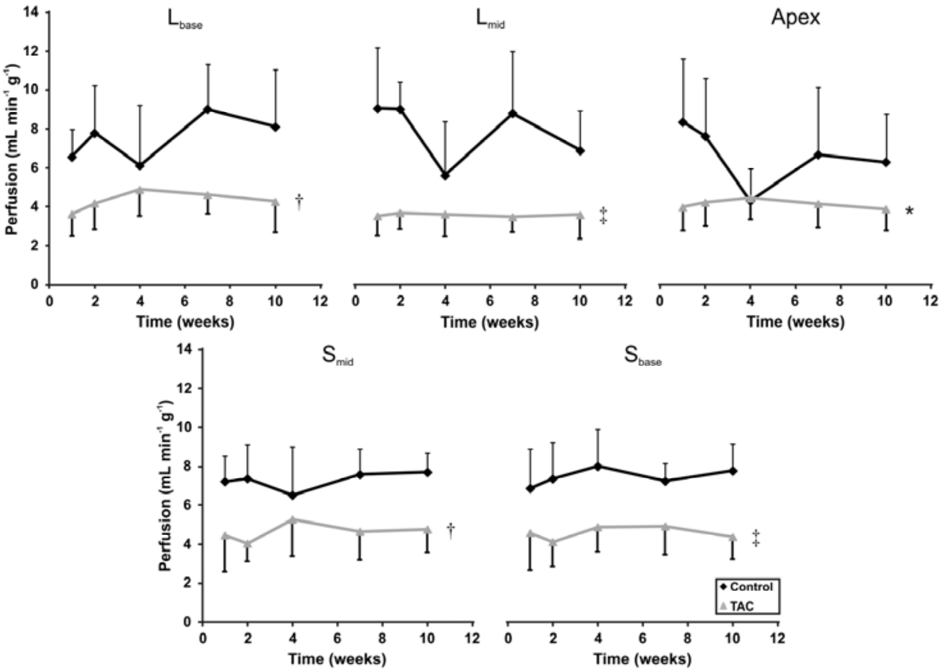

Figure 4.7. Myocardial perfusion in the five wall segments in control and TAC mice as a function of time. S_{base} = septum (basal part), S_{mid} = septum (midventricular part), A = apex, L_{base} = lateral wall (basal part), L_{mid} = lateral wall (midventricular part). Perfusion in the TAC mice was decreased in all segments as compared to control mice ($P < 0.05$, in all cases). In both groups no significant changes over time and between segments were observed. Low perfusion values were found in the lateral wall and the apex in control mice at week 4, which was attributed to experimental difficulties (see Discussion). Mean and SD per time point are denoted by the corresponding symbol and error bars. Statistical differences as compared to the control group are indicated by * ($P < 0.05$), † ($P < 0.01$) and ‡ ($P < 0.001$).

Discussion

The TAC mouse is a well-established and valued model for hypertrophy and HF and has been used for studying various aspects of vascular remodeling in myocardial disease [17-21]. Despite considerable efforts the precise mechanistic role of decreased myocardial perfusion in the development of HF is not fully elucidated. In particular, the relationship between myocardial perfusion and the evolution and severity of decline in LV function in this important mouse model has not been addressed thus far. In this study we therefore investigated the effect of LV pressure overload induced hypertrophy on myocardial perfusion in the TAC mouse model using quantitative first-pass perfusion MRI, and related the perfusion data to the severity and time-course of global left ventricular dysfunction.

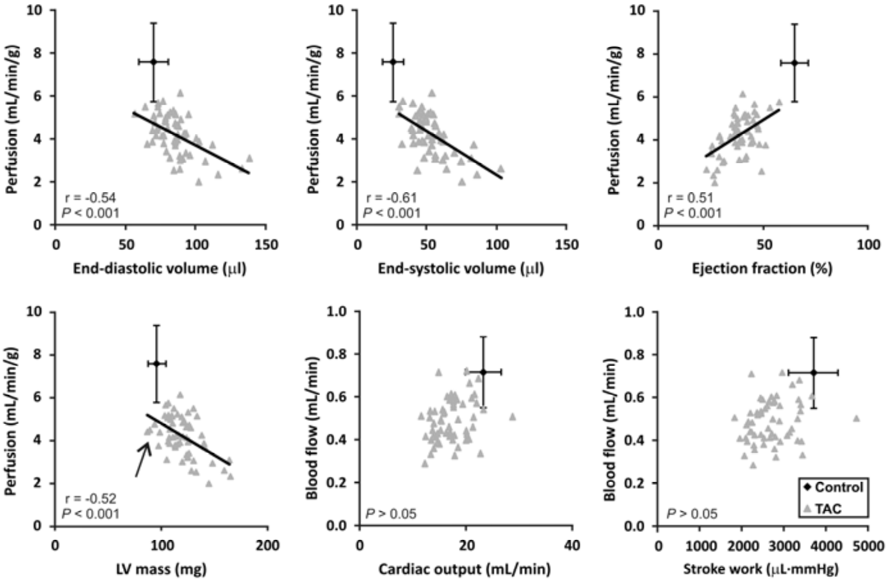

Figure 4.8. Relationship between average myocardial perfusion (mL min^{-1} g^{-1}) in individual hearts and the left ventricular end-diastolic volume (top left), end-systolic volume (top middle), ejection fraction (top right) and LV mass (bottom left), and between the whole heart blood flow and the cardiac output (bottom middle), and the stroke work (bottom right). Whole heart perfusion was calculated by multiplying left ventricular perfusion with LV mass. Stroke work was calculated by multiplying stroke volume with the estimated mean aortic pressure. The mean and SD for the control mice are denoted by the corresponding symbol and error bars. For TAC mice all individual measurement points are shown and the results (Pearson correlation coefficient and significance) of the linear regression analysis are shown in the bottom left of each panel.

Hypertrophy in the TAC mice was apparent from a significantly increased LV mass, while considerably increased EDV and ESV denoted LV dilation. Moreover, LV function in TAC mice was compromised, indicated by decreased EF, SV, and CO. Profound pulmonary remodeling, as assessed from the LuW/TL ratio, was only observed in three out of fourteen TAC mice. Taken together, from the anatomical data and MRI measurements it can be concluded that the TAC surgery resulted in a state of stable cardiac dysfunction rather than progressive HF.

Myocardial perfusion was studied under resting conditions, i.e., the vasculature was not maximally vasodilated. Under these conditions, perfusion values in TAC mice were almost two-fold lower than that for control mice. Group-averaged perfusion values in both groups were found to be constant over time. The apparent decrease of myocardial perfusion observed at week 4 in the apex and both lateral segments of the control mice was likely due to problems with the cardiac triggering. These occurred in 4 out of the 6 measurements and resulted in severe distortions of the first-pass images. LV mass and EDV in TAC mice progressively increased over time and therefore perfusion values were correlated in more detail to LV function and morphology, as shown in Figure 4.8.

Decreased myocardial perfusion in TAC mice was clearly correlated to increased LV EDV and ESV, decreased LVEF and increased myocardial mass (Figure 4.8). Interestingly, even for the TAC mice without a substantial increase in LV mass, rest perfusion was lower as compared to control mice with the same LV mass (arrow in Figure 4.8). Such reduced resting-state perfusion in the absence of LV hypertrophy was also observed in patients with arterial hypertension [37]. We propose that this is the result of a hemodynamic effect caused by the induction of the pressure overload by TAC. Further decrease of the perfusion with increased myocardial mass can be attributed to a decreased capillary density, as hypertrophic myocardial growth outweighs neovascularization [38].

Pathological myocardial hypertrophy is associated with an increased cardiac workload causing an increased O_2 demand, which should be met by increased myocardial perfusion. Instead, myocardial perfusion and perfusion reserve are impaired in pathological cardiac hypertrophy [10]. The resulting lower O_2 delivery capacity has direct functional consequences in terms of impaired myocardial contractility and may even promote apoptosis and fibrosis [7,39]. In our data we indeed observed a significant impairment of LVEF simultaneous with an impaired myocardial perfusion and, importantly, a further decrease of perfusion was strongly associated with a further reduction of the EF (Figure 4.8).

Myocardial stroke work was estimated by multiplying stroke volume and mean aortic pressure. Invasive pressure measurements, for example with a conductance catheter, could not be combined in the same mice with longitudinal MRI measurements. Therefore, mean aortic pressure in control and TAC mice was deduced from earlier observations [21]. The diminished blood flow to TAC hearts resulted in a decreased stroke work. Myocardial efficiency is defined as the ratio of external work performed by the heart to the oxygen consumption [40]. However, no differences between groups could be observed when calculating myocardial efficiency by assuming total blood flow to the heart to be a measure for myocardial oxygen consumption.

In larger mammals perfusion deficits in the hypertrophic heart are often better reflected by impaired perfusion reserve than by resting state perfusion values [10,41]. Here, a part of the perfusion reserve is employed to maintain a near normal or even slightly increased baseline perfusion. In contrast, basal metabolism in healthy mice is relatively high resulting in a concurrent high baseline perfusion in mice (6-8 mL min^{-1} g^{-1}) as compared to larger mammals (0.5-1.5 mL min^{-1} g^{-1}). This may limit recruitment of perfusion reserve to fully compensate for impaired perfusion in face of LV pressure overload, resulting in detection of perfusion abnormalities under resting conditions in mice. Moreover, even though perfusion values were in good agreement with mouse resting state perfusion values previously reported, we cannot exclude that the use of isoflurane as anesthetic might have resulted in some vasodilation and thus in increased resting state myocardial perfusion, potentially enhancing perfusion differences between TAC and control mice [42,43].

Oxygen consumption and therefore myocardial perfusion are closely related to heart rate [44]. For that reason, mouse body temperature and heart rate were carefully kept constant during MRI measurements and between groups. As a result, no relation between heart rate and myocardial perfusion was observed.

Myocardial perfusion measurements were performed in a long-axis orientation to assess possible perfusion differences between basal, midventricular and apical regions [37,45]. However, such differences were not observed in our data. It remains to be determined whether such differences are manifested when the compensated stage of hypertrophy in the present study progresses to overt heart failure.

Patients with an aortic valve stenosis often suffer from myocardial ischemia, but the causative mechanisms are poorly understood. Similarly, the relieve of this ischemic condition upon replacement of the aortic valve is also not well understood [46]. First-pass perfusion measurements in TAC mice before and after removal of the aortic constriction might help to gain new insights in this phenomenon [47,48]. Quantification of transmural perfusion, especially when combined with ventricular pressure measurements, might be of particular interest to assess the potential contribution of impaired endocardial perfusion on this ischemic condition.

There are some limitations to this study. First, in future work our method could be extended to measure the perfusion reserve, for example using adenosine or even a higher dose of isoflurane to produce maximum coronary artery vasodilation [10,49]. This will provide valuable additional information on the maximal perfusion capacity of the heart. Hartley *et al.* studied coronary blood flow velocity using Doppler ultrasound [17]. Coronary flow reserve gradually diminished over time until it was nearly zero three weeks after TAC, mainly as a result of increased baseline coronary flow velocity, also suggesting an impaired myocardial perfusion reserve. In particular, such measurements might be of great value when related to other parameters obtained from a multiparametric MRI protocol. One example is fibrosis, which is known to have detrimental effects on myocardial perfusion [13]. As measurement of the perfusion reserve with the present method requires two dual-bolus injections, the effects of Gd(DTPA)$^{2-}$ accumulation and prolonged anesthesia duration on the repeatability of the perfusion quantification method needs careful consideration. Second, young adult mice were used. Young animals possess the ability to maintain relatively normal capillary density in response to a pressure overload, a capacity that decreases with age [14]. Thus, the use of animals at an early age might lower the relevance for perfusion deficits in heart failure. Nevertheless, the TAC mice in our study did develop perfusion deficits in response to LV pressure overload.

Conclusion

Pressure overload induced cardiac hypertrophy in TAC mice significantly reduced myocardial perfusion as compared to their healthy littermates. Moreover, the perfusion deficit in the hypertrophic mouse heart was proportional to left ventricular volume and mass, and was related to decreased left ventricular ejection fraction. The results from this work show the potential of quantitative first-pass perfusion MRI for the study of the perfusion status of the diseased mouse heart. Moreover, the technique could also provide valuable information for the quantification of pro-angiogenic therapies for the treatment of ischemic heart disease and to monitor the effects of stem cell therapy, in particular when the perfusion tool is incorporated in a multi-parametric MRI protocol.

Acknowledgement

This research was performed within the framework of the Center for Translational Molecular Medicine, project TRIUMPH (grant 01C-103), and supported by the Dutch Heart Foundation. We thank L.B.P. Niesen, D. Veraart and J. Habets for biotechnical assistance and Dr. M.J. van Osch (Leiden University Medical Center) for discussions.

References

1. Denolin, H., et al. *Eur Heart J,* 1983, **4**(7), 445-8.
2. Juenger, J., et al. *Heart,* 2002, **87**(3), 235-41.
3. de Couto, G., et al. *Nat Rev Cardiol,* 2010, **7**(6), 334-44.
4. Lloyd-Jones, D., et al. *Circulation,* 2010, **121**(7), e46-e215.
5. McMurray, J.J., Stewart S. *Heart,* 2000, **83**(5), 596-602.
6. Cokkinos, D.V., Pantos C. *Heart Fail Rev,* 2011, **16**, 1-4.
7. Frey, N., Olson E.N. *Annu Rev Physiol,* 2003, **65**, 45-79.
8. Neubauer, S. *N Engl J Med,* 2007, **356**(11), 1140-51.
9. Shiojima, I., et al. *J Clin Invest,* 2005, **115**(8), 2108-18.
10. Vatner, S.F., Hittinger L. *J Am Coll Cardiol,* 1993, **22**(4 Suppl A), 34A-40A.
11. Mathiassen, O.N., et al. *J Hypertens,* 2007, **25**(5), 1021-6.
12. Levy, B.I., et al. *Circulation,* 2008, **118**(9), 968-76.
13. Dai, Z., et al. *J Cardiol,* 2012, **60**(5), 416-21.
14. Hoenig, M.R., et al. *Curr Vasc Pharmacol,* 2008, **6**(4), 292-300.
15. Cecchi, F., et al. *N Engl J Med,* 2003, **349**(11), 1027-35.
16. Nakajima, H., et al. *Hypertens Res,* 2010, **33**(11), 1144-9.
17. Hartley, C.J., et al. *Ultrasound Med Biol,* 2008, **34**(6), 892-901.
18. Givvimani, S., et al. *J Appl Physiol,* 2011, **110**(4), 1093-100.
19. Givvimani, S., et al. *Arch Physiol Biochem,* 2010, **116**(2), 63-72.
20. Oudit, G.Y., et al. *Cardiovasc Res,* 2008, **78**(3), 505-14.
21. van Deel, E.D., et al. *J Mol Cell Cardiol,* 2011, **50**(6), 1017-25.
22. Streif, J.U.G., et al. *Magn Reson Med,* 2005, **53**(3), 584-92.
23. Jacquier, A., et al. *NMR Biomed,* 2011, **24**(9), 1047-53.
24. Decking, U.K.M., et al. *Am J Physiol Heart Circ Physiol,* 2004, **287**(3), H1132-H40.
25. Coolen, B.F., et al. *Magn Reson Med,* 2010, **64**(6), 1658-63.
26. Makowski, M., et al. *Magn Reson Med,* 2010, **64**(6), 1592-8.
27. van Nierop, B.J., et al. *Magn Reson Med,* 2012, doi: 10.1002/mrm.24424.
28. Rockman, H.A., et al. *Proc Natl Acad Sci U S A,* 1991, **88**(18), 8277-81.
29. van Nierop, B.J., et al. *PLoS ONE,* 2013, **8**(2), e55424.
30. Heijman, E., et al. *NMR Biomed,* 2007, **20**(4), 439-47.
31. Schneider, J.E., et al. *J Cardiovasc Magn Reson,* 2006, **8**(5), 693-701.
32. Köstler, H., et al. *Magn Reson Med,* 2004, **52**(2), 296-9.
33. Jerosch-Herold, M., et al. *Med Phys,* 1998, **25**(1), 73-84.
34. Cerqueira, M.D., et al. *Circulation,* 2002, **105**(4), 539-42.
35. Heijman, E., et al. *J Magn Reson Imaging,* 2008, **27**(1), 86-93.
36. Valentinuzzi, M.E., et al. *Med Biol Eng,* 1969, **7**(3), 277-82.
37. Kawecka-Jaszcz, K., et al. *J Hypertens,* 2008, **26**(8), 1686-94.
38. Izumiya, Y., et al. *Hypertension,* 2006, **47**(5), 887-93.
39. Duncker, D.J., et al. *Med Biol Eng Comput,* 2008, **46**(5), 485-97.
40. Akinboboye, O.O., et al. *Am J Hypertens,* 2004, **17**(5 Pt 1), 433-8.
41. Bache, R.J. *Prog Cardiovasc Dis,* 1988, **30**(6), 403-40.
42. Kober, F., et al. *Magn Reson Mat Phys Biol Med,* 2004, **17**(3-6), 157-61.
43. You, J., et al. *Am J Physiol Heart Circ Physiol,* 2012, **303**(10), H1199-207.
44. Braunwald, E. *Am J Cardiol,* 1971, **27**(4), 416-32.
45. Soler, R., et al. *J Comput Assist Tomogr,* 2006, **30**(3), 412-20.
46. Gould, K.L., Carabello B.A. *Circulation,* 2003, **107**(25), 3121-3.
47. Gao, X.-M., et al. *Am J Physiol Heart Circ Physiol,* 2005, **288**(6), H2702-H7.
48. Stansfield, W.E., et al. *J Surg Res,* 2007, **142**(2), 387-93.
49. Kober, F., et al. *Magn Reson Med,* 2005, **53**(3), 601-6.

5

MR imaging of replacement and diffuse fibrosis in mouse ischemic and non-ischemic heart disease

Bastiaan van Nierop, Noortje Bax, Jules Nelissen,
Abdallah Motaal, Larry de Graaf, Klaas Nicolay,
and Gustav Strijkers

Abstract

Objective: To demonstrate *in vivo* visualization of replacement and diffuse myocardial fibrosis by non-contrast-enhanced magnetic resonance imaging (MRI).

Background: Myocardial fibrosis has an important impact on heart disease progression. Currently, gadolinium-enhanced MRI is commonly used to image fibrosis. We explore the use of a non-contrast-enhanced ultra short echo time (UTE) technique for *in vivo* fibrosis imaging.

Methods: A 3D UTE MRI method to image fibrosis was established. C57BL/6 mice were used with myocardial infarction (MI) (n = 20, ischemic disease), transverse aortic constriction (TAC) (n = 18, non-ischemic disease), or as control (n = 10). UTE images with varying TE were acquired *in vivo* and *ex vivo*. ΔUTE images, resulting from subtraction of short- and long-TE images, were made to highlight fibrotic tissue with short T_2*. *Ex vivo* UTE signal behavior was analyzed using a 3-component model. The presence of replacement and diffuse fibrosis was quantified with histology and correlated to MRI findings.

Results: ΔUTE images showed bright infarct contrast, which co-localized with the fibrotic scar observed on histology. Infarct volumes determined from histology and ΔUTE images linearly correlated ($r = 0.94$, $P < 0.001$). The largest *in vivo* ΔUTE image contrast was observed in the hearts after MI, but significant contrast was also appreciated in the remote tissue of MI hearts and in TAC hearts. Detailed *ex vivo* UTE signal analysis revealed three T_2* contributions that could be attributed to a fast ($T_2^*{}_{\text{fast}}$), a slow ($T_2^*{}_{\text{slow}}$) and a lipid ($T_2^*{}_{\text{lipid}}$) pool. While $T_2^*{}_{\text{fast}}$ remained essentially constant in infarct and TAC hearts, infarct $T_2^*{}_{\text{slow}}$ decreased significantly, while a moderate decrease was observed in remote tissue in post-MI hearts and in the TAC hearts. $T_2^*{}_{\text{slow}}$ correlated with the presence of diffuse fibrosis in the TAC hearts ($r = 0.82$, $P = 0.01$).

Conclusion: Myocardial fibrosis can be visualized *in vivo* with UTE MRI, which opens new opportunities to study the role of fibrosis in cardiovascular disease by *in vivo* imaging.

Introduction

Myocardial fibrosis is the formation of excessive collagen and other extracellular matrix (ECM) components in the interstitium and perivascular regions of the myocardium. This accumulation is a consequence of the disruption of the equilibrium between synthesis and degradation of ECM components [1]. Fibrosis is common to ischemic and non-ischemic heart disease, including myocardial infarction (MI), hypertrophic cardiomyopathy and pressure overload induced hypertrophy [2].

Functional consequences of fibrosis are increased myocardial stiffness, decreased myocardial perfusion and perfusion reserve, and mechano-electrical uncoupling. Together these form a substrate for impaired ventricular relaxation leading to diastolic dysfunction, inappropriate pressure development for systemic perfusion leading to impaired systolic function, ischemia and arrhythmias [1,3-5]. There is increasing awareness for the pivotal role of myocardial fibrosis in the progression of cardiac pathology towards heart failure (HF) and its relation to poor clinical outcome [6,7].

Fibrosis is characterized by different subtypes [2]. Non-ischemic heart disease, for example due to hypertension, is often associated with diffuse, interstitial fibrosis, but also with perivascular fibrosis. Diffuse fibrosis is generally progressive in nature. Ischemic heart disease can result in replacement or scarring fibrosis and often has a localized distribution, for example as a result of cell death after MI.

Clinically, T_1-weighted and T_1-mapping magnetic resonance imaging (MRI) after injection of a Gadolinium (Gd) chelate contrast agent can be used to detect and characterize myocardial fibrosis [2,8]. However, these measurements are based on an increased distribution volume and delayed washout of the contrast agent in fibrotic tissue and therefore do not offer a direct window on fibrotic tissue components. Novel MR imaging techniques that provide a more direct measurement of fibrosis, preferably without the need for a contrast agent, are therefore highly desired. Such techniques could improve risk stratification and aid in the evaluation of new treatment strategies aiming to reduce fibrosis [9-11]. Recently, T_2 was demonstrated to significantly correlate with the extent of diffuse fibrosis in a mouse model of diabetic cardiomyopathy [12]. *Ex vivo* ultra short echo time (UTE) imaging was employed to visualize the collagenous scar, which develops after MI in rats [13].

The UTE imaging technique is very attractive, since it aims to directly visualize tissue components with a very short T_2 such as collagen. However, UTE collagen imaging in the heart was so far only demonstrated for excised hearts and in the presence of replacement fibrosis. The aim of the present study was therefore to develop and demonstrate *in vivo* visualization of replacement as well as diffuse myocardial fibrosis by UTE cardiovascular MRI.

First, a 3D UTE MRI method to image fibrosis in mice was established. Replacement fibrosis was studied in C57BL/6 mice after MI, whereas diffuse fibrosis was studied in mice with pressure overload induced hypertrophy as brought about by transverse aortic constriction (TAC). Findings from UTE MRI in the MI and hypertrophic hearts were related to the amount of fibrosis determined by histology.

Methods

Animal handling

A total of 48 C57BL/6 mice (♂, age 11 weeks, 21-28 grams) were included in this study. Animals were housed under standard laboratory conditions with a 12 h light/dark cycle and were maintained on a standard diet with access to water *ad libitum*. All animal experiments were performed according to the Directive 2010/63/EU of the European Parliament and approved by the Animal Care and Use Committee of Maastricht University.

Animal model

Mice were randomly separated in a control group (n = 8), a group that underwent a permanent occlusion of the left anterior descending (LAD) coronary artery (n = 20) to induce MI and a group that underwent TAC to induce a stenosis of the aorta, resulting in left ventricular (LV) pressure overload (n = 18) [14,15]. Briefly, mice were anesthetized with 2.5 vol% isoflurane in 0.2 L min^{-1} O_2 and 0.2 L min^{-1} medical air and intubated for mechanical ventilation. Animals were placed on a heating pad to maintain body temperature at 37 °C. Buprenorphine (0.1 mg/kg s.c.) was administered for analgesia. Surgical procedures were performed using a stereo microscope (Leica M80). To induce MI the following steps were taken. Mice were placed in a supine position. The left thorax was opened in the fourth intercostal space, the pericardium was opened and the LAD was tied off (6-0 silk suture) just behind its main bifurcation. The success of the procedure was confirmed by discoloration of the myocardium. Finally, the thorax was closed. To induce a stenosis of the aorta in the TAC model a small incision was made just lateral from the sternum above the first intercostal space. The aortic arch was exposed and tied off (6-0 silk suture) together with a 27G (Ø 0.42 mm) needle between the innominate artery and the left common carotid artery. Thereafter, the needle was immediately removed, restoring blood flow. Then, the chest was closed. All surgically prepared animals were allowed to recover at 30 ^{o}C.

UTE sequence design

A 9.4 T small animal MRI scanner (Bruker BioSpec, Ettlingen, Germany) was used, equipped with a 72-mm-diameter quadrature transmit coil and a 4 element phased-array receive coil (Bruker). The 3D UTE sequence consisted of a non slice-selective RF block-pulse ($\alpha = 5^{o}$, 20 µs, bandwidth = 64 kHz) resulting in a minimum echo time (TE) of 21 µs, followed by a 3D radial readout. Other sequence parameters were: pulse repetition time (TR) 6.1 ms, number of signal averages = 1, field of view = 3x3x3 cm^3 and matrix size = 128x128x128. To account for eddy-current induced errors and gradient hardware imperfections, actual k-space trajectories and gradient timing were measured and optimized using a phantom [16].

Study protocol

A subset of the healthy (n = 8), MI (n = 17) and TAC mice (n = 12) were randomly selected for *in vivo* MRI measurements 6 weeks, 1-2 weeks and 11 weeks after the time point of surgery, respectively. After the measurements the anesthetized animals were killed by means of perfusion of the vascular bed with phosphate buffered saline (10 mL, pH 7.4), which was infused via a needle penetrating the apex and exsanguination from the vena cava inferior, as previously described [17]. Next, heart and lungs were excised and promptly weighed, and tibia length (TL) was determined.

Ex vivo UTE measurements were also done in a subset of healthy (n = 6), MI (n = 15) and TAC hearts (n = 13). To this end, hearts were placed in a cryotube filled with Fomblin (Fens Chemicals, The Netherlands) for susceptibility matching.

MRI measurements

Mice were anesthetized with 1.5-2.0 vol% isoflurane in 0.4 L min^{-1} medical air and placed prone in a dedicated animal cradle. The front paws were placed on ECG electrodes and a balloon pressure sensor was placed on the abdomen. Body temperature was maintained at 36-37^{o}C with a heating pad and monitored with a rectal temperature sensor. The readout of the 3D UTE sequence was triggered immediately after ECG R-wave detection. Respiratory gating was applied to prevent motion artefacts. To limit the acquisition time to about 14-16 min (depending on the mouse heart rate), 3 k-lines were measured after every R-wave and the acquisition matrix was 2x undersampled. A blood-saturation slice (1.5 ms Gauss pulse, $\alpha = 90^{o}$, slice thickness 3 mm, followed by a 744 µs crusher gradient) in a short-axis orientation positioned above the LV base provided improved contrast between blood and myocardium. UTE images were obtained with 5 echo times (TE = 21 µs, 100 µs, 300 µs, 714 µs and 1.429 ms). LV function and mass were quantified from two long-axis and a stack of 5-8 short-axis cinematographic (cine) MR images, providing full-heart coverage, with 15-18 frames covering the complete cardiac cycle using an ECG-triggered and respiratory-gated FLASH sequence, as described previously [18,19]. To determine infarct location in the post-MI hearts, a late gadolinium enhancement (LGE) scan was performed at the end of the MRI session using 0.5 mmol/kg $Gd(DTPA)^{2-}$ and a retrospectively gated cine FLASH sequence [20].

Ex vivo MRI measurements were performed on the freshly excised hearts on the same day. No preservative was used to prevent confounding effects on T_2 due to tissue fixation or dehydration [21]. *Ex vivo* fibrosis imaging was performed using the same UTE sequence with 34 different TEs between 21 µs and 4 ms, but without the use of a saturation slice. For anatomical reference, a 3D FLASH image was acquired (TR = 15 ms, TE = 5 ms, $\alpha = 5^{o}$, number of signal averages = 1, field of view = $3x3x3\ cm^3$ and matrix size = 192x192x128).

Histology

A subset of the healthy (n = 3), MI (n = 8) and TAC (n = 6) hearts were embedded in paraffin and cut in 5-µm-thick sections, as described previously [22]. Serial sections (50 µm interval) of the healthy and MI hearts were stained with Picrosirius red and with Prussian blue according to standard histological procedures to confirm the excessive presence of collagen in the infarct area and to exclude confounding effects of iron deposits on the signal formation in the *ex vivo* UTE images, respectively. Serial sections (100 µm interval) covering a one mm mid ventricular portion of the TAC hearts were stained with Picrosirius red to quantify the collagen fractional area in these hearts, defined as the collagen surface area as percentage of the total myocardial surface area. The stained sections were digitalized with a Zeiss Axio Observer Z1 microscope equipped with an AxioCam MRc5 digital camera. Conventional transmission microscopy was used for the healthy and post-MI hearts yielding a total of approximately 38 images per heart. Polarization microscopy was used for quantification of collagen fractional area in the TAC hearts yielding a total of approximately 58 images per heart.

Data analysis

The background signal in the *ex vivo* UTE images was removed using a mask obtained from the 3D FLASH image by applying a signal intensity threshold. Next, long-TE images (4 ms) were subtracted from images with a short-TE (21 µs) to obtain ΔUTE images, suppressing signal with a long T_2* and highlighting myocardial tissue with short T_2* in the infarct area [23]. A signal intensity threshold equal to the mean + 3-times the standard deviation (SD) was applied to a stack of ten remote tissue slices in order to select the hyperintense area in the ΔUTE images.

The selected hyperintense volume, expressed as percentage of the whole heart volume, was determined from the ΔUTE data and was correlated to the collagen rich volume as determined from Picrosirius red stained slices in MI and healthy mice. To this end, a custom-built color detection algorithm based on the hue-saturation-value was used to select the whole heart from the histological images, and to select the collagen rich area (Supplemental Fig. 1).

The *ex vivo* UTE signal behavior was quantified as a function of TE for two reasons: to improve our understanding of the UTE contrast and to determine whether the UTE signal behavior is different in post-MI and TAC hearts as compared to control hearts. To this end, signal intensities were calculated in a stack of ten slices in the healthy hearts, remote tissue of the post-MI hearts, and in the TAC hearts. Here, average SNR (TE = 21 μs) was 23 ± 8. Signal intensities were also calculated in the selected infarct tissue of the post-MI hearts. Signal intensities were normalized to the signal intensity at TE = 21 μs. Next, signal intensity curves *S* were fitted using a Levenberg-Marquardt least squares fitting algorithm to the signal model in equation 1.

$$SI = \left| I_{fast} \cdot e^{-\frac{TE}{T2^*_{fast}}} + I_{slow} \cdot e^{-\frac{TE}{T2^*_{slow}}} + I_{lipid} \cdot e^{-\frac{TE}{T2^*_{lipid}} + i(\omega TE + \varphi)} \right| \qquad [1]$$

This model consists of three exponentially decaying T_2^* components representing a fast relaxing pool, a slowly relaxing pool, and a lipid pool. The lipid pool decays in an oscillatory fashion due to the water-fat chemical shift difference [24]. In this equation I_{fast}, I_{slow}, and I_{lipid} are the relative contributions to the signal of a fast relaxing, a slowly relaxing and a lipid pool, respectively; TE is the echo time; $T_2^*{}_{\text{fast}}$, $T_2^*{}_{\text{slow}}$ and $T_2^*{}_{\text{lipid}}$ the transversal relaxation times of the different pools; ω the water-lipid chemical shift difference, and φ a phase shift. Based on initial model fits the water-lipid chemical shift difference was fixed at $\omega/2\pi$ = 1.3 kHz and $T_2^*{}_{\text{lipid}}$ at 820 μs.

The collagen fractional area in the TAC hearts was determined from the Picrosirius red stained slices using a custom-built color detection algorithm based on the hue-saturation-value (Supplemental Fig. 2). Next, the relationship between $T_2^*{}_{\text{fast}}$ and $T_2^*{}_{\text{slow}}$, and the collagen fractional area of the TAC hearts was assessed.

In vivo long-TE (1.429 ms) UTE images were subtracted from the corresponding images with a short-TE (21 µs) to obtain ΔUTE images to highlight tissue with short T_2*. Next, regions-of-interest (ROIs) were placed in a stack of 6 slices in the different UTE images (all TEs). This was done in the healthy hearts (average number of pixels included: 932 ± 554), in the remote tissue of the post-MI hearts (average number of pixels included: 225 ± 97) and TAC hearts (average number of pixels included: 1637 ± 332). In these images, average SNR (TE = 21 µs) was 12 ± 2. Regions-of-interests were also placed in the infarct tissue (average number of pixels included: 141 ± 68).

All UTE data was analyzed using home-built software in Matlab (The Mathworks, Inc.). For the cine MR images, the myocardial wall was segmented semi-automatically using the software package CAAS MRV FARM (Pie Medical Imaging, The Netherlands) to quantify LV volumes, function and mass [25].

Statistics

Data are expressed as mean ± standard deviation (SD). Differences in LV volume, function and mass between post-MI or TAC mice were compared to control mice using a one-sided unpaired Student's *t*-test. Linearity of the relative Picrosirius red-positive volume as determined with histology with the fractional volume of enhanced pixels on ΔUTE images, and of the relationship between the collagen fractional area and the $T_2{}^*{}_{fast}$ and $T_2{}^*{}_{slow}$ values, were assessed by performing linear regression analysis. Differences in UTE derived parameters between infarct and remote tissue in post-MI hearts were compared using a paired sampled Student's *t*-test, and in remote tissue in post-MI hearts or TAC hearts and control hearts using a one-sided unpaired Student's *t*-test. Calculations were performed using SPSS 19.0 (SPSS Inc., Chicago). For all tests the level of significance was set at $\alpha = 0.05$.

Results

Representative end-diastolic short-axis and long-axis images of healthy, post-MI and TAC hearts are shown in Supplemental Fig. 3. LV end-diastolic volume (EDV) and end-systolic volume (ESV) were increased in post-MI and TAC mice (Supplemental Table 1, $P < 0.001$ in both cases). LV ejection fraction (EF) was increased in both groups ($P < 0.001$), but the cardiac output (CO) was decreased in post-MI mice only ($P < 0.05$). Myocardial hypertrophy was present in post-MI and TAC mice, indicated by increased heart weight/TL and LV mass/TL ($P < 0.001$ in all cases). The heart rate and respiratory rate were stable during the MRI measurements, and not significantly different between experimental groups.

To gain detailed understanding of the signal contributions leading to the contrast in UTE images of the heart, we first studied the UTE signal behavior as function of TE. Representative *ex vivo* signal intensity curves as a function of TE for ROIs in control, post-MI and TAC mouse myocardium are shown in Figure 5.1A-C. *In vivo*, we were only able to measure a few echo times because of measurement time restrictions (Figure 5.1D-F). Also, the longest achievable TE was 1.429 ms, as longer TEs led to motion and field inhomogeneity artifacts. Nevertheless, the *in vivo* curves displayed essentially the same signal decay with TE as the corresponding *ex vivo* curves, with a fast and slow decaying component and a supposedly oscillating contribution. The latter can be attributed to lipid protons for which the chemical shift difference with water protons leads to signal modulation [24]. The three components were consistently observed for the control hearts, the MI hearts and the TAC hearts. In the infarct area, the oscillating lipid signal was less prominent.

For the *ex vivo* case the signal decay as function of TE was fitted well by the 3-component model described by Equation 1 (Figure 5.1). Initial fits to the data resulted in an oscillation frequency of $\omega/2\pi = 1.3 \pm 0.1$ kHz or 3.25 ± 0.25 ppm, which roughly corresponds to the expected water-lipid chemical shift difference. The chemical shift difference was similar for control, post-MI and TAC hearts ($P > 0.05$). Also, no significant difference for $T_2{}^*{}_{\text{lipid}}$ was observed between groups (820 ± 470 µs). In future experiments, a fat saturation preparation sequence may be used to suppress this oscillating contribution, but for the present time we chose to fix ω and $T_2{}^*{}_{\text{lipid}}$ to improve fitting accuracy of the other signal model parameters.

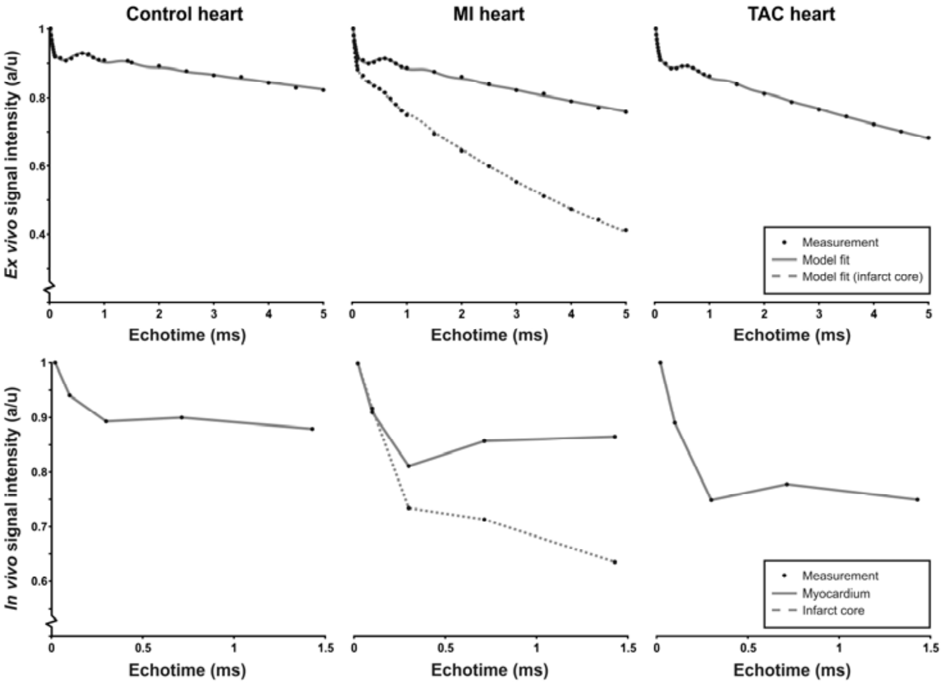

Figure 5.1. Representative ROI-based UTE signal intensity curves as a function of echo time (TE) for *ex vivo* (top row) and *in vivo* (bottom row) measurements in control hearts, remote tissue and infarct area of the post-MI hearts, and the TAC hearts, together with the corresponding model fit (gray line, top row) and lines to guide the reader (bottom row). Signal intensities were normalized to the signal intensity at TE = 21 µs.

The resulting fitted relative signal contributions I_{fast}, I_{slow}, and I_{lipid} were almost equal between post-MI hearts and controls (Table 5.1). For the TAC hearts, I_{slow} was slightly higher ($P < 0.05$) whereas I_{lipid} and I_{fast} were slightly lower as compared to controls ($P < 0.05$). Most prominent differences between the groups were observed in the estimated T_2^*. $T_2^*{}_{slow}$ in the infarct area (5.5 ± 1.4 ms, $P < 0.001$) was significantly lower as compared to the one of remote tissue, and $T_2^*{}_{slow}$ in the remote tissue of post-MI hearts (21 ± 4.3 ms, $P < 0.05$) was significantly smaller than that of control myocardium (30 ± 11 ms). $T_2^*{}_{slow}$ in the TAC hearts (23 ± 4.7 ms, $P = 0.09$) displayed a trend towards lower values as compared to controls. $T_2^*{}_{fast}$ was slightly increased in TAC hearts (38 ± 3.9 µs, $P < 0.05$) as compared to control hearts (34 ± 3.9 µs), and in infarct tissue (58 ± 22 µs, $P < 0.01$) as compared to remote tissue (50 ± 31 µs).

Table 5.1. Three-component model fit parameters of UTE signal intensity as function of TE. Listed parameters are: n = number of mice, fractions of the fast (I_{fast}), slow (I_{slow}) and lipid (I_{lipid}) pool, and the T_2*_{fast} (µs) and T_2*_{slow} (ms) for the control hearts, infarct and remote tissue in post-MI hearts, and the TAC hearts. The changes of T_2*_{slow} in TAC hearts and T_2*_{fast} in remote tissue of post-MI hearts did not reach statistical significance ($P = 0.09$ and $P = 0.10$, respectively).

	Control hearts	**MI**		**TAC**
		Remote	**Infarct core**	
n	6	15		13
I_{fast} (%)	14 ± 1.8	14 ± 2.4	11 ± 5.4	12 ± 1.5*
I_{slow} (%)	84 ± 2.3	83 ± 2.5	87 ± 5.4	86 ± 1.5*
I_{lipid} (%)	2.9 ± 0.9	2.6 ± 1.0	1.7 ± 1.0	2.4 ± 0.7*
T_2*_{fast} (µs)	34 ± 3.9	50 ± 31	58 ± 22†	38 ± 3.9*
T_2*_{slow} (ms)	30 ± 11	21 ± 4.3*	5.5 ± 1.4‡	23 ± 4.7

Indicated are * ($P < 0.05$), † ($P < 0.01$) and ‡ ($P < 0.001$) of the TAC hearts or the remote tissue in post-MI hearts as compared to the healthy hearts, or between the infarct and remote tissue in post-MI hearts.

Having established that the most prominent signal difference between infarct and remote tissue concerns the T_2*_{slow}, we exploited this difference in the transversal relaxation time to obtain contrast on long- and short-TE subtraction images (referred to as ΔUTE images). A representative *ex vivo* ΔUTE image of a chronic post-MI heart with a considerable fibrotic scar in the apical region is shown in Figure 5.2A. The image is shown next to a MI heart 2 days after surgery with substantial wall thinning but without a collagenous scar. A clear hyperenhancement in the ΔUTE image was observed in the apex of the chronic post-MI heart, which colocalized with the area of fibrous scarring observed by histology. The relative infarct volume (% of the whole heart volume) as determined from the ΔUTE images correlated linearly with infarct volume from histology (r = 0.94, $P < 0.001$) (Figure 5.2B).

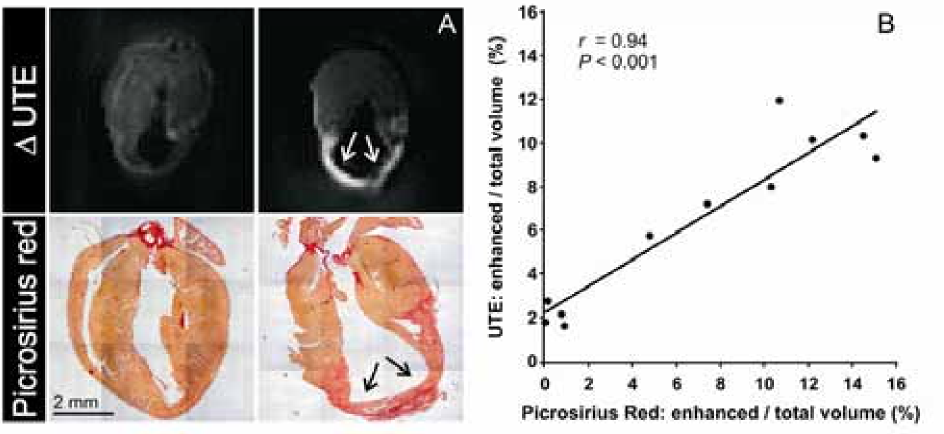

Figure 5.2. Comparison between *ex vivo* ΔUTE images and histology of post-MI hearts. (A) Long-axis cross sections through ΔUTE images in post-MI mouse hearts obtained from subtraction of a short-TE (21 µs) and a long-TE (4 ms) UTE image. The left panels show a post-MI heart 2 days after surgery. The right panels show a post-MI heart with a chronic MI 7 days after surgery. A bright contrast is observed in the ΔUTE image, which corresponds to the location of the chronic MI. Corresponding Picrosirius red stained slices showed hardly any collagen in the MI heart 2 days after surgery, whereas excessive replacement fibrosis was present (↓) in the chronic MI. (B) Correlation between the infarct size as percentage of the total heart volume determined from histology and the *ex vivo* ΔUTE images. The solid line is a linear fit.

Fibrosis in the TAC mouse model is of a diffuse nature and therefore more challenging for imaging than replacement fibrosis in post-MI hearts. Therefore, we investigated whether T_2^* and ΔUTE difference images reported on the presence of diffuse fibrosis in the TAC hearts. Indeed, *ex vivo* analysis (Figure 5.3) revealed a strong and linear correlation of $T_2^*{}_{slow}$ as well as ΔUTE image intensity with the amount of diffuse fibrosis in these hearts ($r = 0.82$, $P = 0.01$ and $r = 0.85$, $P = 0.01$, respectively).

In vivo imaging of replacement and diffuse fibrosis in the mouse models was performed with cardiac triggered versions of the UTE sequence. Basic image quality resulting from UTE imaging was good, as demonstrated in Figure 5.4 for a post-MI mouse heart. Left and right ventricular wall, papillary muscles and infarct area, as well as the surrounding anatomy of ribs and lungs could be clearly distinguished. The dark bands resulted from the saturation slice to suppress blood signal in the LV lumen.

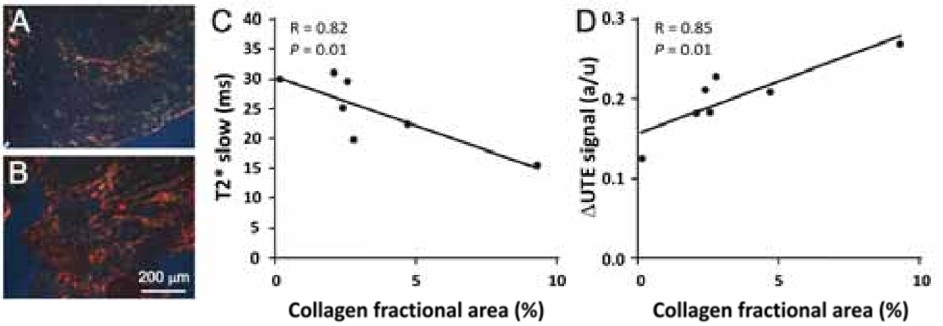

Figure 5.3. Comparison between *ex vivo* ΔUTE images and histology in TAC hearts. Representative Picrosirius red stained slice of a TAC heart with (A) low amounts and (B) of a heart with high amounts of collagen present. Correlations between (C) T_2*_{slow} and (D) ΔUTE contrast versus the collagen fractional area. The solid lines are linear fits.

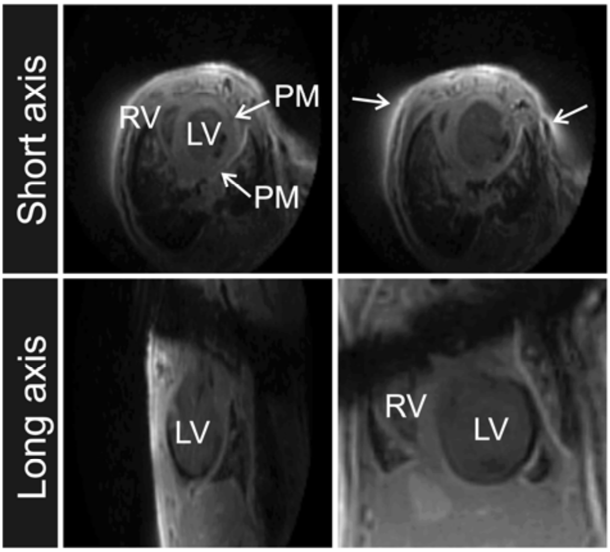

Figure 5.4. *In vivo* long-axis and short-axis cross-sections through a 3D UTE image. Two short-axis and long-axis cross-sections through an *in vivo* UTE dataset (TE = 21 μs) of a post-MI mouse heart. Indicated are the right ventricle (RV), left ventricle (LV), the papillary muscles (PM) and some small artefacts (↖). A dark saturation band with low signal intensity is visible in the two long-axis images.

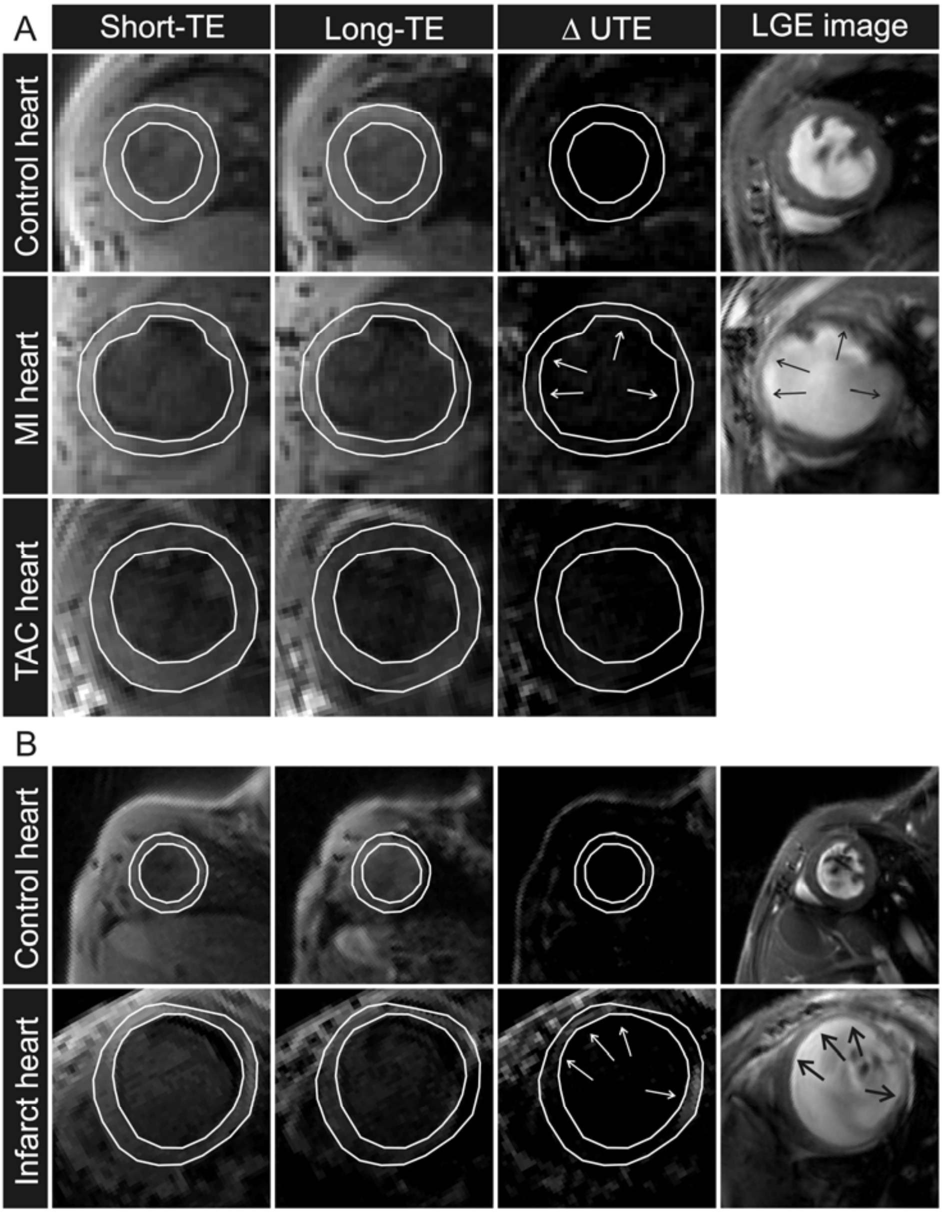

Figure 5.5. *In vivo* UTE in control, post-MI and TAC mice (A). Examples of a short-axis cross-section of a healthy heart (top row), a MI heart (middle row) and a TAC heart (bottom row) obtained with the 3D UTE sequence (short-TE, long-TE and ΔUTE image). Late gadolinium enhancement (LGE) scans were obtained in control and post-MI mice (right column). *In vivo* UTE images in a control and post-MI mouse obtained with a long-TE of 4 ms. Here, a more pronounced enhancement is observed in the infarct area in the ΔUTE images as compared to those obtained with a long-TE of 1.429 ms (B).

Examples of *in vivo* short-TE (21 µs) and long-TE (1.429 ms) UTE images of a healthy heart, a post-MI heart and a TAC heart are presented in Figure 5.5. ΔUTE images of the post-MI hearts revealed areas with hyperenhancement, which colocalized with the MI as independently determined by LGE. In the TAC hearts no focal hyperenhancement could be distinguished visually. ROI-based ΔUTE signal differences of control, post-MI and TAC mice were quantified (Figure 5.6). ΔUTE signal in the MI (0.26 ± 0.10, $P < 0.05$) was significantly higher as that in remote tissue (0.20 ± 0.06). Moreover, the ΔUTE signal in the remote tissue of the post-MI hearts (0.20 ± 0.06, $P < 0.001$) and TAC hearts (0.21 ± 0.07, $P < 0.001$) was larger as compared to that observed in the control hearts (0.13 ± 0.04). We attribute the latter signal difference to the presence of diffuse fibrosis in these hearts, in line with the *ex vivo* results of Figure 5.3.

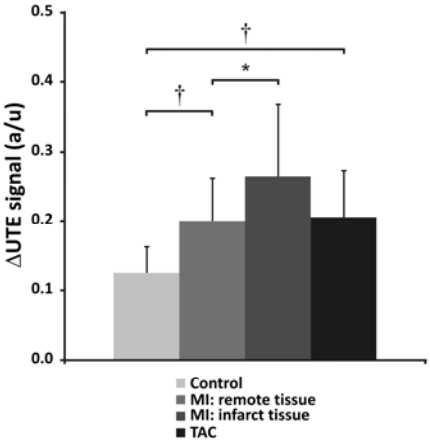

Figure 5.6. *In vivo* signal difference in control, post-MI and TAC mice. ΔUTE signal decrease between the short-TE (21 µs) and long-TE images (1.429 ms) in control hearts, remote and infarct tissue in post-MI hearts, and TAC hearts. Statistical differences are indicated by * ($P < 0.05$) and † ($P < 0.01$). Error bars indicate SD.

Discussion

Myocardial fibrosis has an important impact on heart disease progression and is related to poor outcome [6,26]. Replacement and diffuse fibrosis may be visualized using a Gd-chelate contrast agent and T_1-weighted imaging or quantitative T1-mapping [27,28]. However, Gd-based fibrosis imaging has certain drawbacks since it relies on nonspecific wash in and wash out kinetics of the agent in the fibrotic myocardium, leading to issues with timing of imaging and confounding factors associated with myocardial disease such as the presence of edema. Alternative imaging techniques for the detection of replacement and more importantly diffuse fibrosis are therefore highly desired. In this study we have explored the usefulness of a UTE technique and multi-pool T_2* mapping to image replacement fibrosis as well as diffuse fibrosis by virtue of changes in the transverse relaxation time induced by the presence of collagen as well as other fibrotic elements in the ECM.

Detailed measurements with varying TE were performed in excised hearts, to improve the understanding of the signal generation by UTE imaging and to investigate whether signal behavior is different in case of replacement or diffuse fibrosis. Typically, transverse relaxation processes in muscle tissue are best described by a multi-component signal model depending on the range of TEs used [29]. Indeed, UTE signal curves were adequately described by two exponentially decreasing and one oscillating decaying lipid component. The relative contributions of the different model components (I_{fast}, I_{slow}, and I_{lipid}) were essentially the same in control, post-MI and TAC hearts, apart from a small decrease of I_{fast} and I_{lipid} and a small increase of I_{slow} in the TAC hearts as compared to controls (Table 5.1). This is a surprising finding, since there are rather large differences in the amounts of collagen and other extracellular matrix components in the myocardium for the different disease models, particularly for the MI tissue in comparison to remote and control tissue. We propose two potential reasons for this finding. First, we have normalized the signal to the shortest achievable TE (21 µs), which may not be sufficiently short to capture all of the signal from collagen-bound water. Possible differences in signal behavior at even shorter TE may therefore have gone undetected. Second, different T_2^* contributions are not separated in spatial terms, since most of the MRI signal in the myocardium originates from free water that undergoes rapid exchange between the extracellular and intracellular tissue compartments. In this respect, it is not unlikely that changes in the relaxation behavior mediated by changes in collagen content were detected in the water pool with the highest signal contribution and the longer transverse relaxation time. The significant correlation between the collagen fractional area and the $T_2^*{}_{slow}$ as determined in *ex vivo* TAC hearts supports this explanation.

Previously, strong correlations were reported between the amount of diffuse fibrosis and the T_2 relaxation time in small animal models of diabetic cardiomyopathy [12,30]. Our findings are also in quantitative agreement with recent measurements by Aguor *et al.* who found a significant decrease in T_2^* in MI tissue using a multi-gradient-echo sequence [31].

Hyperenhancement in ΔUTE images colocalized with collagen rich areas in MI tissue observed in stained sections, and the hyperintense volume from MRI and enhanced volume from histology strongly correlated. Iron can be ruled out as a significant source of the contrast as hardly any iron was detected in Prussian blue stained histological slices of the MI tissue (Supplemental Fig. 4) [32]. These findings are in agreement with the *ex vivo* results of de Jong *et al.* who also reported a clear correlation between relative enhanced volume from UTE MRI and MI size from histology for a rat model of

MI [13]. Importantly, we showed that the hyperenhancement in ΔUTE images of MI tissue was also detected *in vivo*.

ΔUTE images resulted in significant signal intensity differences between healthy myocardium on the one hand and tissue with replacement and diffuse fibrosis on the other hand (Figure 5.6), demonstrating that the current UTE protocol can be used to assess the presence of fibrosis in these mouse models of myocardial disease. Nevertheless, it would be preferable to perform T_2* mapping *in vivo* as well, since this would facilitate quantitative comparisons between studies or in longitudinal studies and would strongly reduce the sensitivity to sequences parameters, coil sensitivity profiles, and cardiac and respiratory rates. Currently, the acquisition time of the 3D UTE protocol is too long to enable *in vivo* T_2* mapping, for which we intend to explore the use of acquisition acceleration techniques such as parallel imaging or compressed sensing to decrease imaging time [33].

Complementary techniques for fibrosis imaging include the use of collagen-targeted MRI contrast agents [34]. Also, fibrosis-induced changes in tissue stiffness may be quantified using cardiac MR elastography [35] or by detailed evaluation of the LV diastolic function [26,28]. Alternatively, ultrasonic reflectivity was shown to relate to the amount of connective tissue in human myocardium [36].

Complications in the present experimental design include age differences between the MI and TAC mice. However, changes in the ECM due to ageing are known to be much smaller than fibrosis brought about by MI or TAC [37]. Moreover, the ΔUTE technique is a simple approach to suppress signal from healthy myocardium, but it is sensitive to misregistration caused by cardiac motion [38]. The use of a UTE protocol with a long-T_2 suppression preparation sequence could solve this registration issue [23]. Furthermore, differences in blood oxygenation, relative blood volume and edema are known to modulate the tissue T_2* properties and could thus affect ΔUTE contrast [39-41]. We can exclude significant effects of edema, since this mainly occurs in the acute phase after cardiac ischemia and would lead to longer transversal relaxation times in the MI tissue [42,43]. The blood oxygenation level might influence the myocardial transverse relaxation time as well [44,45]. We cannot fully exclude such a contribution to the observed contrast, because we have no information on the oxygenation of the mouse blood. However, the strong contrast in the MI tissue, where little blood is present, and the strong correlation between T_2* and the amount of interstitial collagen strongly suggest that fibrosis is the main source of contrast.

Conclusion

In vivo visualization of replacement and diffuse fibrosis in the mouse heart is possible using UTE cardiovascular MRI. The amount of diffuse fibrosis in pressure overload induced hypertrophy correlated to the slow T_2* in the mouse myocardium. Clinically, the technique may aid in improved risk stratification for heart disease patients and in the evaluation of new treatment strategies aiming to reduce fibrosis.

Acknowledgements

This research was performed within the framework of the Center for Translational Molecular Medicine, project TRIUMPH (grant 01C-103), and supported by the Dutch Heart Foundation. N.A.M. Bax was supported by a grant from the Dutch government to the Netherlands Institute for Regenerative Medicine (NIRM, grant No. FES0908). We thank L.B.P. Niesen and D. Veraart for biotechnical assistance, and Prof. P. Luijten, S. de Jong, J. Zwanenburg (University Medical Center Utrecht) and W. de Graaf (Eindhoven University of Technology) for discussions.

Supplemental information

Supplemental Table 1

General animal characteristics and global LV cardiac parameters determined from cine MRI of the cohort of control mice, post-MI mice and TAC mice.

	Control	**MI**	**TAC**
n	10	18	12
HW (mg)	156±17	181±29*	252±72‡
HW/TL (mg/mm)	8.7±0.6	10.1±1.6*	13.9±4.0‡
LV mass (mg)	85±9	109±22‡	135±33‡
LV mass/TL (mg/mm)	4.7±0.5	6.3±1.1‡	7.6±2.0‡
LuW (mg)	179±35	157±23	213±75
LuW/TL (mg/mm)	10.4±2.1	8.8±1.2	11.7±4.2
HR (min^{-1})	509±33	519±42	518±46
Resp (min^{-1})	81±12	79±10	83±9
EF (%)	61±7	33±14‡	42±18‡
EDV (µL)	68±11	125±47‡	108±38‡
ESV (µL)	27±7	89±48‡	68±42‡
SV (µL)	41±7	36±10	40±10
CO (mL min^{-1})	22±3	19±6*	21±5

Listed parameters are: n = number of mice, HW = heart weight, HW/TL = heart weight normalized to tibia length, LV mass = left ventricular myocardial mass as determined using MRI, LV mass/TL is LV mass normalized to tibia length, LuW = lung weight, LuW/TL = lung weight normalized to tibia length, HR = heart rate, Resp = respiratory rate, EF = ejection fraction, EDV = end-diastolic volume, ESV = end-systolic volume, SV = stroke volume, CO = cardiac output. Statistical differences are indicated by * ($P < 0.05$) and ‡ ($P < 0.001$).

Supplemental Figure 1: Infarct size quantification from histology

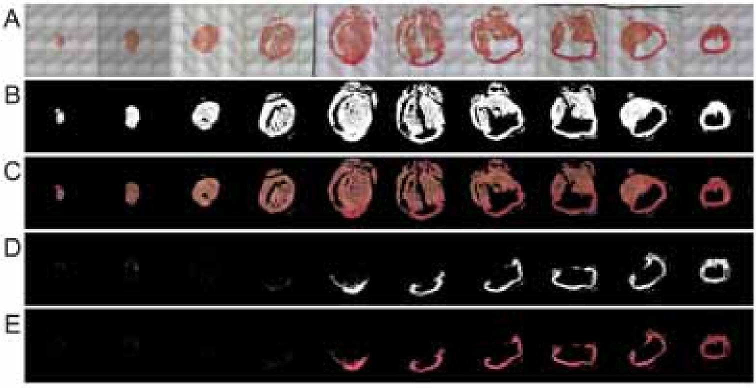

(A) Representative stack of ten Picrosirius red stained slices of a post-MI heart. A custum-built color detection algorithm was used to define (B) a whole heart mask to remove the background from (C) the histological images. To this end, the original RGB images (red-green-blue) were converted to HSV images (hue-saturation-value) and signal intensity thresholds were applied to the different HSV channels. (D) Next, a mask was defined to select (E) the collagen rich area, using a signal intensity threshold on the hue channel. The HSV thresholds were determined empirically and proper selection of the heart and collagen rich area were confirmed by visual inspection.

Supplemental Figure 2: Collagen fractional area determined from histology

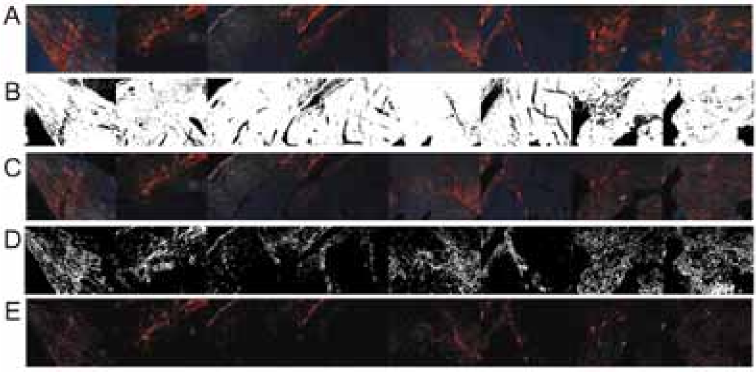

Representative stack of ten Picrosirius red stained slices of a TAC heart (A). A custom-built color detection algorithm was used to define a mask (B) removing the background from the histological images (C). To this end, the original RGB images (red-green-blue) were converted to HSV images (hue-saturation-value) and signal intensity thresholds were applied to the different HSV channels. Next, a mask (D) was defined to select the collagen (E). The HSV thresholds were determined empirically and proper selection of the heart and collagen rich area were confirmed by visual inspection.

Supplemental Figure 3: Cinematographic MRI

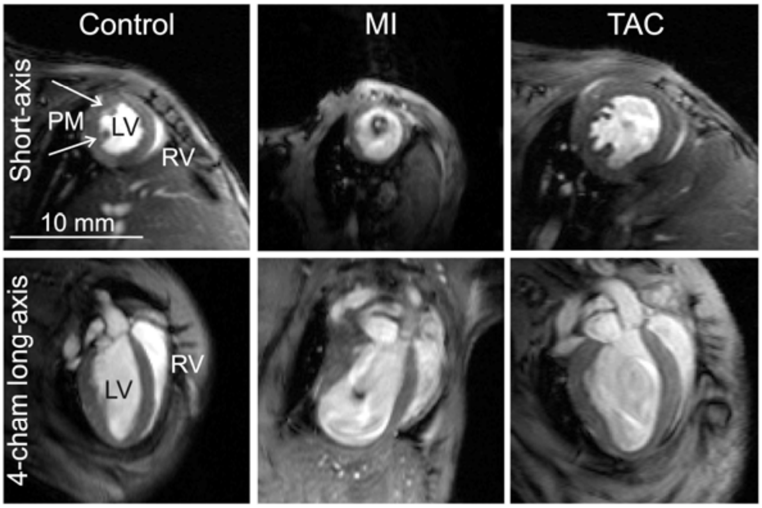

Representative end-diastolic short-axis and long-axis images from a control heart, a post-MI heart and a TAC heart.

Supplemental Figure 4: Prussian blue staining

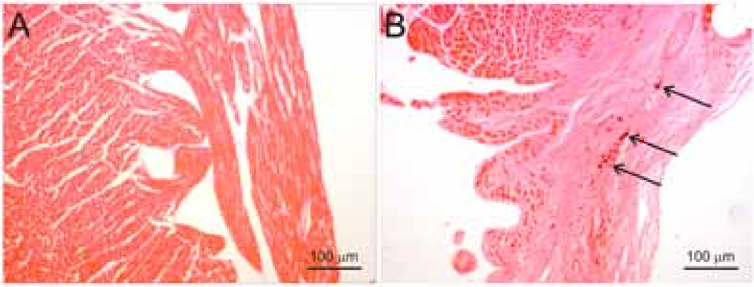

Representative Prussian blue stained slices of (A) a control and (B) an the infarct area of a post-MI heart. Hardly any iron deposits were present in the healthy hearts and only very small amounts were found in the infarct area (↖).

References

1. Díez, J., et al. Nat Clin Pract Cardiovasc Med, 2005, 2(4), 209-16.
2. Mewton, N., et al. J Am Coll Cardiol, 2011, 57(8), 891-903.
3. Kass, D.A., et al. Circ Res, 2004, 94(12), 1533-42.
4. Burlew, B.S., Weber K.T. Herz, 2002, 27(2), 92-8.
5. Brower, G.L., et al. Eur J Cardiothorac Surg, 2006, 30(4), 604-10.
6. Creemers, E.E., Pinto Y.M. Cardiovasc Res, 2011, 89(2), 265-72.
7. Milano, A.D., et al. J Thorac Cardiovasc Surg, 2012, 144(4), 830-7.
8. Jackson, E., et al. Clin Radiol, 2007, 62(5), 395-403.
9. Karamitsos, T.D., et al. J Am Coll Cardiol, 2009, 54(15), 1407-24.
10. Jellis, C., et al. J Am Coll Cardiol, 2010, 56(2), 89-97.
11. Sado, D.M., et al. Future Cardiol, 2011, 7(5), 643-50.
12. Bun, S.-S., et al. Invest Radiol, 2012, 47(5), 319-23.
13. de Jong, S., et al. J Mol Cell Cardiol, 2011, 51(6), 974-9.
14. Lutgens, E., et al. Cardiovasc Res, 1999, 41(3), 586-93.
15. Rockman, H.A., et al. Proc Natl Acad Sci U S A, 1991, 88(18), 8277-81.
16. Duyn, J.H., et al. J Magn Reson, 1998, 132(1), 150-3.
17. Strijkers, G.J., et al. NMR Biomed, 2009, 22(2), 182-90.
18. Heijman, E., et al. NMR Biomed, 2007, 20(4), 439-47.
19. Schneider, J.E., et al. J Cardiovasc Magn Reson, 2006, 8(5), 693-701.
20. Coolen, B.F., et al. Magn Reson Med, 2010, 64(6), 1658-63.
21. Thickman, D.I., et al. Radiology, 1983, 148(1), 183-5.
22. Winter, E.M., et al. Circulation, 2007, 116(8), 917-27.
23. Gatehouse, P.D., Bydder G.M. Clin Radiol, 2003, 58(1), 1-19.
24. O'Regan, D.P., et al. Eur Radiol, 2008, 18(4), 800-5.
25. Heijman, E., et al. J Magn Reson Imaging, 2008, 27(1), 86-93.
26. Moreo, A., et al. Circ Cardiovasc Imaging, 2009, 2(6), 437-43.
27. Iles, L., et al. J Am Coll Cardiol, 2008, 52(19), 1574-80.
28. Ellims, A.H., et al. J Cardiovasc Magn Reson, 2012, 14(1), 76.
29. Brix, G., et al. Phys Med Biol, 1990, 35(1), 53-66.
30. Loganathan, R., et al. Int J Cardiovasc Imaging, 2006, 22(1), 81-90.
31. Aguor, E.N.E., et al. Magn Reson Mat Phys Biol Med, 2012, 25(5), 369-79.
32. Rozenman, Y., et al. Radiology, 1990, 175(3), 655-9.
33. Griswold, M.A., et al. Magn Reson Med, 2002, 47(6), 1202-10.
34. Caravan, P., et al. Angew Chem Int Ed Engl, 2007, 46(43), 8171-3.
35. Robert, B., et al. Magn Reson Med, 2009, 62(5), 1155-63.
36. Picano, E., et al. Circulation, 1990, 81(1), 58-64.
37. Debessa, C.R.G., et al. Mech Ageing Dev, 2001, 122(10), 1049-58.
38. Du, J., et al. Magn Reson Imaging, 2011, 29(4), 470-82.
39. Beyers, R.J., et al. Magn Reson Med, 2012, 67(1), 201-9.
40. Tilak, G.S., et al. Invest Radiol, 2008, 43(1), 7-15.
41. Eitel, I., Friedrich M.G. J Cardiovasc Magn Reson, 2011, 13, 13.
42. Yamada, K., et al. Eur Radiol, 2012, 22(4), 789-95.
43. Abdel-Aty, H., et al. J Am Coll Cardiol, 2009, 53(14), 1194-201.
44. Ghugre, N.R., et al. J Magn Reson Imaging, 2006, 23(1), 9-16.
45. Atalay, M.K., et al. Magn Reson Med, 1995, 34(4), 623-7.

6

In vivo cardiac ^{31}P MR spectroscopy in a mouse model of heart failure using 3D ISIS

Adrianus Bakermans, Bastiaan van Nierop*, Desiree
Abdurrachim*, Inge van der Kroon, Gustav Strijkers,
Sander Houten, Klaas Nicolay, and Jeanine Prompers

* These authors contributed equally to this work

Abstract

Background: Phosphorous-31 magnetic resonance spectroscopy (^{31}P-MRS) can provide a noninvasive window on the cardiac energy status. Mouse models of human cardiac disease are widely used in preclinical studies, but application of ^{31}P-MRS in the *in vivo* mouse heart has been limited. The small-sized, fast-beating mouse heart imposes challenges regarding localized signal acquisition devoid of contamination from signal originating from surrounding tissues. Here, we report the implementation of 3D Image Selected *In vivo* Spectroscopy (ISIS) for single-voxel localized ^{31}P-MRS of the *in vivo* mouse heart at 9.4 T.

Methods: A cardiac-triggered, respiratory-gated 3D ISIS sequence was used, whilst maintaining steady state of magnetization with dummy excitations during respiratory gates to ensure a constant repetition time. Cardiac ^{31}P MR spectra were acquired *in vivo* in healthy mice and in mice with a transverse aorta constriction (TAC), a model of heart failure. MR imaging was used to quantify cardiac function and morphology.

Results: Signals from phosphocreatine (PCr) and adenosine triphosphate (ATP) could be quantified in the spectra obtained from the *in vivo* mouse hearts. The PCr-to-ATP ratio, an index of myocardial energy status, was ~25% lower in TAC mice compared to control mice ($P < 0.01$), and was accompanied by an increased left ventricular mass and a decreased ejection fraction.

Conclusion: The 3D ISIS localized ^{31}P-MRS method is able to noninvasively detect disturbed cardiac energy homeostasis, while allowing for measurements of cardiac function with MRI during the same experimental session.

Introduction

Currently, cardiovascular disease is the leading cause of death worldwide. Research efforts are ample in trying to understand the pathogenesis of cardiomyopathies that contribute to mortality, e.g., in diabetes, ischemia, high blood pressure, aortic stenosis, and congenital diseases. Mouse models of disease are widely used in preclinical studies. In recent years, many magnetic resonance imaging (MRI) and, to a lesser extent, spectroscopy (MRS) methods have been introduced to study the *in vivo* mouse heart in a noninvasive fashion [1,2]. Application of these methods allows for longitudinal studies of disease progression and an assessment of the effects of therapeutic strategies.

Disturbed myocardial energy metabolism has been identified as an important contributor to the development of cardiomyopathy [3]. Assessment of the myocardial energy status is therefore instrumental in characterizing disease progression or treatment response. The high-energy phosphates phosphocreatine (PCr) and adenosine triphosphate (ATP) provide energy for cellular processes such as sarcomere contraction in cardiomyocytes, and are essential for energy transport. The inherent instability of high-energy phosphates compromises accurate assessment of the myocardial energy status using traditional biochemical techniques, which in addition require disruptive or terminal biopsies, precluding longitudinal *in vivo* investigations of the same subject.

Currently, phosphorous-31 MRS (^{31}P-MRS) is the only method that provides a noninvasive window on tissue energy metabolism [3]. Localized signal acquisition is essential to restrict the obtained spectrum to the heart, excluding signal from nearby liver tissue or chest skeletal muscle. Localization methods for cardiac ^{31}P-MRS include single-voxel as well as chemical shift imaging (CSI) approaches. ^{31}P-CSI allows for a regional assessment of myocardial energy status, but is susceptible to intervoxel signal contamination due to Fourier bleeding [4,5]. In contrast, single-voxel localization with 3D Image Selected *In vivo* Spectroscopy (ISIS) leads to a better defined voxel shape, but voxel size is usually much larger compared to CSI, commonly encompassing the entire left ventricle (LV) [6-8]. Nowadays, both CSI and ISIS approaches are applied for human cardiac ^{31}P-MRS [9]. The rodent heart has been studied with ^{31}P-MRS *in situ* using open thorax protocols as well as *ex vivo* in perfused-heart setups [10-13]. Literature reports of noninvasive *in vivo* cardiac ^{31}P-MRS in the mouse are limited, referring to only a few laboratories worldwide [8,14,15]. Application of ^{31}P-MRS to the *in vivo* mouse heart is very challenging due the small organ size (100-200 mg), the high heart rate (500-600 min^{-1}), and the intrinsically low sensitivity of ^{31}P-MRS (6.65% of the proton (^{1}H) sensitivity), possibly explaining the limited application of this technique.

Methods for *in vivo* 1D and 2D ^{31}P-CSI of the mouse heart were initially demonstrated in healthy mice and in a transgenic mouse model for cardiomyopathy [14,15]. These experiments were performed at a constant repetition time (TR), which is essential for an accurate quantification of the signals, but none of these methods used cardiac triggering or respiratory gating to account for motion of the tissue of interest. Together with the effects of Fourier bleeding in CSI methods, neglecting tissue displacement may lead to significant contamination of the spectrum with signal from the liver, blood, and/or chest muscle. One early study describes the application of cardiac-triggered 3D ISIS for *in vivo* ^{31}P-MRS of the mouse heart, which until now has not been pursued by other research groups [8]. These initial experiments were performed at 2.35 T and required a scan time of almost 3 hours, which is not desirable in studies combining multiple MR modalities, i.e., ^{31}P-MRS, ^{1}H-MRS and MRI. At higher field strengths, experimental time can possibly be reduced to acceptable values. While cardiac triggering was used for synchronizing the acquisitions with the cardiac cycle, no measures were taken to ensure a constant TR. When applying ISIS under partially saturated conditions (i.e., $TR < 5 \times T_1$), variations in TR can lead to severe signal contamination [16,17].

Here, we report the implementation of 3D ISIS for single-voxel localized ^{31}P-MRS of the *in vivo* mouse heart at 9.4 T. Since 3D ISIS is a multi-shot localization method and hence sensitive to motion artifacts, we employed both cardiac triggering and respiratory gating whilst maintaining steady state of magnetization with dummy excitations during respiratory gates to ensure a constant TR. To demonstrate suitability for cardiac applications, the method was applied to a well-characterized mouse model of heart failure (HF). In these mice, a transverse aorta constriction (TAC) was placed to surgically induce pressure-overload hypertrophic cardiomyopathy, a condition previously shown to be associated with an impaired myocardial energy status [18]. Cardiac functional parameters were quantified using MR images obtained during the same experimental session, which could typically be completed within 2 hours.

Methods

Animals

C57BL/6 mice (♂, age 11 weeks, n = 8, body weight = 26.2 ± 2.6 g) underwent TAC surgery as described previously [19,20]. In brief, mice were anesthetized with 2.5 vol% isoflurane in 0.2 L min^{-1} O_2 and 0.2 L min^{-1} medical air, after which mice were intubated for mechanical ventilation. Buprenorphine (0.1 mg/kg s.c.) was administered for analgesia. A small incision was made just lateral from the sternum above the first intercostal space to gain access to the aortic arch. The aorta was tied off together with a 27G needle between the innominate artery and the left common carotid artery with a 6-0 silk suture. The needle was immediately removed, leaving a stenosis of the aorta that results in LV pressure overload. The chest was closed and the intubation tube was removed to allow full recovery. Seven weeks after surgery, MR data were acquired as described below. Healthy mice (n = 9, body weight = 24.4 ± 2.0 g) served as controls. Immediately after the MR measurements, anesthetized mice were sacrificed by exsanguination from the vena cava inferior. Blood was collected in EDTA tubes for further analysis with *ex vivo* ^{31}P-MRS. The heart was rapidly excised and weighed to confirm hypertrophic growth of the myocardium in TAC mice. All animal experiments were performed according to the Directive 2010/63/EU of the European Parliament and approved by the Animal Care and Use Committee of Maastricht University.

MR protocol

Mice were anesthetized with 4.0 vol% isoflurane in 0.4 L min^{-1} flow of medical air and positioned prone in a purpose-built support cradle. Anesthesia was maintained by providing 1.5-2.0 vol% isoflurane in a continuous flow of 0.4 L min medical air through a nose cone. The mouse was positioned with the heart above a custom-built, actively decoupled, two-turn ^{31}P surface coil (Ø 15 mm) for signal reception. The front paws were taped onto gold-coated ECG electrodes integrated in the anesthesia mask. A respiratory balloon was positioned under the lower abdomen. Vital signs were monitored and used for MR gating and triggering by the SA Monitoring and Gating System 1025 (Small Animal Instruments, Stony Brook, NY, USA). Mouse body temperature was maintained using a heating pad with integrated warm water flow. Temperature was monitored with an external abdominal fiber optic temperature probe. The setup was entered into a horizontal-bore 9.4 T magnet (Magnex Scientific, Oxon, UK), interfaced to a Bruker Avance III console (Bruker Biospin MRI, Ettlingen, Germany) and controlled by the ParaVision 5.0 software package (Bruker Biospin). The system was equipped with a 740 mT/m gradient set, and a volume coil (Ø 54 mm) composed of a quadrature ^{1}H birdcage resonator and a linear ^{31}P birdcage resonator

(RAPID Biomedical GmbH, Rimpar, Germany), used for ^{1}H imaging and shimming, and for radiofrequency (RF) transmission for ^{31}P-MRS, respectively.

Scout ^{1}H images were acquired to confirm positioning of the heart within the sensitive area of the surface coil. A segmented, prospectively cardiac-triggered, respiratory-gated FLASH sequence was used to acquire cine ^{1}H MR image series of 16-18 frames per cardiac cycle. Four 1-mm LV short-axis slices were complemented with four- and two-chamber long-axis views, and used for quantification of LV function and morphology as well as for anatomical reference during 3D ISIS voxel planning for localized ^{31}P-MRS. Imaging parameters were: pulse repetition time (TR) = 7 ms, echo time (TE) = 1.8 ms, number of signal averages (NA) = 4, $\alpha = 15°$, field of view = 3×3 cm^{2}, matrix = 128×128. Total acquisition time was approximately 30 minutes.

Subsequently, an 11×11×11 mm^{3} cubic voxel in the sensitive area of the surface coil was shimmed manually by minimizing the $^{1}H_2O$ line width acquired with a cardiac-triggered, respiratory-gated PRESS sequence [21]. Next, calibration of the ^{31}P sinc excitation pulse (pulse length = 1.2 ms, bandwidth = 32.0 ppm) was performed by varying pulse power to achieve maximal signal from a spherical phantom (Ø 5 mm) containing 15 M phosphoric acid, positioned underneath the ^{31}P surface coil. After removal of the phantom, unlocalized ^{31}P-MR spectra were acquired in a subset of animals (n = 5 per group) to assess metabolite T_1 values using conventional saturation recovery experiments. Parameters were: 1.2 ms sinc excitation pulse, bandwidth = 32.0 ppm, γ-ATP on resonance, TR = 500 ms, 1000 ms, 2000 ms, 4000 ms, 6000 ms, and 15000 ms, NA = 1024 - 32.

Next, a cardiac-triggered, respiratory-gated ISIS sequence was used for localized cardiac ^{31}P-MRS. Dependent on heart size, a 125 - 216 µL cubic voxel was positioned to enclose the end-diastolic LV, carefully excluding the liver and skeletal muscle (Figure 6.1A-B). ISIS parameters were: TR ≈ 2 seconds, 96 ISIS cycles (768 scans) preceded by 1 dummy cycle, 6.25 ms 180° adiabatic hyperbolic secant inversion pulses (bandwidth = 37.5 ppm), 1.2 ms 90° sinc excitation pulse (bandwidth = 32.0 ppm), γ-ATP on resonance. Triggering was timed at ECG R-wave upslope detection. Respiratory gating causes fluctuations in effective TR, leading to variations in longitudinal magnetization between subsequent acquisitions. If longitudinal magnetization is not equal for all eight acquisitions within one 3D ISIS cycle, cancellation of unwanted signals in the addition/subtraction scheme is incomplete. Thus, when measuring at $TR < 5 \times T_1$, a constant TR is required to minimize signal contamination. Therefore, we performed unlocalized dummy excitation pulses during respiratory gates to maintain an essentially constant TR of ≈ 2 seconds. Acquisition time was approximately 45 minutes.

In a subset of healthy mice (n = 6), fully relaxed 3D ISIS was performed (TR ≈ 15 seconds, 24 cycles/192 scans, acquisition time ≈ 1 hour and 30 minutes). These measurements were used to verify the partial saturation correction factor obtained with the unlocalized saturation recovery experiments.

To investigate the contribution of blood metabolites to the cardiac ^{31}P MR spectra acquired *in vivo*, spectra of fresh blood were measured *ex vivo* using a pulse-acquire sequence. A vial with approximately 1 mL of blood in EDTA was positioned just over the surface coil and maintained at 37 °C by a warm water flow through a heating pad. Parameters were: 1.2 ms 90° sinc excitation pulse, γ-ATP on resonance, TR = 2000 ms, NA = 512.

Image analysis

LV cavity and myocardial wall volumes were quantified by semi-automatic segmentation of the cine images using CAAS MRV FARM (Pie Medical Imaging, The Netherlands) as described previously, yielding LV end-diastolic volume (EDV), end-systolic volume (ESV), stroke volume (SV), ejection fraction (EF), and LV myocardial mass [22].

^{31}P-MRS data analysis

Fitting of the metabolite signals to Lorentzian line shapes was performed in the time domain using AMARES in jMRUI [23]. The PCr resonance at 0.00 ppm was used as an internal chemical shift reference. The ATP resonances at -2.48 ppm (γ; doublet), -7.52 ppm (α; doublet) and -16.26 (β; triplet) were fitted with equal amplitudes and line widths within each multiplet, and a J-coupling constant of 17 Hz. The γ-ATP line widths ($LW_{\gamma\text{-ATP}}$) were constrained relative to the PCr line width (LW_{PCr}) according to an empirically determined relation: $LW_{\gamma\text{-ATP}} = LW_{PCr} + 14.85$ Hz. This constraint was derived from spectra obtained in this study and from previous experiments, displaying well resolved PCr and γ-ATP resonances (number of spectra = 63, r = 0.78, $P < 0.001$). The resonances arising from 2,3-diphosphoglycerate (2,3-DPG) in the blood obscured the inorganic phosphate (P_i) resonance. Therefore, these signals were fitted with two peaks: one for $\text{2,3-DPG}_{5.4\text{ ppm}}$ and P_i at 5.4 ppm, and one for $\text{2,3-DPG}_{6.3\text{ ppm}}$ at 6.3 ppm.

For each mouse, saturation recovery curves of PCr, γ-ATP and α-ATP were fitted by a mono-exponential function to estimate the corresponding longitudinal relaxation rate constants R_1. Mean R_1 values were used to determine metabolite T_1 values via $R_1 = 1/T_1$, which were used for partial saturation correction.

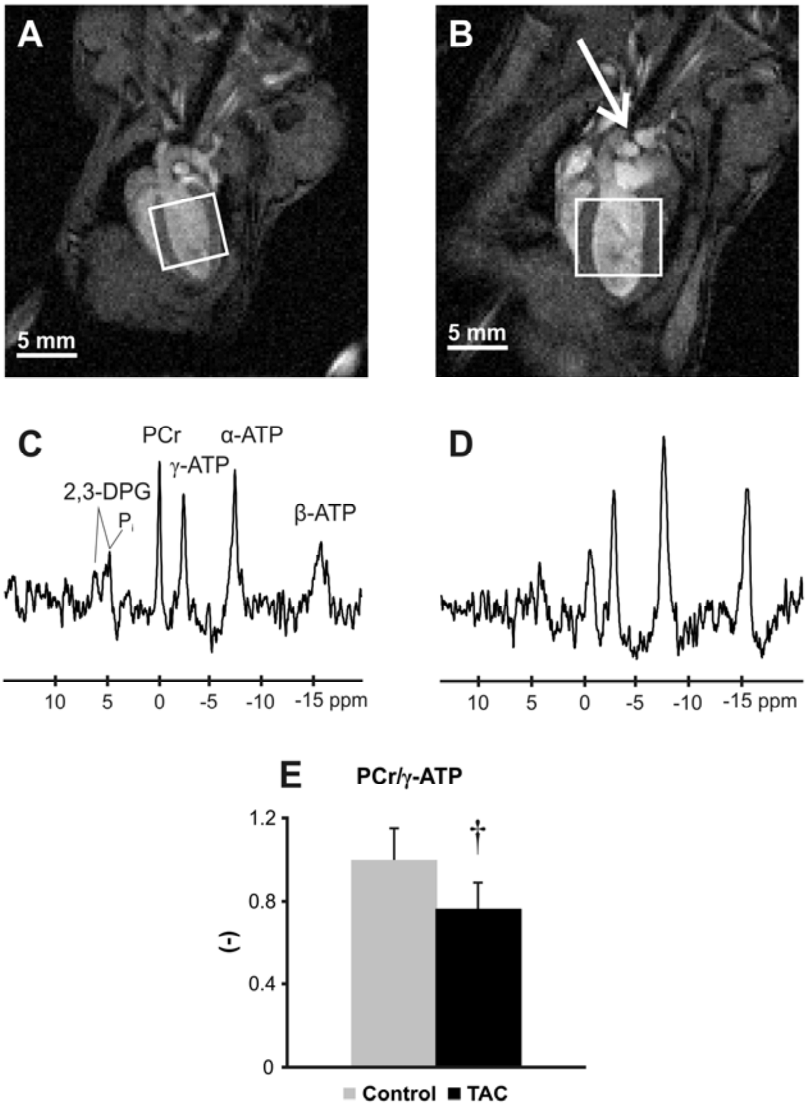

Figure 6.1. End-diastolic left ventricular (LV) MR images obtained from a control mouse (A) and a mouse with a transverse aorta constriction (TAC) (B). The constriction in the TAC mouse is indicated by the arrow. Note the increased LV wall thickness and the increased LV cavity volume, indicating dilated hypertrophic cardiomyopathy in the TAC mouse. The solid rectangles indicate the voxels selected for localized ^{31}P-MRS with 3D ISIS. Panels C and D display ^{31}P MR spectra acquired *in vivo* with 3D ISIS in a healthy mouse heart and a TAC heart, respectively. Peak assignments: 2,3-DPG, 2,3-diphosphoglycerate; PCr, phosphocreatine; α-, β-, γ-ATP, α-, β-, and γ-phosphate groups in adenosine triphosphate; P_i, inorganic phosphate. Myocardial PCr/γ-ATP, corrected for partial saturation, was lower in TAC mice compared to healthy controls (E). Statistical difference between the TAC and control group is indicated by † ($P < 0.01$).

As blood contains ATP, but no PCr, signal contamination from blood in *in vivo* cardiac ^{31}P MR spectra will reduce the apparent myocardial PCr/γ-ATP ratio [24]. Therefore, we checked whether the myocardial PCr/γ-ATP ratio was affected by blood contamination by correlating PCr/γ-ATP to 2,3-DPG$_{6.3\ ppm}$ signal intensity. A significant contribution of signal from ATP in the blood to the cardiac spectra would be reflected by a negative correlation. Furthermore, the [γ-ATP/2,3-DPG$_{6.3\ ppm}$]$_{blood}$ ratio in spectra acquired in fresh blood was determined as a measure for ATP content in blood. The contribution of resonances from blood metabolites to *in vivo* spectra was assessed by quantifying the [2,3-DPG$_{6.3\ ppm}$/γ-ATP]$_{myocardium}$ ratio in the cardiac 3D ISIS spectra. The relative contribution of signal from ATP in the blood to the ATP signal obtained with *in vivo* 3D ISIS was calculated as: [γ-ATP/2,3-DPG$_{6.3\ ppm}$]$_{blood}$ × [2,3-DPG$_{6.3\ ppm}$/γ-ATP]$_{myocardium}$ × 100%.

Myocardial energy status was expressed as the PCr/γ-ATP ratio, corrected for partial saturation. Calculation of intracardiomyocellular Mg^{2+} concentration was based on the chemical shift of β-ATP from PCr [25]. An estimate of P_i signal intensity was made by taking the ratio of the two resonance peaks at 5.4 ppm and 6.3 ppm, of which only the peak at 5.4 ppm overlaps with P_i [26].

Statistical analyses

Data are expressed as mean ± standard deviation (SD). The statistical significance of TAC-induced effects on cardiac function and energy status was analyzed using two-sided unpaired *t*-tests. The level of significance was set at $\alpha < 0.05$.

Results

MRI: LV hypertrophy in TAC mice

We assessed *in vivo* cardiac LV morphology and function from cine MR images to confirm the hypertrophic phenotype and impaired cardiac performance in TAC mice (Table 6.1). Long-axis end-diastolic images obtained from a control mouse and a TAC mouse are shown in Figure 6.1A-B. LV mass was 95% higher in TAC mice compared to healthy mice ($P < 0.001$). This difference persisted after normalization to body weight ($P < 0.001$), indicating LV hypertrophy in TAC mice. Concomitantly, EDV ($P < 0.001$) and ESV ($P < 0.001$) were higher in TAC mice compared to controls. This translated in a lower SV (-33%, $P < 0.001$) and EF (-65%, $P < 0.001$) in TAC mice. Combined, these data illustrate the development of dilated hypertrophic cardiomyopathy with severe systolic dysfunction after 7 weeks of aortic pressure-overload in TAC mice.

^{31}P-MRS: *in vivo* myocardial energy status

Typical ^{31}P MR spectra acquired with 3D ISIS in a healthy mouse heart and a TAC heart are shown in Figure 6.1C-D. Resonances of PCr, and α-, β-, and γ-ATP could be distinguished. Inorganic phosphate (P_i, ~5 ppm) was obscured by 2,3-DPG arising from blood. Spectral line width for PCr was 0.37 ± 0.15 ppm.

Table 6.1. LV morphology and functional parameters obtained with MRI in control mice and TAC mice.

	Control (n = 9)	**TAC (n = 8)**	***P***
Heart mass at autopsy (mg)	101.0±7.2	286.3±38.4	‡
LV mass (mg)	90.0±14.9	175.9±19.1	‡
LV mass/body weight (mg/g)	3.7±0.6	6.0±0.9	‡
End-diastolic volume (µL)	64±11	123±26	‡
End-systolic volume (µL)	21±5.4	94±25	‡
Stroke volume (µL)	43±7.3	29±6.6	‡
Ejection fraction (%)	68±5.6	24±5.2	‡

Statistical differences as compared to the control group are indicated by ‡ ($P < 0.001$).

Conventional unlocalized ^{31}P MR saturation recovery experiments of the mouse chest were performed in order to estimate the high-energy phosphate metabolite T_1 relaxation times at 9.4 T. T_1 values did not differ between control mice and TAC mice, and were 2.54 ± 0.41 s for PCr, 1.09 ± 0.31 s for α-ATP, and 1.45 ± 0.25 s for γ-ATP. Given a TR of 2 s, this resulted in a partial saturation correction factor for PCr/γ-ATP of 1.37 in our 3D ISIS experiments. In a subset of healthy mice (n = 6), 3D ISIS was also performed under fully relaxed conditions. These localized acquisitions yielded a partial saturation correction factor for myocardial PCr/γ-ATP of 1.38 ± 0.28 for spectra acquired at TR = 2 s, which is in good agreement with the value derived from unlocalized saturation recovery experiments.

From localized ^{31}P MR spectra, we derived several myocardial metabolic parameters. Myocardial PCr/γ-ATP, corrected for partial saturation, was lower in TAC mice compared to healthy controls (0.76 ± 0.13 versus 0.99 ± 0.15, $P < 0.01$, Figure 6.1E), which is indicative of a compromised myocardial energy status in TAC mice. Intracardiomyocellular Mg^{2+} concentration was 0.26 ± 0.05 mM in TAC mice, and 0.36 ± 0.12 mM in healthy controls ($P = 0.12$). Semi-quantitative estimation of myocardial P_i levels revealed no differences between groups.

Contribution of signal from metabolites in the blood to the cardiac spectra, estimated via $[2,3\text{-DPG}_{6.3\ \text{ppm}}/\gamma\text{-ATP}]_{\text{myocardium}}$, was similar for both groups, and was 0.18 ± 0.10. In spectra obtained from fresh blood (Figure 6.2), the ATP content in blood was estimated via the $[\gamma\text{-ATP}/2,3\text{-DPG}_{6.3\ \text{ppm}}]_{\text{blood}}$ ratio, which was 0.22 ± 0.14. The relative contribution of signal from ATP in the blood to the ATP signal in cardiac 3D ISIS spectra was therefore approximately 4%. These results show that contamination of ATP from the blood in the 3D ISIS spectra is marginal, and only minimally affects the myocardial PCr/γ-ATP ratio. This was corroborated by the absence of a correlation between the $2,3\text{DPG}_{6.3\ \text{ppm}}$ signal amplitude and the myocardial PCr/γ-ATP ratio determined in the 3D ISIS spectra ($r = 0.04$, $P = 0.88$), implying that signal from ATP in the blood did not significantly contribute to the *in vivo* spectra.

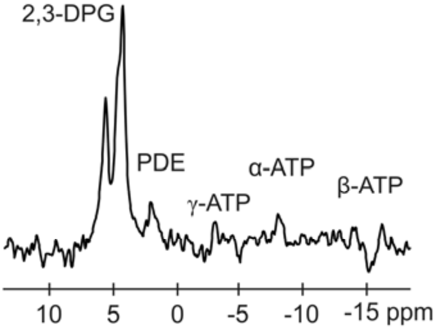

Figure 6.2. ^{31}P MR spectrum obtained from fresh blood. Peak assignments: 2,3-DPG, 2,3-diphosphoglycerate; PDE, phosphodiesters; α-, β-, γ-ATP, α-, β-, and γ-phosphate groups in adenosine triphosphate.

Discussion

With this work, we aimed to establish a noninvasive method to study the *in vivo* myocardial energy status in healthy and diseased mice using 3D ISIS-localized ^{31}P-MRS. We demonstrated the feasibility of a cardiac-triggered, respiratory-gated 3D ISIS method for volume-selective signal acquisition. Adequate cancelation of unwanted signals was ensured by employing dummy excitations during respiratory gates, maintaining a constant TR to achieve equal longitudinal magnetization for subsequent ISIS acquisitions. Using a ^{1}H/^{31}P MR setup, 3D ISIS-localized ^{31}P-MRS was combined with cine ^{1}H MR imaging to assess morphological, functional and metabolic parameters in a single experimental session of less than 2 hours. With this approach, we identified a reduced myocardial energy status, evidenced by a lower PCr/γ-ATP ratio, accompanied by hypertrophic growth and impaired myocardial function in a surgical mouse model of HF.

The small heart size and the high heart rate in mice require adequate strategies to avoid contamination and to maximize sensitivity for cardiac ^{31}P-MRS. A surface coil has superior sensitivity over a volume resonator, and is therefore beneficial for ^{31}P MR signal reception. However, in *in vivo* cardiac ^{31}P-MRS, skeletal muscle from the chest is located in the most sensitive area of the surface coil, and can contribute considerably to the received signal [9]. Therefore, localized acquisitions are essential to restrict the obtained spectra to the heart. If CSI techniques are used for localized signal acquisition, Fourier bleeding can be an important contributor to signal contamination, which is exacerbated in a surface coil setup [5,14,15,18,27]. Typically, single-voxel localization techniques provide better-defined signal localization than CSI methods [7]. We minimized contamination from tissues other than the myocardium by using the single-voxel approach of cardiac-triggered, respiratory-gated 3D ISIS. In addition, we combined the benefit of B_1 homogeneity obtained by volume coil RF transmission with the superior sensitivity of surface coil signal reception.

Myocardial PCr/γ-ATP ratio in healthy mice was 0.99 ± 0.15. This value is on the lower range of the PCr/ATP values reported in literature, with an average reported value of about 2 for both humans and mice [8,9,14,15]. It has been recognized that many aspects of localized ^{31}P-MRS acquisition and quantification can contribute to the variability in the PCr/ATP values reported in literature, and that comparisons between laboratories should be made with the differences in the methods used in mind [9,27,28]. The three main causes for apparent discrepancies in literature reports are laboratory-dependent differences in correction for partial saturation, contamination of the spectra by signal from the liver or skeletal muscle tissue, and contamination by blood in the LV cavity and the correction thereof [9]. In the following, each of these issues will be addressed for the current study.

Partial saturation correction

For the correction of partial saturation effects, we used the metabolite T_1 relaxation times as determined by unlocalized saturation recovery experiments. Since the T_1 values in chest skeletal muscle could be different from those in cardiac muscle, we validated the correction factor in healthy mice by acquiring localized spectra from the LV myocardium under fully relaxed conditions [29]. Indeed, the partial saturation correction factor derived from unlocalized saturation recovery experiments was in agreement with measurements localized to the heart. This observation confirms a prior assumption [15] that in the healthy mouse the T_1(PCr)/T_1(γ-ATP) ratio is essentially the same for chest skeletal muscle and myocardium at 9.4 T. Furthermore, the T_1 relaxation times from unlocalized saturation recovery experiments were not different between healthy and TAC mice. This justifies the use of a general partial saturation correction factor for all mice in the present study. When studying other experimental groups of mice, these assumptions will need to be verified for the particular mouse model under investigation.

Minimizing signal contamination

As 3D ISIS requires multiple acquisitions for signal localization, the method is particularly sensitive to motion artifacts and consequential contamination from tissues surrounding the heart such as liver and skeletal muscle from the chest. Additional contamination can be introduced through so-called 'T_1-smearing', which is caused by differences in longitudinal magnetization between subsequent acquisitions within one ISIS cycle due to imperfect flip angle of the excitation pulse combined with a $TR < 5 \times T_1$ [16,17]. Similar effects occur when TR is not constant between acquisitions, while measuring at $TR < 5 \times T_1$. Previous studies in rodents and in humans using 3D ISIS for cardiac applications did not measure at constant TR, nor under fully relaxed conditions [8,30-32]. This is the first report of a cardiac-triggered, respiratory-gated 3D ISIS sequence that is combined with dummy excitations during respiratory gates, to ensure localized inversion of the LV signal at identical cardiac and respiratory phases for all acquisitions, whilst maintaining a constant TR. In addition, a volume coil was used for the homogeneous transmission of the adiabatic inversion pulses and a calibrated 90° excitation pulse to minimize T_1 smearing. This approach may find applications beyond investigations of *in vivo* myocardial energy status in the mouse, because localized ^{31}P-MRS from the liver will also benefit from the strategy proposed here [33].

In the present study, the PCr/γ-ATP ratio was calculated as a measure for the myocardial energy status. In some studies of the mouse heart, β-ATP was used in this calculation [8,14]. We used the γ-ATP peak for several reasons. First of all, the β-ATP resonance is at the edge of the excitation pulse bandwidth used here, which may result in imperfect excitation of β-ATP and consequently an underestimation of the β-ATP signal. Secondly, the chemical shift difference between PCr and γ-ATP is only 2.48 ppm, while it is 16.26 ppm for PCr and β-ATP. The PCr/γ-ATP ratio is therefore less affected by the chemical shift displacement artifact than the PCr/β-ATP ratio, particularly at high field strengths. Indeed, with the inversion pulse used here (bandwidth = 37.5 ppm), the chemical shift displacement of the voxel selected for PCr relative to that for β-ATP at -16.26 ppm is 43% in one direction, corresponding to only 18% overlap of the voxels selected for both resonances. For PCr relative to γ-ATP, the displacement is only 6.6%, with 81% overlap of the voxels.

Correcting for blood contamination

Blood in the LV cavity contains ATP, but no PCr. If signal from ATP in the blood contributes to the signal acquired from the voxel of interest, the calculated myocardial PCr/ATP ratio may be underestimated [34]. A correction factor can be applied to account for signal contribution from ATP in the blood to the spectra, which depends on both the amount of ATP in the blood and the amount of blood contributing to the spectrum. We showed that the amount of ATP signal from fresh blood, in terms of $[\gamma\text{-ATP}/2,3\text{-DPG}_{6.3\ \mathrm{ppm}}]_{\mathrm{blood}}$, was approximately 20%, which is consistent with previous reports of ^{31}P-MRS studies of blood in humans and mice [8,12,24,35]. The contribution of signal from metabolites in blood to the *in vivo* 3D ISIS spectra, estimated via $[2,3\text{-DPG}_{6.3\ \mathrm{ppm}}/\gamma\text{-ATP}]_{\mathrm{myocardium}}$, was less than 20% and was not different between healthy and TAC mice. The high velocity of flowing blood during acquisition may attenuate the peaks from blood metabolites in spectra obtained *in vivo* [36]. Based on these considerations, we estimated that the contribution of signal from ATP in the blood to the ATP signal in *in vivo* 3D ISIS spectra was only 4%, and concluded that correcting for blood contamination was not necessary in this study. Again, these assumptions may not hold for other mouse models of disease [8,24].

Using cine ^{1}H MR imaging, cardiac function and morphology was quantified in TAC mice and healthy control animals. As expected, global hypertrophic remodeling of the LV was observed in the TAC mice, evidenced by a high EDV and a high LV mass compared to control mice. This finding was corroborated by the elevated heart weight in TAC mice at autopsy. Cardiac function, in terms of EF and SV, were severely impaired in the TAC mice, indicating an advanced state of HF. These functional and morphological changes, combined with the ~25% decrease of the PCr/γ-ATP ratio in TAC mice compared to healthy controls, are consistent with previous studies on patients and mice [18,37-39].

With our current approach, it is not possible to detect changes in myocardial PCr or ATP concentration separately. Similar decreases in both PCr and ATP concentrations can render the PCr/ATP ratio insensitive to alterations in myocardial energy status. An absolute quantification of metabolites might therefore be more sensitive to changes in cardiac energy metabolism [40]. In addition, absolute values would allow for a more straightforward comparison of results obtained with different methods. Nonetheless, a reduced PCr/ATP ratio has been shown to be an important indicator of disease severity and can be of prognostic value in treatment planning [41].

A drawback of using single-voxel localized ^{31}P-MRS is that the cardiac energy status cannot be assessed at a regional scale, which could be of importance in investigations of myocardial ischemia. However, many preclinical animal studies focus on pathologies that have a global effect on the heart, such as aortic stenosis, diabetes, and inborn errors of metabolism. For these investigations, the current 3D ISIS approach for localized ^{31}P-MRS can be a valuable addition to the toolbox of mouse cardiac MR methods [2].

Conclusion

The present work describes a noninvasive approach to assess myocardial energy status in the *in vivo* mouse using single-voxel localized ^{31}P-MRS. The method encompasses a cardiac-triggered, respiratory-gated 3D ISIS sequence with dummy excitations during respiratory gates, to ensure a well-defined localization of signal acquisition. The method is able to identify differences in high-energy phosphate metabolism between the healthy mouse heart and a widely used model for HF, the TAC mouse. Furthermore, the 3D localized spectra can be obtained within 45 minutes, leaving room for measurements of cardiac function with MRI during the same experimental session. We anticipate that localized ^{31}P-MRS will provide valuable contributions to preclinical investigations of cardiac disease progression and therapeutic intervention efficacy.

Acknowledgements

We thank L. de Graaf and T.R. Geraedts for designing the animal support cradle and the surface coil, E.C.M. Kneepkens for her contributions to the pulse sequence design, and L.B.P. Niesen for biotechnical assistance. B.J. van Nierop is supported by the Center for Translational Molecular Medicine, project TRIUMPH (grant number 01C-103) and the Dutch Heart Foundation. S.M. Houten and J.J. Prompers are supported by VIDI grants (project numbers 016.086.336 and 700.58.421, respectively) from the Netherlands Organisation for Scientific Research (NWO), and G.J. Strijkers is supported by a VIDI grant (number: 07952) from the Dutch Technology Foundation STW, applied science division of NWO and the Technology Program of the Ministry of Economic Affairs.

References

1. Geelen, T., et al. NMR Biomed, 2012, 25(8), 953-68.
2. Coolen, B.F., et al. NMR Biomed, 2012, 25(8), 969-84.
3. Neubauer, S. N Engl J Med, 2007, 356(11), 1140-51.
4. Weiss, R.G., et al. N Engl J Med, 1990, 323(23), 1593-600.
5. Keevil, S.F. Phys Med Biol, 2006, 51(16), R579-636.
6. Ordidge, R.J., et al. J Magn Reson, 1986, 66, 283-94.
7. De Graaf, R.A. In vivo NMR spectroscopy : principles and techniques. Chichester, West Sussex, England ; Hoboken, NJ: John Wiley & Sons, 2007.
8. Omerovic, E., et al. Biochem Biophys Res Commun, 2000, 271(1), 222-8.
9. Bottomley, P.A. NMR Spectroscopy of the Human Heart. Encyclopedia of Magnetic Resonance: John Wiley & Sons, Ltd, 2007.
10. Headrick, J.P., et al. Am J Physiol, 1994, 267(3 Pt 2), H1074-84.
11. Nicolay, K., et al. Biochim Biophys Acta, 1987, 929(1), 5-13.
12. Lee, J., et al. J Magn Reson Imaging, 2006, 24(6), 1269-76.
13. Kolwicz, S.C., Jr., Tian R. J Vis Exp, 2010, doi: 10.3791/2069.
14. Chacko, V.P., et al. Am J Physiol Heart Circ Physiol, 2000, 279(5), H2218-24.
15. Flogel, U., et al. Magn Reson Med, 2007, 57(1), 50-8.
16. Lawry, T.J., et al. Magn Reson Med, 1989, 9(3), 299-314.
17. Keevil, S.F., et al. NMR Biomed, 1992, 5(4), 200-8.
18. Maslov, M.Y., et al. Am J Physiol Heart Circ Physiol, 2007, 292(1), H387-91.
19. Rockman, H.A., et al. Proc Natl Acad Sci U S A, 1991, 88(18), 8277-81.
20. van Nierop, B.J., et al. PLoS ONE, 2013, 8(2), e55424.
21. Bakermans, A.J., et al. Circ Cardiovasc Imaging, 2011, 4(5), 558-65.
22. Heijman, E., et al. J Magn Reson Imaging, 2008, 27(1), 86-93.
23. Vanhamme, L., et al. J Magn Reson, 1997, 129(1), 35-43.
24. Horn, M., et al. Magn Reson Mat Phys Biol Med, 1993, 1(2), 55-60.
25. Iotti, S., et al. NMR Biomed, 1996, 9(1), 24-32.
26. Lamb, H.J., et al. Circulation, 1997, 96(9), 2969-77.
27. Bottomley, P.A. Radiology, 1991, 181(2), 344-50.
28. Lamb, H.J., et al. NMR Biomed, 1996, 9(5), 217-27.
29. van Dobbenburgh, J.O., et al. NMR Biomed, 1994, 7(5), 218-24.
30. Schaefer, S., et al. J Am Coll Cardiol, 1988, 12(6), 1449-55.
31. van der Meer, R.W., et al. Diabetes, 2007, 56(12), 2849-53.
32. Fragasso, G., et al. Am Heart J, 2011, 162(1), 136-41.
33. Solanky, B.S., et al. Toxicol Sci, 2012, 126(2), 306-16.
34. Hardy, C.J., et al. Am Heart J, 1991, 122(3 Pt 1), 795-801.
35. Krahe, T., et al. Rofo, 1993, 159(1), 64-70.
36. Zhang, J., et al. Am J Physiol, 1995, 268(5 Pt 2), H1891-905.
37. Gupta, A., et al. Circ Cardiovasc Imaging, 2011, 4(1), 42-50.
38. Neubauer, S., et al. J Investig Med, 1997, 45(8), 453-62.
39. Lamb, H.J., et al. Circulation, 1999, 99(17), 2261-7.
40. Gupta, A., et al. Am J Physiol Heart Circ Physiol, 2009, 297(1), H59-H64.
41. Neubauer, S., et al. Circulation, 1997, 96(7), 2190-6.

7

Mouse cardiac function and energetics during the onset of hypertrophy and their relation to subsequent remodeling

Bastiaan van Nierop, Adrianus Bakermans, Desiree Abdurrachim, Ingeborg van der Made, Klaas Nicolay, Gustav Strijkers, and Jeanine Prompers

Abstract

Background: A well-established measure of *in vivo* myocardial energetics is the PCr/ATP ratio obtained from ^{31}P-MRS. PCr/ATP is known to be reduced in the failing heart. Previously, it was reported for a mouse model of cardiac hypertrophy induced by transverse aortic constriction (TAC) that PCr/ATP measured at week 3 after TAC was predictive for subsequent adverse ventricular remodeling. In this study, we investigated whether PCr/ATP during the onset of TAC induced hypertrophy also predicts subsequent remodeling.

Methods: C57BL/6 mice (n = 35) underwent TAC resulting in pressure overload induced left ventricular (LV) hypertrophy. PCr/ATP was quantified using localized ^{31}P-MR spectroscopy *in vivo* at the day of TAC surgery or 4 days thereafter, and correlated to LV function (end-diastolic and end-systolic volume, ejection fraction, stroke volume, cardiac output) and LV mass measured 7 and 10 weeks after TAC, using MR imaging.

Results: At the day of surgery after TAC (day 0) an instantaneous impairment of LV function was observed. PCr/ATP (0.85 ± 0.12) showed a trend towards lower values as compared to previously obtained values in control mice (0.99 ± 0.15, $P = 0.67$). PCr/ATP at day 4 was significantly decreased (0.75 ± 0.23, $P = 0.01$). Importantly, no correlation was noted between PCr/ATP and LV function or mass at day 4. PCr/ATP at day 4 also did not correlate to LV function or mass at weeks 7 or 10 after TAC. However, significant correlations were observed between LV function (except for end-diastolic volume) or mass at day 4 with corresponding parameters at weeks 7 and 10 ($r > 0.52$, $P < 0.05$). Correlations of functional parameters between day 0 with respect to weeks 7 and 10 were absent.

Conclusion: PCr/ATP measured at the same day of TAC surgery showed a trend towards lower values and became significantly lower than control mice at day 4. Importantly, PCr/ATP measured at these time points during the first stage of hypertrophic growth, did not predict functional and anatomical indicators of subsequent remodeling. Instead, significant correlations were found between cardiac functional parameters at day 4 after TAC with the same parameters 7 and 10 weeks after TAC.

Introduction

Heart failure (HF) is a progressive syndrome in which the heart is no longer capable of pumping blood at a rate sufficient for fulfilling the peripheral needs [1]. HF is an important cause of morbidity and mortality worldwide [2-4]. In many patients, HF results from sustained, systemic hypertension accompanied by a pressure overload of the left ventricle (LV) [5]. The heart initially adapts to this overload by means of hypertrophic growth. However, a broad range of concomitant maladaptive processes, including increased collagen deposition, metabolic remodeling and microvascular adaptation, eventually lead to HF [6-8].

The metabolic changes that occur in HF affect substrate utilization, oxidative phosphorylation, and adenosine triphosphate (ATP) transfer and utilization [8]. An important effect of the derangements in these metabolic pathways is a reduction in phosphocreatine (PCr), that acts as an energy buffer and is a key molecule for the energy transport from production to utilization site in the cell, and eventually even a reduction of the available ATP, a high-energy phosphate compound that serves as the direct energy source to drive myocardial function [9]. Ultimately, metabolic remodeling in HF results in reduced myocardial energy supplies. Given the high energy demand of the heart, this has detrimental consequences and results in impaired LV function [10].

Phosphorous-31 magnetic resonance spectroscopy (^{31}P-MRS) provides a unique, noninvasive means to assess high-energy phosphate compounds involved in cardiac energy metabolism [11]. Cardiac ^{31}P-MRS can be used to quantify the phosphocreatine-to-ATP ratio (PCr/ATP), which is a well recognized measure of the myocardial energy status and which has been shown to be decreased in a wide variety of pathologies resulting in HF [12]. Moreover, PCr/ATP may predict cardiovascular mortality due to dilated cardiomyopathy [13].

Transverse aortic constriction (TAC) in mice is a highly relevant mouse model of pressure overload induced hypertrophy and plays an important role in preclinical research to unravel the precise role of metabolic remodeling in HF development [14-19]. Previously it was shown that PCr/ATP measured in hearts of mice with a compensated stage of hypertrophy measured three weeks after TAC predicted subsequent LV remodeling and impaired function[17]. These results suggested that energetic abnormalities contribute to disease progression at this stage of remodeling following TAC. Three weeks after TAC, the hearts had already undergone considerable remodeling resulting in doubling of LV mass. An important question that remained was whether PCr/ATP, measured during the onset of hypertrophy, can predict subsequent heart remodeling.

This study builds on previous work by Bakermans *et al.*, who implemented 3D Image Selected *In vivo* Spectroscopy (ISIS) for localized ^{31}P-MRS of the mouse heart (Chapter 6) [20]. With ^{31}P-MRS a significantly decreased PCr/ATP was measured 7 weeks after TAC surgery as compared to healthy controls. Here, we exploited this method to study the energy status of the TAC heart at the day of surgery, and when the first signs of hypertrophic growth become evident 4 days after TAC. These findings were related to LV function and mass determined concurrent with the ^{31}P spectra, as well as to functional status 7 and 10 weeks after surgery.

Methods

Animal handling

A total of 35 C57BL/6 mice (♂, age 11 weeks, 23-27 grams) were included in this study. Animals were housed under standard laboratory conditions with a 12 hour light/dark cycle and were maintained on a standard diet with access to water *ad libitum*. All animal experiments were performed according to the Directive 2010/63/EU of the European Parliament and approved by the Animal Care and Use Committee of Maastricht University.

Animal model

All mice underwent a surgically induced TAC, resulting in LV pressure overload [14,21]. Briefly, mice were anesthetized with 2.5 vol% isoflurane in 0.2 L min^{-1} O_2 and 0.2 L min^{-1} medical air and intubated for mechanical ventilation. Animals were placed on a heating pad to maintain body temperature at 37 °C. Buprenorphine (0.1 mg/kg s.c.) was administered for analgesia. Surgical procedures were performed using a stereo microscope (Leica M80). A small incision was made just lateral from the sternum above the first intercostal space. The aortic arch was exposed and tied off (6-0 silk suture) together with a 27G (Ø 0.42 mm) needle between the innominate artery and the left common carotid artery to induce TAC, respectively. The needle was immediately removed, restoring blood flow. The chest was then closed and the animals were allowed to recover in a 30 °C recovery chamber.

Study protocol

MR measurements were performed either at the day of TAC after surgery (day 0; n = 9) or 4 days after surgery (day 4; n = 19) to quantify the PCr/ATP ratio, as a measure of the myocardial energy status, and global LV function from cinematographic MRI. In addition, one (n = 9), seven (n = 26) and ten weeks (n = 24) after surgery cinematographic MRI measurements were obtained. Immediately after the last measurements the anesthetized animals were killed by means of perfusion of the vascular bed with phosphate buffered saline (10 mL, pH 7.4), which was infused via a needle penetrating the apex, and exsanguination from the vena cava inferior. Next, the integrity of the aortic band was visually verified, and whole heart and lung wet weight (LuW) and tibia length (TL) were measured.

MR examinations

All MR data was acquired using a 9.4 T small animal MRI scanner (Bruker BioSpec, Ettlingen, Germany) equipped with a 740 mT/m gradient set. Mice were anesthetized with isoflurane (4.0 vol% for induction, 1.5-2.0 vol% for maintenance) in medical air (0.4 L min^{-1}). The front paws were taped onto gold-coated ECG electrodes and a balloon pressure sensor was placed on the abdomen. Body temperature was maintained at 36-37^{o}C with a heating pad and monitored with a rectal temperature sensor.

Cardiac ^{31}P-MRS was performed as described previously [20]. Briefly, mice were positioned prone in a purpose-built support cradle with the heart above a custom-built, actively decoupled, two-turn ^{31}P surface coil (Ø 15 mm) for signal reception. In addition, a volume coil (Ø 54 mm) composed of a quadrature ^{1}H birdcage resonator and a linear ^{31}P birdcage resonator (RAPID Biomedical GmbH, Rimpar, Germany), was used for ^{1}H-MR imaging and shimming, and for radiofrequency (RF) transmission for ^{31}P-MRS, respectively.

A cardiac-triggered, respiratory-gated FLASH sequence was used to acquire cine ^{1}H-MR image series of 14-17 frames per cardiac cycle (Chapter 2). Three LV short-axis slices and four- and two-chamber long-axis views were acquired, and used for quantification of LV function and morphology as well as for anatomical reference during 3D ISIS voxel planning for localized ^{31}P-MRS. Imaging parameters were: pulse repetition time (TR) = 7 ms, echo time (TE) = 1.8 ms, number of signal averages (NA) = 4, $\alpha = 15°$, field of view (FOV) = 3×3 cm^2, matrix = 128×128.

Subsequently, an 11×11×11 mm^3 cubic voxel in the sensitive area of the surface coil was shimmed manually by minimizing the water line width in ^{1}H spectra acquired with a cardiac-triggered, respiratory-gated PRESS sequence [22]. Pulse power to achieve maximal signal from the ^{31}P sinc excitation pulse (pulse length = 1.2 ms, bandwidth = 32.0 ppm) was determined in a previous study and proved constant between animals [20]. To confirm the appropriateness of the partial saturation correction factor used in the present study (see Data analysis), unlocalized ^{31}P-MR spectra were acquired using conventional saturation recovery experiments. ^{31}P-MR parameters

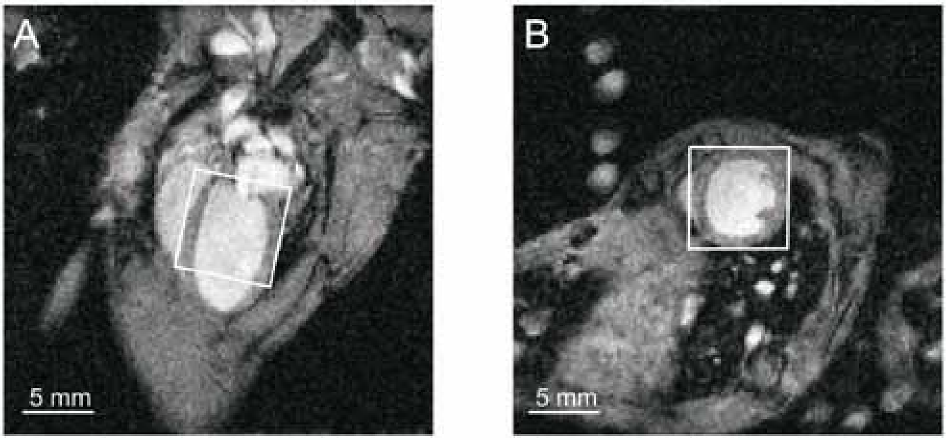

Figure 7.1. End-diastolic LV MR images in a long-axis (A) and a short-axis orientation (B) obtained in a mouse at the day of TAC after surgery. The solid rectangles indicate the voxels selected for localized ^{31}P-MRS with 3D ISIS.

were: 1.2 ms sinc excitation pulse, bandwidth = 32.0 ppm, γ-ATP on resonance, TR = 2 s and 15 s, NA = 128 and 32.

Next, a cardiac-triggered, respiratory-gated ISIS sequence was used for localized ^{31}P-MRS [23]. A 160 - 333 µL cubic voxel, dependent on heart size, was positioned to enclose the end-diastolic LV (Figure 7.1). ISIS parameters were: TR ≈ 2 seconds, 96 ISIS cycles (768 scans) preceded by 1 dummy cycle, 6.25 ms 180° adiabatic hyperbolic secant inversion pulses (bandwidth = 37.5 ppm), 1.2 ms 90° sinc excitation pulse (bandwidth = 32.0 ppm), γ-ATP on resonance.

For cinematographic MRI measurements performed at 1, 7 and 10 weeks after TAC a 72-mm-diameter quadrature transmit coil in combination with a 4 element phased-array receive coil (Bruker) was used [24,25]. Briefly, LV function and mass were quantified from 2 long-axis and a stack of 3 short-axis cinematographic MR images with 14-17 frames per cardiac cyclic covering the complete cardiac cycle using an ECG-triggered and respiratory-gated FLASH sequence. Imaging parameters were: TR = 7ms, TE = 1.8 ms, NA = 6, α = 15, FOV 30 × 30 mm^2, matrix = 192 × 192.

Data analysis

The myocardial wall was segmented semi-automatically in the cine MR images using CAAS MRV FARM (Pie Medical Imaging, The Netherlands) to obtain LV end-diastolic volume (EDV), end-systolic volume (ESV), ejection fraction (EF), stroke volume (SV), cardiac output (CO) and LV mass [26], and compared to data available in our laboratory from age-matched C57BL/6 control mice (♂, n = 13), which was measured with a similar cine MR protocol (Chapter 2 and Chapter 4).

Cardiac ^{31}P-MR spectra were analyzed as follows. Fitting of the metabolite signals to Lorentzian line shapes was performed in the time domain using AMARES in jMRUI [20]. Briefly, the PCr resonance at 0.00 ppm was used as an internal chemical shift reference. The ATP resonances at -2.48 ppm (γ; doublet), -7.52 ppm (α; doublet) and -16.26 (β; triplet) were fitted with equal amplitudes and line widths within each multiplet, and a J-coupling constant of 17 Hz. The γ-ATP line widths ($LW_{\gamma\text{-ATP}}$) were constrained relative to the PCr line width (LW_{PCr}) according to an empirically determined relation: $LW_{\gamma\text{-ATP}} = LW_{PCr} + 14.85$ Hz (data collected from previous studies in our group; number of spectra = 63; r = 0.78; $P < 0.001$). The resonances arising from 2,3-diphosphoglycerate (2,3-DPG) in the blood obscured the inorganic phosphate (Pi) resonance. Therefore, these signals were fitted with two peaks: one for 2,3-$DPG_{5.4\ ppm}$ and Pi at 5.4 ppm, and one for 2,3-$DPG_{6.3\ ppm}$ at 6.3 ppm.

Myocardial energy status was expressed as the PCr/γ-ATP ratio as determined from the unlocalized ^{31}P-MR spectra. PCr/γ-ATP had to be corrected for partial T_1 saturation. In a previous study in our laboratory the T_1 values of PCr and γ-ATP were determined from unlocalized, conventional saturation recovery experiments, and found to be 2.54 ± 0.41 s and 1.45 ± 0.25 s, respectively (Chapter 6). Both T_1 values of PCr and γ-ATP did not differ between control and TAC mice. Cardiac ^{31}P-MR spectra were thus obtained under partially saturated conditions, since TR (2 s) < 5 × T_1, for PCr and γ-ATP. A partial saturation correction factor was determined in the previous study from fully relaxed (TR ≈ 15 s) 3D ISIS ^{31}P-MR measurements and from the PCr and γ-ATP T_1 times (Chapter 6), yielding a partial saturation correction factor of 1.38 of PCr/γ-ATP. In the present study, PCr/γ-ATP was therefore corrected for partial saturation by multiplying with 1.38.

Statistics

Data are expressed as mean ± standard deviation (SD). An ANOVA for repeated measures was used to test for within group differences of LV EDV, ESV, EF, SV, CO, LV mass, bodyweight, heart rate (HR) and respiratory rate over time. Separate tests were used for the control group, and the TAC groups that underwent MRI at the day of surgery or 4 days thereafter. Differences in PCr/ATP measured in control and TAC hearts were assessed using a one-way ANOVA. When appropriate, ANOVA tests were followed by the Bonferroni post-hoc test. A two-sided, unpaired Students *t*-test was used to compare the time-averaged parameters between groups. Between group differences in whole heart wet weight and lung wet weight normalized to TL were tested using a two-sided unpaired Student's *t*-test for unequal variances. Linear regression analysis with offset was used to correlate PCr/ATP at day 0 or 4, to LV parameters (EDV, ESV, SV, EF, CO or LV mass) determined either at the same time point, 7 weeks after surgery, 10 weeks after surgery, or to the change of a certain LV parameter from 7 to 10 weeks after surgery. Linear regression analysis with offset was also used to correlate LV parameters as determined at day 0 or 4, to LV parameters measured 7 and 10 weeks after surgery. Calculations were performed using SPSS 19.0 (SPSS Inc., Chicago). For all tests the level of significance was set at $\alpha = 0.05$.

Results

Four TAC mice died shortly after surgery. One mouse was found dead in its cage at 51 days after TAC induction, most likely as a result of acute decompensated HF or arrhythmias. Three TAC mice were sacrificed before the end of the experiment for animal welfare reasons. General animal characteristics are given in Table 7.1, and compared to data previously obtained under similar conditions in age- and gender matched, healthy control mice in our laboratory. Mouse bodyweight increased over time in both groups ($P < 0.05$), but no significant differences between groups were detected. Respiratory rate during MRI scanning was constant between measurements in both groups, but higher as compared to the control group ($P < 0.001$). HR during MRI measurements was constant between measurements in the control group. HR was slightly lower in TAC than control mice ($P < 0.01$). In TAC mice HR at the day of surgery was significantly lower as compared to the HR during other measurements ($P < 0.01$).

Table 7.1. Mouse body (BW) (g) weight as determined before the MRI measurements, and heart rate (HR) (min^{-1}), and respiratory rate (Resp) (min^{-1}) as determined during the MRI measurements at the different time points in the study for the control and TAC mice. BW increased significantly over time in both groups ($P < 0.001$), but no significant differences between groups were detected. HR was similar in both groups, however, HR during MRI measurements in the TAC mice at the day of surgery was significantly lower as compared to the other time points ($P < 0.001$).

		Day 0	**Day 4**	**Week 1**	**Week 7**	**Week 10**
BW (g)	Control	-	-	25.3±1.7	27.1±1.4	28.4±1.6
	TAC	25.1±2.0	24.8±1.5	24.7±0.9	27.1±1.7	28.0±2.1
HR (min^{-1})	Control	-	-	520±37	539±31	529±35
	TAC	385±49‡	495±52	518±43	495±50	497±54
Resp (min^{-1})	Control	-	-	68±9	76±19	77±18
	TAC	84±9	87±10	94±12	86±12	86±9

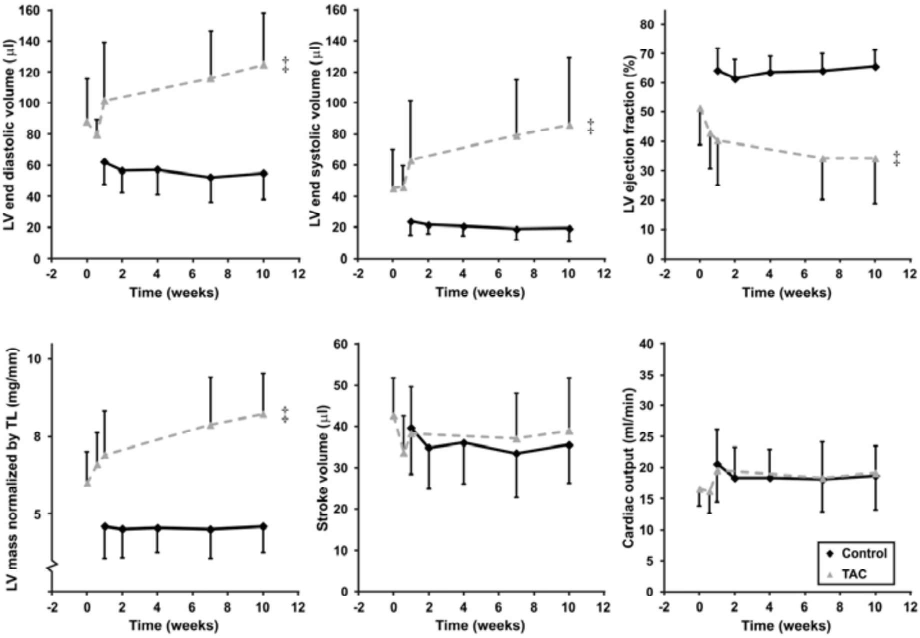

Figure 7.2. Left ventricular (LV) end-diastolic volume (top left), end-systolic volume (top middle), ejection fraction (top right), LV mass normalized to tibia length (TL) (bottom left), stroke volume (bottom middle), and cardiac output (bottom right) as a function of time. Time point zero indicates the day of surgery. The dotted line in the TAC group is to guide the reader. Statistical differences between the control and TAC group are indicated by ‡ ($P < 0.001$).

LV functional status was determined from cinematographic MR images (Figure 7.2). In control mice no significant differences between measurements were detected for EDV (56 ± 15 μL), ESV (20 ± 8 μL), EF (65 ± 6%), LV mass (4.6 ± 0.9 mg/mm), SV (36 ± 10 μL) and CO (19 ± 5 mL $\min^{-1}$). Possible between group differences in LV functional and morphological data were assessed from time-averaged parameters. Impaired systolic function in the TAC mice was apparent from an increased EDV ($P < 0.001$) and ESV ($P < 0.001$), and a decreased EF ($P < 0.001$) as compared to control mice. Myocardial hypertrophy in TAC mice was manifested as a significantly increased LV mass normalized to TL as compared to controls ($P < 0.001$). No between groups differences were observed for SV and CO.

In TAC mice, EDV increased over time from 88 ± 28 μL to 125 ± 33 μL at 10 weeks after surgery, ESV increased from 45 ± 25 μL to 86 ± 43 μL, EF decreased from 51 ± 12% to 34 ± 15%, and LV mass gradually increased from 6.0 ± 1.0 mg/mm to 8.2 ± 1.3 mg/mm. Moreover, these parameters changed significantly over time ($P < 0.05$, in all cases), except for the change of EDV and ESV in the mice that underwent MR measurements at the day of surgery (*P* = 0.09 and *P* = 0.08, respectively). Altogether, these results demonstrate maladaptive LV remodeling. No significant differences were detected in SV (38 ± 11 µL) and CO (18 ± 5 mL min^{-1}) between measurements.

Post-mortem whole heart wet weight was significantly higher in TAC mice as compared to controls ($P < 0.001$) (Table 7.2). The presence of pulmonary remodeling was assessed from the lung wet weight-to-TL ratio, which was significantly higher in TAC mice compared to control animals ($P < 0.01$).

Table 7.2. Post mortem heart wet weight-to tibia length (TL) ratio (mg/mm) was higher in TAC mice as compared to controls. Lung weight-to-tibia length (LuW/TL) ratio (mg/mm) was also higher in TAC mice compared to controls.

Group	Heart mass/TL (mg/mm)	LuW/TL (mg/mm)
Control	8.6 ± 1.0	9.7 ± 1.3
TAC	14.8 ± 3.6‡	13.6 ± 7.2†

Statistical differences as compared to the control group are indicated by † ($P < 0.01$) and ‡ ($P < 0.001$).

Figure 7.3 shows an example of a cardiac ^{31}P-MR spectrum as obtained at the day of surgery and day 4. PCr/ATP was quantified from the ^{31}P-MR spectra as measure for the myocardial energy status. PCr/ATP was underestimated due to partial T_1 saturation and was therefore corrected using an extensively validated correction factor (1.38) determined in a previous study, for which no significant differences were found between control and TAC mice (Chapter 6). The suitability of this correction factor for the data in the present study was tested for using unlocalized ^{31}P-MR spectra, acquired using conventional saturation recovery experiments. Indeed, this approach yielded the same correction factor as determined with saturation recovery experiments in the previous study.

On average, the corrected myocardial PCr/ATP ratio was 0.85 ± 0.12 at day 0 and 0.75 ± 0.23 at day 4 (Figure 7.4). Previously, we found that PCr/ATP in control mice was 0.99 ± 0.15 and that it was 0.76 ± 0.13 seven weeks after TAC [20]. Potential differences between PCr/ATP, corrected for partial saturation, in control mice, and the 3 different time points after TAC induction, were assessed using a one-way ANOVA. Only the decrease of PCr/ATP at day 4 after TAC was significant (*P* = 0.01).

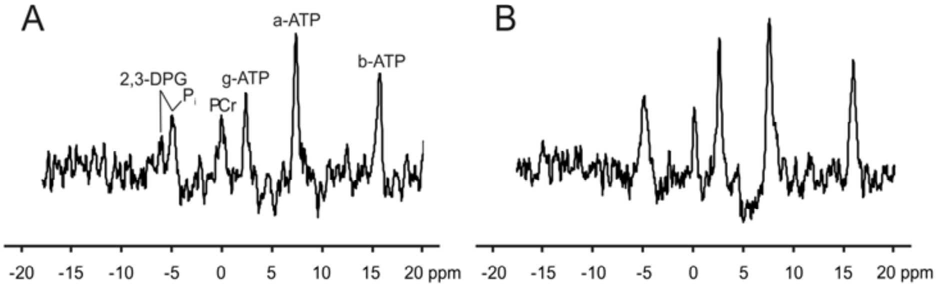

Figure 7.3. ^{31}P-MR spectra acquired *in vivo* with 3D ISIS in different TAC hearts at (A) day 0 and (B) day 4. Peak assignments: 2,3-DPG, 2,3-diphosphoglycerate; PCr, phosphocreatine; α-, β-, γ-ATP, α-, β-, and γ-phosphate groups in adenosine triphosphate; P_i, inorganic phosphate.

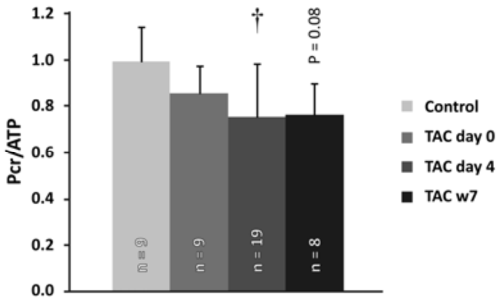

Figure 7.4. PCr/ATP, corrected for partial saturation, in control mice and TAC mice at day 0, day 4, and at 7 weeks after TAC. PCr/ATP showed a trend towards decrease at day 0, and a significant further decrease at day 4 (†, P = 0.01), but did not reach significance 7 weeks (P = 0.08) after TAC induction (one-way ANOVA, followed by a Bonferroni post-hoc test).

To determine whether impaired LV function at day 0 and day 4 was directly related to a decreased energy status of the myocardium, PCr/ATP was correlated to the EDV, ESV, SV, EF, CO and LV mass as determined during the same measurement session. At day 0, PCr/ATP was not correlated to the morphological and functional indices, i.e., EDV, ESV, SV, EF, CO and LV mass determined in the same scan session ($r < 0.34$, $P > 0.41$, in all cases). Although at day 4 after TAC a decreased PCR/ATP appeared weakly associated with increased EDV and increased LV mass, both trends were not significant ($r = 0.35$, $P = 0.15$ and $r = 0.37$, $P = 0.12$, respectively). For the other functional parameters, no correlations were observed either ($r < 0.24$, $P > 0.33$, in all cases).

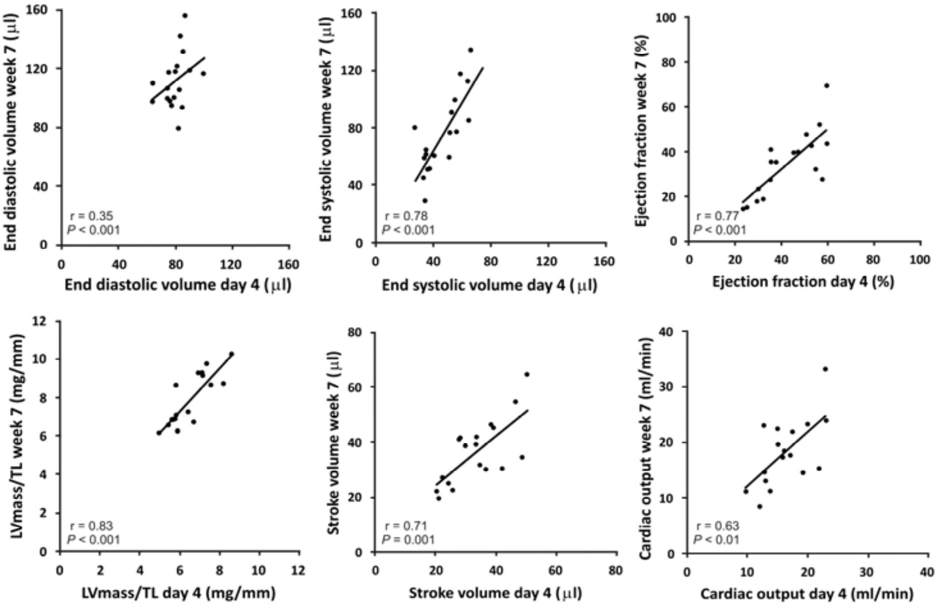

Figure 7.5. LV end-diastolic volume (top left), end-systolic volume (top middle), ejection fraction (top right), stroke volume (bottom left), cardiac output (bottom middle), and LV mass normalized to tibia length (TL) (bottom right) as determined 7 weeks after surgery were plotted as a function of the same parameters at day 4 after surgery.

Next, we determined if PCr/ATP, either determined at day 0 or 4, had predictive value for late LV functional changes. However, no correlation was observed between PCr/ATP at day 0 (r < 0.30, *P* > 0.47, in all cases) and any of the LV functional parameters (EDV, ESV, SV, EF, CO and LV mass) as determined either 7 or 10 weeks after surgery. The same holds for PCr/ATP at day 4 (r < 0.09, *P* > 0.73, in all cases) and any of the LV functional parameters determined 7 or 10 weeks after surgery. Moreover PCr/ATP at day 0 (r < 0.54, *P* > 0.18, in all cases) or day 4 (r < 0.30, *P* > 0.28, in all cases) was not correlated to the change of LV functional parameters from week 7 to week 10.

LV functional parameters (ESV, EF, LV mass, SV and CO) at day 4 did significantly correlate with the same LV functional parameters in the mice 7 weeks (r > 0.62, *P* < 0.01, in all cases) (Figure 7.5) and 10 weeks after surgery (r > 0.52, *P* < 0.05, in all cases) (not shown). EDV at day 4 was not correlated to EDV 7 and 10 weeks after surgery (r = 0.35, *P* = 0.15 and r = 0.10, *P* = 0.99, respectively). In contrast, LV functional parameters at day 0 did not correlate to the same parameters either 7 or 10 weeks after surgery.

Discussion

Evidence is accumulating for a pronounced role of myocardial energy shortage in HF [8]. ^{31}P-MRS measurements can be used to quantify the phosphocreatine-to-ATP (PCr/ATP) ratio, which is an established measure to characterize the energy status of the heart. PCr/ATP is decreased in HF in a wide range of mammals and it has been suggested that it has prognostic value for patient mortality due to HF [13,19,27,28]. The TAC mouse is a well-established model of pressure overload induced HF and is frequently used to study myocardial metabolism in HF [14,17,18,29]. Here, we studied the LV energy status of TAC mice during the onset of myocardial hypertrophy using localized ^{31}P-MRS, and LV function and morphology using cinematographic MR imaging. Findings were related to subsequent myocardial remodeling to determine whether alterations in the PCr/ATP ratio predict LV remodeling.

Hypertrophy in TAC mice was apparent from a significantly increased LV mass and LV dilation was evident from an increased EDV and ESV. TAC mice showed impaired LV function indicated by a decreased EF. Moreover, LV mass, EDV and ESV significantly increased and EF significantly decreased over time in the TAC mice. The increased LuW/TL ratio in TAC mice indicated profound pulmonary remodeling [30]. Notably, LV mass as estimated from cinematographic MRI seemed already increased at the same day shortly after TAC surgery. This might be the result of myocardial edema or small differences in mouse body weight upon the time of inclusion as compared to previous studies, but since no baseline measurements were obtained in the mice before TAC the precise cause cannot be ascertained [31]. Taken together, in this study TAC mice developed a stage of decompensated myocardial hypertrophy.

Previously, we found myocardial PCr/ATP, corrected for partial T_1 saturation, to be 0.99 ± 0.15 in control mice [20]. In the present study, we found impaired LV function at the day of surgery, which was accompanied by a trend towards a decrease of PCr/ATP, pointing to the first signs of a decreased cardiac energy status. This finding suggests that the impaired LV function mainly resulted from a massively increased afterload exceeding the maximum workload of the heart, which was not reflected by a significant change of PCr/ATP. The decreased HR during MR measurements at the day of TAC may have contributed to a decreased cardiac energy demand and as a consequence to the preservation of the near normal myocardial energy status. Previously, it was shown by Naumova *et al.* that the mouse heart can cope with an acute increase of cardiac workload [32]. In their study, dobutamine stress did not result in a decreased PCr/ATP, analogous to our findings in the acute stage after TAC induction. These results emphasize the efforts of the heart to maintain normal PCr and

ATP levels even under challenging circumstances. In the present study, on the other hand, signs of hypertrophic remodeling were visible four days after TAC, i.e., LV mass was slightly increased and LVEF was decreased. At the same time, a significant decrease in PCr/ATP was observed, indicating a decreased energy status of the TAC heart.

In our mouse model, we did not observe a correlation between PCr/ATP and the global LV functional parameters, such as EF, determined during the same measurements and under exactly the same experimental circumstances. It is still debated whether such a relationship exists. While some recent studies indeed have reported moderate correlations between LVEF and PCr/ATP [33,34], in some earlier studies no relation between LV contractile measures and PCr/ATP was found [27,35]. PCr/ATP shows a relative wide range of values within groups as compared to the differences between groups, for example healthy and failing hearts. This holds to a lesser extent also for LVEF. Therefore, it is likely that fairly large, well-defined study groups are required to determine whether LVEF and PCr/ATP indeed are correlated. It is experimentally complicated to quantify absolute PCr and ATP concentrations with the use of reference measurements in a ^{31}P phantom. PCr and ATP concentrations, however, probably constitute a better measure for myocardial energy status than PCr/ATP, and are likely more closely related to LV function [10,18].

The implications of an impaired myocardial energy status for HF development are still subject of extensive research. It remains to be clarified whether impaired energetics are causative or predictive for cardiac disease progression, or potentially suitable as a therapeutic target [8,16,17]. For instance, Maslov *et al.* showed that myocardial PCr/ATP measured three weeks after TAC was inversely correlated to the change of LV EDV from three to six weeks, suggesting that decreased PCr/ATP has predictive value for LV chamber dilation in TAC mice [17]. In our study no relationships were observed between PCr/ATP measured at day 0 or day 4 after surgery, and LV functional status at later time points.

One critical determinant of the course of HF progression is the magnitude of the pressure overload [36]. Indeed, clear correlations were obtained between LV functional parameters determined 4 days after surgery and myocardial function 7 and 10 weeks after surgery. Although these results do not shed any light on the cause and consequence of the resulting remodeling, they do implicate that the severity of the initial functional response to the pressure overload is predictive for the magnitude of the hypertrophic response at later stages, and even predicts subsequent remodeling.

Taken together with the data reported by Maslov *et al.*, the results of our study suggest that although myocardial energy status, expressed as PCr/ATP, might still correlate with myocardial remodeling, it apparently does not critically steer the remodeling process in this early stage. Instead, the severity of the initial hypertrophic response is more important in this period. During a later stage of the disease, however, when PCr/ATP does predict subsequent remodeling, myocardial energy status might become an important modulator of remodeling [17]. Clearly, additional studies are required to confirm this hypothesis, and to further investigate the key determinants that dominate tissue remodeling in the first three weeks after TAC. Maslov *et al.* relied on a small cohort of twelve mice, making the regression analysis to determine the predictive value of PCr/ATP three weeks after TAC rather sensitive to the outcome of individual measurements. Moreover, in their study the mice showed limited hypertrophic growth and an essentially constant EF between three to six weeks after TAC. Studying mice until a stage of decompensated HF could thus yield important additional information of the potential predictive value of PCr/ATP for myocardial remodeling.

There are some limitations to this study. First, in this study we used PCr/ATP as it is a valued measure of myocardial energy status. For future work, we are aiming to do absolute measurements of PCr and ATP concentrations to further improve the characterization of myocardial energy status. Moreover, no baseline ^{31}P-MR spectroscopy and ^{1}H-MR imaging measurements were performed in the mice that underwent TAC. Instead, we relied on data from a control group from a previous study from our lab that was obtained using identical measurement procedures. This was done mainly for practical reasons and to reduce the number of measurements that each mouse had to undergo. Still, we were able to show maladaptive LV remodeling and impaired myocardial energetics in TAC mice, by comparison to previous measurements in age- and gender-matched healthy mice. Second, PCr/ATP was not corrected for the possible contribution of blood pool ATP to the ^{31}P spectra. PCr/ATP might thereby be underestimated, also depending on the myocardial-to-blood volume ratio in the sensitive area of the ^{31}P surface coil within the 3D ISIS voxel. In a previous study, however, we showed that it is reasonable to neglect the contribution of blood to the cardiac ^{31}P-MR spectra (Chapter 6) [20].

Conclusion

PCr/ATP measured at the same day of TAC surgery showed a trend towards lower values and became significantly lower than control mice at day 4. Importantly, PCr/ATP measured at these time points during the first stage of hypertrophic growth, did not predict subsequent functional and anatomical parameters of remodeling. Instead, significant correlations were found between cardiac functional parameters at day 4 after TAC with later outcome.

Acknowledgement

This research was performed within the framework of the Center for Translational Molecular Medicine, project TRIUMPH (grant 01C-103), and supported by the Dutch Heart Foundation. J.J. Prompers is supported by a VIDI grant (project number: 700.58.421) from the Netherlands Organisation for Scientific Research (NWO), and G.J. Strijkers is supported by a VIDI grant (number: 07952) from the Dutch Technology Foundation STW, applied science division of NWO and the Technology Program of the Ministry of Economic Affairs. We thank L.B.P. Niesen, D. Veraart and J. Habets for biotechnical assistance, and Prof. D.J. Duncker (Erasmus Medical Center, Rotterdam) and Prof. Y. Pinto (Academic Medical Center, Amsterdam) for stimulating discussions.

References

1. Denolin, H., et al. Eur Heart J, 1983, 4(7), 445-8.
2. Juenger, J., et al. Heart, 2002, 87(3), 235-41.
3. de Couto, G., et al. Nat Rev Cardiol, 2010, 7(6), 334-44.
4. Lloyd-Jones, D., et al. Circulation, 2010, 121(7), e46-e215.
5. McMurray, J.J., Stewart S. Heart, 2000, 83(5), 596-602.
6. Cokkinos, D.V., Pantos C. Heart Fail Rev, 2011, 16, 1-4.
7. Frey, N., Olson E.N. Annu Rev Physiol, 2003, 65, 45-79.
8. Neubauer, S. N Engl J Med, 2007, 356(11), 1140-51.
9. Turer, A.T., et al. Curr Opin Clin Nutr Metab Care, 2010, 13(4), 458-65.
10. Ingwall, J.S., Weiss R.G. Circ Res, 2004, 95(2), 135-45.
11. Prompers, J.J., et al. Drug Discov Today Technol, 2011, 8(2-4), e95-e102.
12. Ingwall, J.S. Cardiovasc Res, 2009, 81(3), 412-9.
13. Neubauer, S., et al. Circulation, 1997, 96(7), 2190-6.
14. Rockman, H.A., et al. Proc Natl Acad Sci U S A, 1991, 88(18), 8277-81.
15. Dunn, M.E., et al. Cardiovasc Pathol, 2011, 20(6), 343-51.
16. Lygate, C.A., et al. Exp Physiol, 2012, doi: 10.1113/expphysiol.2012.064709.
17. Maslov, M.Y., et al. Am J Physiol Heart Circ Physiol, 2007, 292(1), H387-91.
18. Gupta, A., et al. Circ Cardiovasc Imaging, 2011, 4(1), 42-50.
19. Gupta, A., et al. Am J Physiol Heart Circ Physiol, 2009, 297(1), H59-H64.
20. Bakermans, A.J., et al. Proc Intl Soc Mag Reson Med, Melbourne, Australia, 2012, 0057.
21. van Deel, E.D., et al. J Mol Cell Cardiol, 2011, 50(6), 1017-25.
22. Bakermans, A.J., et al. Circ Cardiovasc Imaging, 2011, 4(5), 558-65.
23. Ordidge, R.J., et al. J Magn Reson, 1986, 66, 283-94.
24. Heijman, E., et al. NMR Biomed, 2007, 20(4), 439-47.
25. Schneider, J.E., et al. J Cardiovasc Magn Reson, 2006, 8(5), 693-701.
26. Heijman, E., et al. J Magn Reson Imaging, 2008, 27(1), 86-93.
27. Hardy, C.J., et al. Am Heart J, 1991, 122(3 Pt 1), 795-801.
28. Tian, R., et al. Circulation, 1997, 96(4), 1313-9.
29. Luptak, I., et al. Circulation, 2007, 116(8), 901-9.
30. Chen, Y., et al. Hypertension, 2012, 59(6), 1170-8.
31. Barsotti, A., et al. Cardiologia, 1993, 38(12 Suppl 1), 67-77.
32. Naumova, A.V., et al. Am J Physiol Heart Circ Physiol, 2003, 285(5), H1976-9.
33. Beer, M., et al. J Am Coll Cardiol, 2002, 40(7), 1267-74.
34. Hansch, A., et al. Eur Radiol, 2005, 15(2), 319-23.
35. Neubauer, S., et al. Circulation, 1992, 86(6), 1810-8.
36. Perrino, C., et al. J Clin Invest, 2006, 116(6), 1547-60.

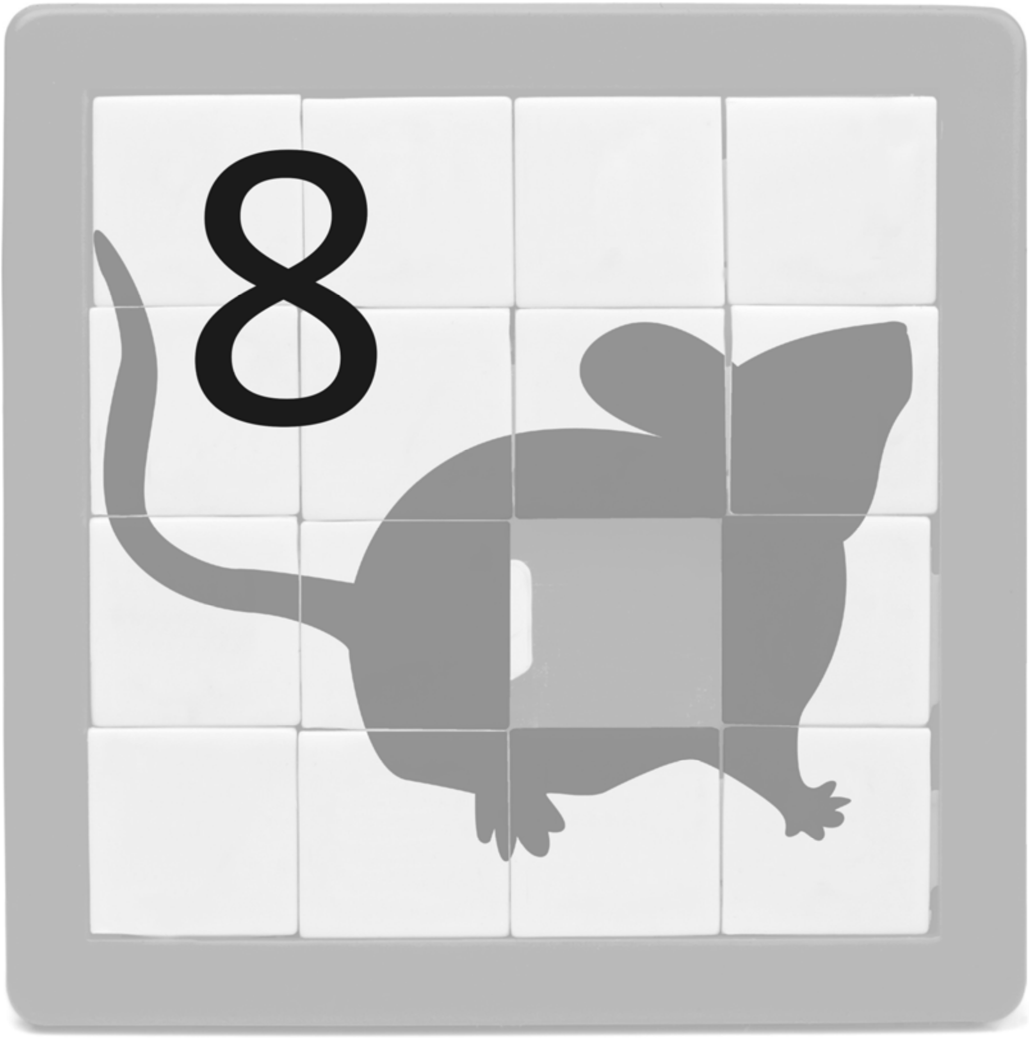

8

General discussion

Heart failure (HF) is the inability of the heart to pump blood at a rate that satisfies the peripheral needs and is a final consequence of many pathologies [1,2]. Left ventricular (LV) pressure overload and myocardial infarction are amongst the most important causes of HF [3,4]. Common and important hallmarks of HF are myocardial hypertrophy, fibrosis, vascular adaptation and metabolic remodeling [5-7]. The role of cardiac magnetic resonance (CMR) as a diagnostic tool for HF is rapidly increasing [8,9]. The prognostic value of important measures of LV function such as ejection fraction, however, is limited [10]. To improve diagnostic relevance and risk stratification additional MR imaging and spectroscopy techniques are therefore highly desired. For that, preclinical research in mouse models plays an important role [11-23].

This **goal** of this thesis was to apply multiple, novel MR imaging methods and phosphorous ^{31}P-MR spectroscopy for the evaluation of mouse HF, with a focus on myocardial hypertrophy, fibrosis, perfusion and LV energy status.

These techniques are part of an ever extending toolbox for mouse CMR that allows the researcher to perform a multi-parametric assessment of myocardial tissue status. Preferably, a time-efficient protocol is constructed from all these tools, which is tailored for a particular HF phenotype and yields the relevant, decisive features of the stage of development towards HF. After successful proof-of-concept studies in mice, these techniques could be translated for clinical use. Ultimately, these techniques might then contribute to improved diagnostic accuracy and a better characterization of the tissue status, new (surrogate) end-points to evaluate the success of therapies and interventions, and perhaps may even provide better prognostic markers for the disease course.

Summarizing discussion

The transverse aortic constriction (TAC) mouse model was used throughout this thesis as it is an important model of pressure overload induced hypertrophy and HF [24]. Since the TAC model was first described, it has been extensively used to study various facets of pressure overload induced LV adaptation [25-33]. In **Chapter 2** we characterized cardiac function and morphology in a mild and severe TAC model. Mice underwent repeated measurements to evaluate the progression of cardiac parameters over time. The mild TAC mice developed a stage of compensated LV hypertrophy and mildly impaired LV function. No progressive deterioration of myocardial function was observed over time and LV maladaptation did not result in pulmonary remodeling and RV failure. LV function and morphology in severe TAC mice, on the other hand, progressively deteriorated over time resulting in overt decompensated hypertrophy, which was also indicated by profound pulmonary remodeling and impaired RV function.

A repeatable method for quantitative, first-pass perfusion MRI of the mouse heart based on a dual-bolus approach was described in **Chapter 3**. A non-saturated arterial input function was acquired from a low-dose $Gd(DTPA)^{2-}$ prebolus. The myocardial tissue response was measured from a separate high-dose $Gd(DTPA)^{2-}$ full-bolus infusion. Perfusion (ml min^{-1} g^{-1}) was quantified using a Fermi constrained deconvolution of the myocardial tissue response with the arterial input function. This calculation critically depends on linearity of the measured MR signal intensity with $Gd(DTPA)^{2-}$ concentration in the LV lumen during the prebolus and in the myocardial wall during the full-bolus. In separate experiments these assumptions were proven to be valid for our experimental conditions. Interestingly, this assumption was to the best of our knowledge never demonstrated *in vivo*, although Weber *et al.* confirmed the appropriateness of this assumption for quantitative first-pass perfusion measurements in the human heart using phantom experiments [34,35].

The first-pass perfusion method was used in **Chapter 4** to study myocardial perfusion in TAC mice, which was considerably decreased as compared to perfusion in control mice. Importantly, the relationship between perfusion and LV morphology and function was studied. Clear correlations were obtained between a decreased perfusion in TAC mice and the indices of LV function and morphology, e.g., LV ejection fraction, volumes as well as LV mass. Although group-averaged perfusion values in TAC mice did not change between measurements in the longitudinal study, these results revealed that with an ensuing hypertrophic growth and concomitantly declining LV function (Chapter 2) perfusion gradually diminishes.

Current MRI techniques for the quantification of diffuse myocardial fibrosis suffer from severe limitations. In **Chapter 5** ultra short echo time (UTE) MRI was used to study replacement and diffuse fibrosis in the *ex vivo* and *in vivo* mouse heart. Here, the MI mouse model was also used as it results in the formation of a spatially confined, collagenous scar providing an ideal model for proof-of-principle purposes. Subtraction of short- and long-TE images resulted in images highlighting tissue with short T_2*, such as collagen. Indeed, a good correlation was obtained between the relative infarct volume as determined from histology and *ex vivo* UTE MRI. UTE MRI also resulted in signal differences between control and TAC hearts, which were related to the amount of collagen present in the hearts. Cardiovascular UTE MRI may thus provide a means for the assessment of diffuse fibrosis based on endogenous tissue contrast.

Impaired myocardial energetics is thought to play an important role in HF. **Chapter 6** describes 3D Image Selected *In vivo* Spectroscopy (ISIS) for single-voxel localized ^{31}P-MRS of the *in vivo* mouse heart. From the resulting spectra the phosphocreatine-to-

ATP (PCr/γ-ATP) ratio was quantified as a measure for myocardial energy status. In mice with a markedly impaired LV systolic function and myocardial hypertrophy 7 weeks after TAC, PCr/ATP was approximately 25% lower as compared to control mice.

Multiple studies have pointed to the possible predictive value of PCr/ATP for subsequent maladaptive ventricular remodeling. It is unclear though if PCr/ATP measured during the first stage of the remodeling process also predicts consecutive maladaptation. In **Chapter 7** the hypothesis was therefore tested that PCr/ATP measured at the day of TAC or four days thereafter predicts subsequent remodeling. Such a relation could, however, not be established. Clear relations were obtained, on the other hand, between LV function and morphology four days after TAC and seven weeks, pointing to the importance of the severity of the initial pressure overload for maladaptive cardiac remodeling. In addition, these experiments showed an apparent decrease of PCr/ATP already at the day of TAC, whereas PCr/ATP four days after TAC was significantly decreased, pointing to the first signs of an impaired myocardial energy status.

Important aspects of myocardial tissue remodeling in the failing human heart are fibrosis, diminished myocardial perfusion and an impaired energy status. The results presented in this thesis, altogether demonstrate that each of these facets can be assessed in the TAC mouse model of HF using dedicated CMR protocols. In each of the studies, cinematographic MRI provided a robust means to quantify LV morphology and function as essential parameters for a solid characterization of the cardiac status. Myocardial perfusion in TAC mice was markedly decreased during the early stage of cardiac remodeling, and remained impaired thereafter (Chapter 4). Importantly, impaired LV perfusion was closely correlated to changes in LV function and morphology in TAC mice, which points to the importance of vascular remodeling for HF. Unfortunately these results do not provide clear evidence for cause and consequence of the remodeling process. Myocardial energy status was significantly decreased four days after TAC (Chapter 7), as well as seven weeks after TAC (Chapter 6). These results emphasize that metabolic remodeling in TAC mice already begins at the onset of hypertrophy, and remains an important aspect of maladaptation thereafter. Fibrosis was only studied seven weeks after TAC in the present thesis (Chapter 5). Souders *et al.*, however, showed that fibrosis is already apparent in the mouse heart one week after TAC induction [36]. The development of diffuse fibrosis in pressure overload induced hypertrophy is known to be a gradual process [37-39]. Fibrosis induced tissue adaptation, therefore, likely contributes to the progressive deterioration of LV function in TAC already from an early stage of hypertrophy, just as vascular and metabolic remodeling.

Myocardial fibrosis, vascular and metabolic adaptation in the development of HF are not independent processes. In fact, they are tightly coupled. Perivascular fibrosis for instance also negatively affects myocardial perfusion, and a decreased oxygen delivery to the heart, in turn, could well contribute to metabolic remodeling [40,41]. The ability to study each of these effects *in vivo* in the same mouse opens many opportunities to further investigate their inter-related, detrimental effects. Such studies might also help in attempts to decipher their mutual dependency in terms of cause and consequence.

Longitudinal studies as described in Chapter 2 are increasingly used in preclinical MR investigations, emphasizing the potential of these study designs for the characterization of mouse cardiac function during the time course of maladaptive remodeling [42-44]. An important reason for this development probably is the increased sensitivity for the detection of changes over time associated with repeated measures within the same animals, which in addition also results in smaller group sizes required. Longitudinal studies have another attractive feature. Disease progression can show considerable time-wise variation between individual TAC mice, as Kaplan-Meier survival analysis clearly showed (Chapter 2). A longitudinal study design naturally takes these differences into account, while they might be obscured by measurements at a single time-point after TAC.

Clinical observations clearly indicate the existence of gender differences in cardiovascular disease prevalence and severity [45]. Similar observations are reported for the MI and TAC mouse models [46]. Typically, male MI mice develop greater LV hypertrophy, dilation and dysfunction as compared to females [47]. Male TAC mice generally develop signs of overt HF, LV dilation and impaired systolic function, whereas female TAC mice show less maladaptive remodeling [48,49]. For that reason, in all studies described in this thesis male mice were used to obtain a severe MI and TAC phenotype. As a result, many of the studied aspects of HF, for example TAC induced perfusion deficits, are likely less pronounced for female mice. This is not necessarily a problem for MR technology development. Ultimately, studies should include mice from both sexes though, to determine the full potential of the newly developed techniques for the assessment of HF. Inclusion of mice from both sexes will also be of importance when further studying the effects of myocardial fibrosis, perfusion deficits and impaired energetics on disease progression.

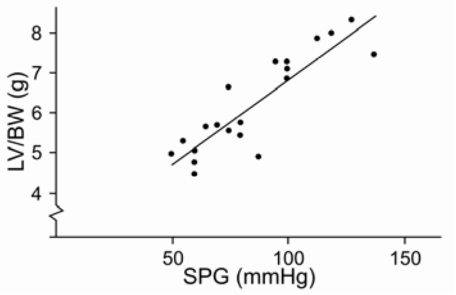

Figure 8.1. Relationship between the systolic pressure gradient (SPG) and the left ventricular-to-body weight ratio (LV/BW) four weeks after TAC, showing that SPG is a key determinant of the magnitude of LV hypertrophy in TAC. Adapted from Perrino *et al.* [50].

The systolic pressure gradient (SPG) across the TAC, measured in a terminal experiment, is frequently used to grade the severity of the stenosis and thereby the success of the surgery [24]. The SPG can decrease over time and is therefore best determined shortly after TAC, which is obviously not possible in a longitudinal study [26]. Various publications have shown the clear relation between the SPG and the resulting increase in LV mass (Figure 8.1) [50]. Post-mortem visual inspection of the TAC in combination with an assessment of the hypertrophic response, as described in this thesis, thus nevertheless provides a valuable means to qualitatively determine the integrity and severity of the stenosis [28].

It is generally accepted that implementation of any surgical animal model is time consuming and requires a highly skilled micro surgeon to minimize subtle surgical variation between animals, resulting in a well-defined, reproducible animal model [27,30]. Despite such efforts, reproduction of results from other laboratories might still not be straightforward [51,52]. It is also of great importance to maintain surgical skills by regularly performing surgical procedures. Knot slippage or differences in the amount of connective tissue removed from the direct vicinity of the transverse aorta can result in subtle variation in the imposed TAC. This may have resulted in the attenuated hypertrophic response as observed in Chapter 4.

Despite the remarkable similarities between cardiac anatomy and function in mice versus man, also important physiological differences exist between both species [53]. Examples are the life span, heart rate, basal metabolic rate, but also the dominant myosin heavy chain isoform [54]. These differences might not necessarily hamper proof-of-principle studies, such as those described in Chapter 5, where the presence of collagen in TAC and MI served as a model to obtain large amounts of tissue components with very short T_2*. Studies involving questions regarding myocardial perfusion and metabolism on the other hand, for instance as described in Chapter 4 and Chapter 7, certainly need further investigations to determine the appropriateness of extrapolation of the results from mouse to man.

The TAC model for pressure overload induced hypertrophy and the PO model for myocardial infarction, although they represent markedly simplified models, have turned into indispensable tools to study the failing heart within the whole organism setting. This is not only of importance for the study of HF etiology, but also for the development of imaging technologies. It is expected that the fast numbers of future HF patients will suffer from comorbidities, such as diabetes, myocardial infarction and obesity [55,56]. This might necessitate the development of new animal models that better resemble these more complex HF pathologies. One example in this direction is a recent study by Chen *et al.* In this study rats were subjected to LV pressure overload and myocardial infarction, to study the effect of pressure overload on vascular adaptation following myocardial infarction [57]. Such models are likely of great importance to assess the full added value of newly developed CMR techniques for the diagnosis and risk stratification in the future HF patient population.

Ethical considerations

Continuous efforts are made to obtain suitable alternatives for research involving animal experiments. One beautiful example is the use of pig hearts obtained from a slaughterhouse, which can be used in a Langendorff setup to study many aspects of myocardial physiology, and are thus of great research value [58]. In order to study complex disorders, such as HF, it is unavoidable to use *in vivo* models that closely resemble human pathology. Such studies ultimately contribute to improvements of patient healthcare and are thus of great social importance, but also come with a great responsibility for the researcher. Efforts should be made to design all experiments in accordance with the principles of replacement, reduction and refinement [59]. The use of longitudinal experiments described in multiple chapters in this thesis, for instance, results in substantial reductions of the number of mice necessary in studies. Anesthesia and analgesia should be used whenever necessary for pain relief and minimization of animal discomfort. Of particular interest for the work in this thesis were regular checks of mice after TAC and MI as they can very rapidly develop signs of overt HF. Further use of mice under such circumstances results in disproportional discomfort and was considered not justified, resulting in termination of the experiment.

Integration of knowledge from multi-parametric CMR recordings

The clinical picture of HF is not well described by one single measurement parameter [4]. This might well be the result of the multifactorial character of HF etiology, and variable symptoms and clinical outcome in patients [60,61]. In addition, many of the facets of maladaptive cardiac remodeling are tightly linked. The use of plasma biomarkers in combination with rapidly advancing imaging technology and genetic testing might provide a means to further improve diagnostics for patients [62]. Ho *et al.* showed the power of such an approach [63]. In hypertrophic cardiomyopathy patients serum levels of C-terminal propeptide of type I procollagen (PICP), a biomarker of collagen metabolism, were studied in relationship to cardiac morphology and function determined from CMR. This study showed that PICP levels were already elevated in patients with normal cardiac morphology as compared to healthy subjects, and PICP levels further increased in patients with overt hypertrophic cardiomyopathy. Another example are circulating microRNA's (miRNA), that hold great promise as biomarkers for various cardiovascular diseases [64,65]. For instance, Eitel *et al.* studied plasma concentrations of miRNA-133a in relation to myocardial damage to assess its potential prognostic value [66]. Increased miRNA-133a concentration was associated with larger infarcts, but did not add independent prognostic information to traditional and CMR markers of disease progression.

Since HF is a multifactorial disease, a multi-parametric CMR approach to measure different aspects of the remodeling heart could provide a means to further improve tissue characterization and thereby achieve a better diagnostic accuracy. In fact, this is the long-standing promise of CMR to obtain a comprehensive assessment of different aspects of myocardial function and morphology during one measurement session, the so-called one-stop-shop [67]. Clinically, one important limitation for such an approach were measurement time restrictions. The increased use of parallel imaging and acceleration techniques, such as GRAPPA, results in strong reductions of acquisition times [68]. In addition with continuous improvements in image quality and an extending range of MR applications available, some important limitations have been eliminated for reaching a comprehensive assessment of myocardial tissue status using a multi-parametric CMR exam [69].

A number of existing and newly developed CMR techniques could aid in future improvements in diagnostic accuracy and better myocardial tissue characterization. To obtain a comprehensive overview a selection had to be made of the most exciting and relevant tools, that are briefly discussed below. The reader is referred to the many cited papers for in-depth information on each of the techniques.

Cardiac morphology and function

Cinematographic MRI of the beating heart is an essential technique enabling characterization of cardiac morphology, and diastolic and systolic function (Figure 8.2). For these applications ultrasound is still most widely used, but MRI is valued for its high spatial resolution and excellent tissue contrast [70]. Due to limited acoustic windows

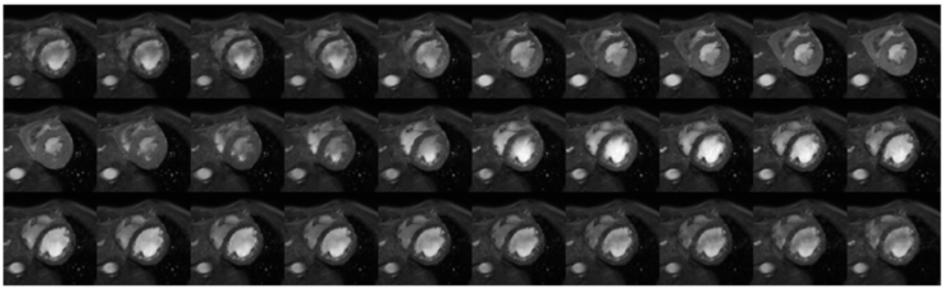

Figure 8.2. Series of 30 short-axis cinematographic MR images obtained in a healthy volunteer from the beginning of systole (top left) to end-diastole (bottom right). Images of Hans van Assen (Eindhoven University of Technology) and Jos Westenberg (Leiden University Medical Center).

oblique imaging planes cannot be freely defined in ultrasound, which is not a problem in MRI. As a result, MRI can quantify LV function and morphology with high accuracy and reproducibility and without geometric assumptions, which is of particular importance in ischemic heart disease. As with many MRI techniques, cinematographic imaging comes in many different variants: ECG triggered or self-gated acquisitions, bright or black blood imaging, and numerous different MR sequences are available. Notably, many current segmented acquisition schemes still acquire cinematographic data over multiple consecutive heart beats. Real-time approaches have also been proposed for the human heart with good in-plane (~ 2 mm) and temporal resolution (~ 30 ms) by exploiting the full potential of parallel imaging techniques with a strongly undersampled radial acquisition scheme, which alleviates an important drawback of MRI as compared to ultrasound [71].

Diastolic function measurements can provide information on the ratio of active-to-passive filling of the ventricles, which is an important marker of cardiac function in a large subset of patients that suffer from HF with a normal LV ejection fraction [10]. In MRI this data can be derived from mitral flow measurements. Alternatively, the LV filling rate can be quantified using LV volumetric data from cinematographic MR images sampled at a high temporal resolution during the cardiac cycle [72-74]. This technique can be of great benefit for patients that display diastolic dysfunction.

Signal intensities across the myocardial wall in cinematographic MRI are fairly homogeneous complicating direct regional motion analysis from this data. Instead, dedicated techniques for 2D and 3D regional motion quantification have been developed such as MR tagging [75,76]. Tagging techniques are based on the tracking of lines or a grid, obtained by local modulation of the MR signal, which moves along with the myocardium during the cardiac cycle (Figure 8.3). Although many methods have

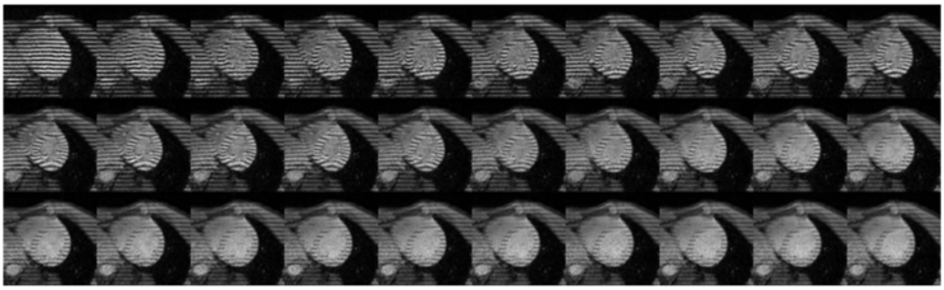

Figure 8.3. Series of 30 short-axis tagged, cinematographic MR images obtained in the same healthy heart as depicted in Figure 8.2, from the beginning of systole (top left) to end-diastole (bottom right). Images of Hans van Assen (Eindhoven University of Technology) and Jos Westenberg (Leiden University Medical Center).

been proposed to extract tissue motion and strain from tags, quantitative analysis of these images still requires time-consuming, complicated procedures. This is an important limitation that to a certain extent also holds for the other methods for regional motion quantification, i.e., phase contrast MRI, displacement encoding with stimulated echoes and strain encoding [77]. As a result, all these tools are essentially only used in research settings [69]. Nevertheless, studies of myocardial tissue deformation have yielded valuable insights in cardiac mechanics [43,78-82]. Lumens *et al.*, for example, showed an increased LV torsion-to-shortening ratio in asymptomatic elderly subjects compared to controls, pointing to decreased endocardial relative to epicardial function, while LV ejection fraction remained unaffected [83]. Ultimately, characterization of regional tissue motion might be of special interest in patients where a near normal global LV function obscures the presence of local motion abnormalities [84]. This will require the availability of robust, fast and automated post-processing tools.

Myocardial fibrosis

Late Gd-enhanced MRI is a robust and widely accepted tool for the quantification of replacement fibrosis and is not only valuable for infarct tissue characterization, but also to assess fibrosis in hypertrophic cardiomyopathy patients [85]. This technique, however, is less well suited for the assessment of diffuse myocardial fibrosis [86]. Diffuse fibrosis results in increased tissue stiffness negatively affecting both diastolic and systolic function, and is associated with poor clinical outcome. Currently, diffuse fibrosis is still diagnosed using biopsy specimens, for which a noninvasive alternative is highly desired. Research efforts to design MR techniques for the quantification of diffuse fibrosis are therefore ample and include approaches based on T_1, T_2* as well as $T_1\rho$ contrast.

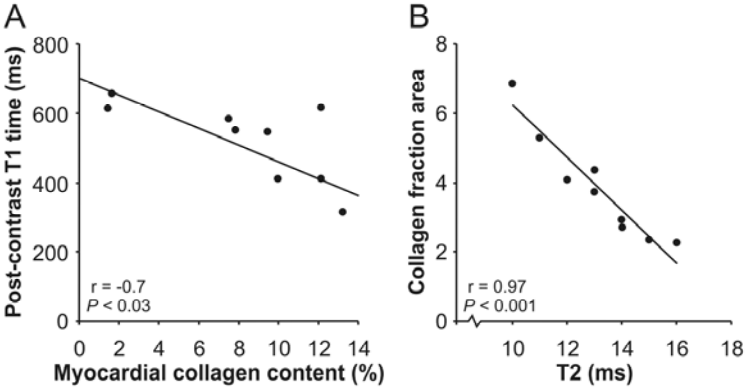

Figure 8.4. (A) Correlation between the myocardial collagen content and post-contrast T_1 time in HF patients with diffuse fibrosis (adapted from Iles *et al.* [87]). (B) Correlation between *in vivo* T_2 values and the collagen fractional area in diabetic mouse hearts (adapted from Bun *et al.* [88]).

Iles *et al.* showed that post-contrast T_1, measured after the injection of a bolus of $Gd(DTPA)^{2-}$, was lower in HF patients compared to healthy subjects [87]. Importantly, the lower post-contrast T1 value moderately correlated with increased myocardial collagen content in a rather small subset of 9 patients (Figure 8.4A), and was associated with impaired diastolic function. A slightly different approach is based on probing the myocardial distribution volume of $Gd(DTPA)^{2-}$, which is increased in fibrotic areas [86]. This is exploited during continuous contrast agent infusion, when myocardial T_1 values depend on the distribution volume rather than on the in- and efflux kinetics. Flett *et al.* used this approach and showed a clear correlation between MRI derived myocardial distribution volume and the collagen volume fraction measured using histology [89,90].

Alternatively, diffuse collagen content has also been quantified by means of T_2 and T_2* measurements. Bun *et al.* studied the *in vivo* mouse heart after streptozotocin-induced diabetes and found a clear negative correlation between myocardial T_2 and the collagen fractional area determined from histology (Figure 8.4B) [88]. Similarly, Loganathan *et al.* measured a lower T_2 in the diabetic Sprague-Dawley rat heart as compared to their healthy littermates [91]. Here, a direct comparison between T_2 and tissue collagen content was not made, but increased collagen content was observed in the diabetic hearts. Finally, Aguor *et al.* reported a significant decrease in T_2* in myocardial infarction using a multi-gradient-echo sequence [92]. In fact, these techniques are based on similar endogenous contrast mechanism as those exploited in Chapter 5.

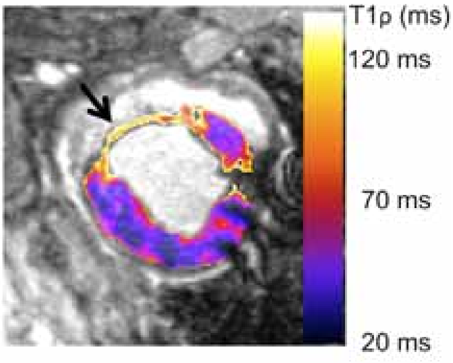

Figure 8.5. Short-axis cross section through a pig heart eight weeks after myocardial infarction overlaid with a $T_1\rho$ map. Infarct and myocardial $T_1\rho$ were 91.7 ms and 47.2 ms, respectively, resulting in clear image contrast between both regions. Adapted from Witschey *et al.* [93].

A recent, exciting development is spin-lock MRI providing so-called $T_1\rho$ contrast, which provides information complementary to contrast based on T_1-, T_2- or proton density [94,95]. $T_1\rho$ contrast is modulated by processes on a macromolecular level and is therefore recognized as a potential readout for the presence of fibrotic tissue. Witschey *et al.* explored one potential application of this technique in a pig model of myocardial infarction (MI) at 3T, an important field strength for clinical applications (Figure 8.5) [93]. $T_1\rho$ nearly doubled in the fibrotic scar compared to remote tissue yielding excellent contrast between both regions. The cardiac application of $T_1\rho$ imaging is still in its infancy, but these results certainly warrant further investigation to explore the full potential of $T_1\rho$ contrast. It can be foreseen that $T_1\rho$ imaging will provide data complementary to late Gd-enhanced MRI, while having the advantage of exploiting endogeneous contrast. In addition, $T_1\rho$ imaging could prove valuable for the assessment of diffuse fibrosis in other cardiomyopathies, including pressure overload induced hypertrophy and hypertrophic cardiomyopathy.

Myocardial perfusion

Contrast enhanced MR imaging as applied in Chapter 3 and Chapter 4, and arterial spin labeling (ASL) measurements are amongst the most widely used MRI techniques for myocardial perfusion quantification [96]. ASL measurements rely on endogenous contrast, which is a distinct advantage compared to contrast enhanced techniques. Although ASL measurements are frequently used to measure human brain perfusion, cardiac ASL applications are still limited [96,97]. Cardiac ASL comes with a number of challenges, including relatively low signal-to-noise ratios and very small flow-dependent signal changes (1-8 %) in the heart that are difficult to robustly measure at clinical field strengths (1.5-3 T) [98].

Human myocardial first-pass perfusion measurements, on the other hand, are widely adopted and are well suited to quantify resting state perfusion and the perfusion reserve [99-101]. Regional perfusion differences in ischemic heart disease make the potential value of contrast-enhanced measurements obvious. First-pass measurements could also be of great value in non-ischemic heart disease. Petersen *et al.*, for instance, found profound hyperemic perfusion deficits in hypertrophic cardiomyopathy patients [102]. Here, quantitative measurements are of great importance as no clear regional perfusion differences are anticipated.

At the present time it remains to be seen if contrast-enhanced perfusion measurements will find their way to clinical routine [96]. This depends on many factors, but will probably not be hindered by the accuracy of the measurement technique. A recent study by Greenwoud *et al.* showed superior diagnostic accuracy of a multi-parametric MRI exam compared to SPECT perfusion measurements for the diagnosis of suspected coronary heart disease [103]. The MR exam included cine imaging, rest-stress perfusion measurements, late-Gd enhanced acquisitions and MR coronary angiograms, resulting in a better sensitivity and negative predictive values.

Cardiac metabolic remodeling

The use of ^{31}P-MRS offers a unique means to noninvasively measure adenosine triphosphate and phosphocreatine levels, which are key metabolites for cardiac energy metabolism, and ^{1}H-MRS offers the possibility to study creatine and myocardial lipid content, but is less often used than ^{31}P-MRS (Figure 8.6) [104]. Small animal and human studies exploiting cardiac MRS have yielded many new insights in cardiac metabolism [105-108]. At this moment, however, this has not resulted in widespread use in clinical cardiology, which is related to challenges regarding reproducibility, and in particular for ^{31}P also with the inherent low MR sensitivity as compared to ^{1}H [104,109]. With the increasing awareness of the importance of metabolic adaptation in pathological hypertrophic remodeling, the use of cardiac MRS may be expected to increase in view of the valuable information that it provides in addition to other MRI derived parameters. Successful clinical translation, however, will require significant advances with respect to reproducibility of the spectroscopy methods, wide clinical availability of spectroscopy sequences and hardware, and, importantly, a more elaborate evaluation of the added value of these measurements for diagnostic purposes [110].

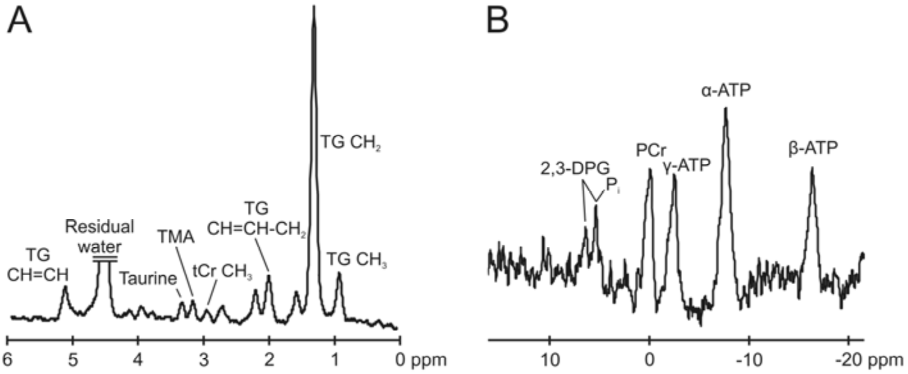

Figure 8.6. *In vivo* localized mouse cardiac ^{1}H-MRS reporting on myocardial lipids and creatine content (A), and ^{31}P spectrum enabling the detection of adenosine triphosphate (ATP) and phosphocreatine (PCr) (B). Courtesy of A.J. Bakermans (Eindhoven University of Technology).

Other developments in CMR

Diffusion tensor imaging (DTI) is a well-recognized technique to measure muscle fiber orientation in a non-destructive way [111]. In addition, various DTI derived parameters help to characterize muscle tissue status, for instance via the mean diffusivity, the fractional anisotropy (reflects on the tissue anisotropy) and the myocardial disarray (measure for the presence of abnormally organized myofibers) [112-116]. Strijkers *et al.*, for instance, studied tissue remodeling in the *ex vivo* mouse heart after myocardial infarction using DTI and reported an increase of the fractional anisotropy between 7 and 14 days after infarct induction in the border zone and remote region of the heart [117]. Clearly, a direct mechanistic link exists between muscle fiber orientation and tension development during muscle contraction. For this reason, DTI gained much scientific attention to study muscle fiber remodeling in cardiac diseases. DTI measurements of the beating heart, however, are very challenging, requiring extremely demanding MR sequences and very powerful MR hardware [118,119]. Therefore, only recently the feasibility of reproducible *in vivo* DTI could be shown for the human (Figure 8.7) and mouse heart [119-122]. These recent developments already enabled studies in which the relationship of local myocardial fiber orientation and contraction, for example determined from MR tagging data, is quantified [123]. In particular, Wang *et al.* used a finite element model to integrate fiber orientation and contraction in the human heart, and found a homogeneous strain along the fiber direction in end-systole [124].

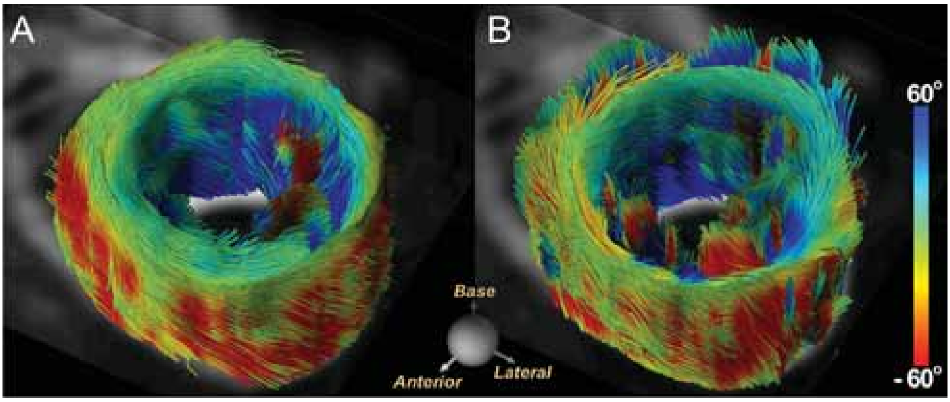

Figure 8.7. 3D fiber tractography of the human LV obtained with a multiple breath hold technique (A) and using a navigator based approach (B). Color coding on the fibers represents their helix angle. Reprinted with permission from Nielles-Vallespin *et al.* [120].

The application of *in vivo* DTI is expected to advance our knowledge of normal cardiac physiology, but also of the impact of fiber remodeling in cardiac pathologies. In particular, *in vivo* DTI measurements could play a vital role to study the potential positive effects of myocardial salvaging therapies after myocardial infarction, for example experimental stem cell treatment, on fiber remodeling [125]. Pressure overload induced hypertrophy will probably result in more subtle fiber remodeling than changes induced by myocardial infarction, with prominent differences in DTI derived parameters between the infarct, the border zone and remote tissue [126]. As a result, studying fiber remodeling in pressure overload induced hypertrophy is probably more challenging than in hearts following myocardial infarction.

Molecular imaging aims to visualize specific molecular markers of disease processes [127]. A beautiful example of such an approach is a study by Caravan *et al.* presenting a peptide-based collagen-targeted MR contrast agent [128]. The probe accumulated in the collageneous scar of a mouse heart, 40 days after myocardial infarction, resulting in bright contrast on T_1-weighted images (Figure 8.8). Molecular imaging thus provides a way to visualize molecular markers that would otherwise go undetected, given the typical resolution and sensitivity of MRI [13,14]. However, due to concerns regarding the possibilities for clinical translation of novel Gd-containing contrast agents, in particular targeted versions that have prolonged retention times, future developments of molecular imaging agents for MRI have become uncertain [129].

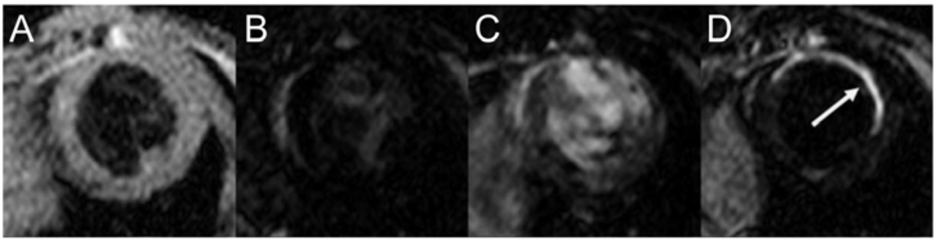

Figure 8.8. Short-axis cross sections of a mouse heart 40 days after myocardial infarction obtained with a peptide-based collagen targeted MR contrast agent. From left to right T_2-weighted black blood image, and inversion recovery images obtained before, 1 min and 40 min after injection of the contrast agent. Reprinted with permission from Caravan *et al.* [128].

Future perspectives

The increasing role of CMR in clinical practice combined with a multitude of techniques to characterize various aspects of HF etiology could contribute to a number of improvements. Blood levels of BNP or NT-proBNP are known to be prognostic markers for HF [130]. LV pathological hypertrophy is also known to be associated with increased risk of cardiovascular mortality [131]. HF is a multi-factorial disease though, and it is therefore unlikely that the disease stage or even the disease progression is adequately described by one or a few measurement parameters. It is to be expected that the possibility to quantify multiple aspects of HF etiology using MR technology, beyond plain myocardial function and morphology, can contribute to improved diagnostic accuracy. One such example is the application of T_2* CMR for the diagnosis of thalassaemia major, an inherited cardiac disease resulting in cardiac iron overload [132,133]. Marked reductions in mortality as a result of this pathology have been observed following the introduction of MRI-based diagnosis, which is attributed to reductions in myocardial iron overload. Here, T_2* measurements played a key role to steer the successful application of iron chelator treatment. In addition, it is currently very difficult to predict the effect of HF treatment on an individual basis due to the lack of suitable (surrogate) end-points, again possibly related to the heterogeneity of cardiac remodeling. In addition, there is a need to intervene even before symptoms of HF become apparent, emphasized by recent guidelines for the diagnosis and management of HF in which two out of the four categories describe asymptomatic patients [134,135]. The increased number of readout parameters from a CMR exam might provide new end-points to evaluate treatment strategies, also in an earlier stage of maladaptive cardiac remodeling.

Many studies have used MRI to search for additional parameters that predict subsequent myocardial remodeling or patient outcome, which is of great interest to improve patient risk stratification [43,108,136]. In fact, this is an old desire, expressed already in 1937: 'The very essence of cardiovascular practice is recognition of early heart failure' [137]. Related to this quest are many unresolved issues with regard to HF development, for instance whether microvascular dysfunction is a mere consequence of maladaptation or also contributes to cardiac disease progression, or perhaps both [138,139].

Answering these questions is not simple, as a result of the progressive nature of HF etiology. Examples are plentiful. Myocardial hypertrophy itself ensues bit by bit during the disease course [29,140]; the coronary flow reserve gradually decreases over time as a result of pressure overload induced hypertrophy and HF [32]; diffuse myocardial fibrosis develops progressively [37-39]; metabolic remodeling also progresses over time [7,105,106]. Moreover, the plasticity of the heart is likely to result in continuous attempts to compensate for maladaptation, which could partly mask the true effects of vascular, metabolic or extracellular matrix remodeling [141].

There are a number of elegant studies, nevertheless, that attempted to predict cardiac remodeling or patient outcome. Neubauer *et al.*, for instance, showed that PCr/ATP predicts mortality in patients with acquired dilated cardiomyopathy [108]. Similarly, data presented by Maslov *et al.* suggests that PCr/ATP in pressure overload induced hypertrophic remodeling in the mouse can predict LV dilation to some extent [136]. Hankiewicz *et al.* used MR tagging to study the protein kinase C-ε transgenic mouse model, which displays a phenotype of dilated cardiomyopathy [43]. LV dilation in these mice was preceded in time by a decrease in myocardial wall thickening, from which the authors concluded that dysfunction at the level of the myofibril might be causative for wall thinning. Mathiassen *et al.* found that the media-to-lumen ratio of resistance arteries measured from subcutaneous biopsies in subjects with essential hypertension had predictive value for cardiovascular event-free survival, including amongst others the absence of myocardial infarction, HF, stroke, transient ischemic attacks and cardiovascular death, assessed over a period of more than 11 years [142]. In a similar study Rizzoni *et al.* also suggested the prognostic value of the media-to-lumen ratio [111].

Still, the number of studies that were successful in finding a solid, prognostic marker for cardiac remodeling or patient outcome can be considered limited. Some remarks might illustrate the difficulties associated with finding suitable prognostic imaging or spectroscopic markers for cardiac remodeling, let alone that one could predict patient outcome on an individual basis. The study by Neubauer *et al.*, for example, was conducted on a small cohort of patients (n = 39) with a LV ejection fraction < 50% upon inclusion. A clear difference in survival resulted between patients with a PCr/ATP either higher or lower than 1.6. Although the study has been cited >270 times, none of these studies showed a follow-up in a substantial cohort of patients. Interestingly, the study by Maslov *et al.* searched for a similar effect in TAC mice (n = 12). Indeed PCr/ATP predicted subsequent ventricular remodeling. Given the small patient or animal groups often examined, more extensive studies are needed, both in human patients and in appropriate animal models, to critically evaluate the applicability of the PCr/ATP ratio as a prognostic marker of HF progression. It also remains to be determined to which extent these results can be extrapolated to different HF phenotypes, and during which phases of the disease course prognostic markers have the most predictive power.

CMR has the unique advantage of being extremely versatile, as illustrated by a selection out of many different MR measurement methods discussed above. If multi-parametric exams indeed prove valuable for myocardial tissue characterization to further improve current diagnostic tools, MRI has a large lead as compared to other cardiac imaging modalities, e.g., ultrasound, computed tomography, positron emission tomography and single-photon emission computed tomography. For many of the CMR techniques, there is still much to gain, which will further increase their potential for clinical implementation. Time will tell whether future studies, exploiting multi-parametric MR approaches, indeed can live up to this promise.

Conclusion

Cardiac MRI in mice plays an important role in the development of new imaging techniques that characterize myocardial tissue on a level beyond conventional tissue morphology and function. With the results of this thesis the toolbox for mouse cardiac MRI has been further extended, and now includes: a method for the quantification of myocardial perfusion (ml min^{-1} g^{-1}) based on contrast-enhanced MR imaging; a tool to assess diffuse and replacement fibrosis *in vivo*, using ultra-short TE MRI exploiting endogenous contrast mechanisms; and a method to quantify myocardial energy status in terms of the phosphocreatine-to-adenosine triphosphate ratio, using localized ^{31}P-MRS.

These methods were used to study pressure overload induced left ventricular hypertrophy following TAC in the mouse. Results showed that myocardial perfusion in TAC mice was markedly impaired and was correlated to LV morphology and function, and that TAC hearts are exposed to metabolic remodeling from the early onset of hypertrophy.

Future preclinical studies should aim at obtaining the most relevant combination of decisive features obtained in a time-efficient, multi-parametric CMR protocol, that aid in improved HF diagnostics and risk stratification. Such studies can provide important guidance to subsequent evaluation of these multi-parametric approaches in the clinical setting.

References

1. Denolin, H., et al. *Eur Heart J,* 1983, **4**(7), 445-8.
2. Houser, S.R., et al. *Circ Res,* 2012, **111**(1), 131-50.
3. Roger, V.L., et al. *Circulation,* 2011, **123**(4), e18-e209.
4. Hunt, S.A., et al. *Circulation,* 2009, **119**(14), e391-e479.
5. Cokkinos, D.V., Pantos C. *Heart Fail Rev,* 2011, **16**, 1-4.
6. Frey, N., Olson E.N. *Annu Rev Physiol,* 2003, **65**, 45-79.
7. Neubauer, S. *N Engl J Med,* 2007, **356**(11), 1140-51.
8. Constantine, G., et al. *Lancet,* 2004, **363**(9427), 2162-71.
9. Alfayoumi, F., et al. *Rev Cardiovasc Med,* 2007, **8**(3), 135-44.
10. Maeder, M.T., Kaye D.M. *J Am Coll Cardiol,* 2009, **53**(11), 905-18.
11. Coolen, B.F., et al. *NMR Biomed,* 2011, **24**(2), 154-62.
12. Coolen, B.F., et al. *Magn Reson Med,* 2010, **64**(6), 1658-63.
13. Coolen, B.F., et al. *NMR Biomed,* 2012, **25**(8), 969-84.
14. Geelen, T., et al. *NMR Biomed,* 2012, **25**(8), 953-68.
15. Makowski, M., et al. *Magn Reson Med,* 2010, **64**(6), 1592-8.
16. Sosnovik, D.E., et al. *Circ Cardiovasc Imaging,* 2009, **2**(6), 460-7.
17. Heijman, E., et al. *NMR Biomed,* 2007, **20**(4), 439-47.
18. Dall'armellina, E., et al. *Magn Reson Med,* 2012, **67**(2), 541-51.
19. Bakermans, A.J., et al. *Circ Cardiovasc Imaging,* 2011, **4**(5), 558-65.
20. Coolen, B.F., et al. *J Cardiovasc Magn Reson,* 2011, **13**, 56.
21. Aguor, E.N., et al. *Int J Cardiovasc Imaging,* 2012, doi: 10.1007/s10554-012-0093-6.
22. van Nierop, B.J., et al. *Magn Reson Med,* 2012, doi: 10.1002/mrm.24424.
23. Epstein, F.H., et al. *Magn Reson Med,* 2002, **47**(3), 482-91.
24. Rockman, H.A., et al. *Proc Natl Acad Sci U S A,* 1991, **88**(18), 8277-81.
25. Givvimani, S., et al. *J Appl Physiol,* 2011, **110**(4), 1093-100.
26. van Deel, E.D., et al. *J Mol Cell Cardiol,* 2011, **50**(6), 1017-25.
27. Lygate, C. *Drug Discov Today Dis Models,* 2006, **3**(3), 283-90.
28. Lygate, C.A., et al. *Basic Res Cardiol,* 2006, **101**(1), 8-16.
29. van Nierop, B.J., et al. *PLoS ONE,* 2013, **8**(2), e55424.
30. Tarnavski, O., et al. *Physiol Genomics,* 2004, **16**(3), 349-60.
31. deAlmeida, A.C., et al. *J Vis Exp,* 2010, doi: 10.3791/1729.
32. Hartley, C.J., et al. *Ultrasound Med Biol,* 2008, **34**(6), 892-901.
33. Qu, J., et al. *Circ Res,* 2009, **104**(3), 365-71.
34. Weber, S., et al. *J Magn Reson Imaging,* 2008, **28**(1), 51-9.
35. Weber, S., et al. *J Magn Reson Imaging,* 2007, **26**(3), 569-79.
36. Souders, C.A., et al. *Am J Pathol,* 2012, **181**(4), 1226-35.
37. Díez, J., et al. *Nat Clin Pract Cardiovasc Med,* 2005, **2**(4), 209-16.
38. Díez, J. *J Clin Hypertens (Greenwich),* 2007, **9**(7), 546-50.
39. Weber, K.T., et al. *Am J Hypertens,* 1989, **2**(12 Pt 1), 931-40.
40. Dai, Z., et al. *J Cardiol,* 2012, **60**(5), 416-21.
41. Brilla, C.G., Maisch B. *Eur Heart J,* 1994, **15 Suppl D**, 45-52.
42. Stuckey, D.J., et al. *PLoS ONE,* 2012, **7**(1), e28569.
43. Hankiewicz, J.H., et al. *Am J Physiol Heart Circ Physiol,* 2008, **294**(1), H330-H6.
44. Costandi, P.N., et al. *Am J Physiol Heart Circ Physiol,* 2006, **291**(6), H2971-H9.
45. Luchner, A., et al. *Cardiovasc Res,* 2002, **53**(3), 720-7.
46. Patten, R.D. *Drug Discov Today Dis Models,* 2007, **4**(4), 227-32.
47. Cavasin, M.A., et al. *Life Sci,* 2004, **75**(18), 2181-92.
48. Douglas, P.S., et al. *J Am Coll Cardiol,* 1998, **32**(4), 1118-25.
49. Skavdahl, M., et al. *Am J Physiol Heart Circ Physiol,* 2005, **288**(2), H469-H76.

50. Perrino, C., et al. *J Clin Invest,* 2006, **116**(6), 1547-60.
51. Martin, T.P., et al. *Exp Physiol,* 2012, **97**(7), 822-32.
52. Mohammed, S.F., et al. *Cardiovasc Pathol,* 2012, **21**(3), 188-98.
53. Wessels, A., Sedmera D. *Physiol Genomics,* 2003, **15**(3), 165-76.
54. Hamlin, R.L., Altschuld R.A. *Circ Cardiovasc Imaging,* 2011, **4**(1), 2-4.
55. Breckenridge, R. *Dis Model Mech,* 2010, **3**(3-4), 138-43.
56. Westenbrink, B.D., et al. *Eur J Heart Fail,* 2012, **14**(10), 1090-6.
57. Chen, J., et al. *Am J Physiol Heart Circ Physiol,* 2012, doi: 10.1152/ajpheart.00793.2012.
58. Sutherland, F.J., Hearse D.J. *Pharmacol Res,* 2000, **41**(6), 613-27.
59. Rowan, A.N. *Dev Biol Stand,* 1980, **45**, 175-80.
60. McMurray, J.J., Stewart S. *Heart,* 2000, **83**(5), 596-602.
61. McMurray, J.J.V., Pfeffer M.A. *Lancet,* 2005, **365**(9474), 1877-89.
62. Wollert, K.C. *Eur Heart J,* 2012, **33**(18), 2246-8.
63. Ho, C.Y., et al. *N Engl J Med,* 2010, **363**(6), 552-63.
64. Creemers, E.E., et al. *Circ Res,* 2012, **110**(3), 483-95.
65. Tijsen, A.J., et al. *Am J Physiol Heart Circ Physiol,* 2012, **303**(9), H1085-95.
66. Eitel, I., et al. *Am Heart J,* 2012, **164**(5), 706-14.
67. Kramer, C.M. *Cardiol Clin,* 1998, **16**(2), 267-76.
68. Griswold, M.A., et al. *Magn Reson Med,* 2002, **47**(6), 1202-10.
69. Finn, J.P., et al. *Radiology,* 2006, **241**(2), 338-54.
70. Atalay, M.K. *J Am Coll Radiol,* 2005, **2**(9), 740-8.
71. Uecker, M., et al. *NMR Biomed,* 2010, **23**(8), 986-94.
72. Coolen, B.F., et al. *Magn Reson Med,* 2012, doi: 10.1002/mrm.24287.
73. Motaal, A.G., et al. *NMR Biomed,* 2012, doi: 10.1002/nbm.2883.
74. Caudron, J., et al. *Radiographics,* 2011, **31**(1), 239-59.
75. Axel, L., Dougherty L. *Radiology,* 1989, **171**(3), 841-5.
76. Axel, L., Dougherty L. *Radiology,* 1989, **172**(2), 349-50.
77. Wang, H., Amini A.A. *IEEE Trans Med Imaging,* 2012, **31**(2), 487-503.
78. Hankiewicz, J.H., et al. *Circ Cardiovasc Imaging,* 2010, **3**(6), 710-7.
79. Herold, V., et al. *Magn Reson Med,* 2006, **55**(5), 1058-64.
80. Gotte, M.J.W., et al. *J Am Coll Cardiol,* 2006, **48**(10), 2002-11.
81. Russel, I.K., et al. *J Cardiovasc Magn Reson,* 2011, **13**(1), 3.
82. Nucifora, G., et al. *Circ Cardiovasc Imaging,* 2010, **3**(4), 433-42.
83. Lumens, J., et al. *Am J Physiol Heart Circ Physiol,* 2006, **291**(4), H1573-H9.
84. Shehata, M.L., et al. *J Cardiovasc Magn Reson,* 2009, **11**(1), 55.
85. Jackson, E., et al. *Clin Radiol,* 2007, **62**(5), 395-403.
86. Osorio, J. *Nat Rev Cardiol,* 2010, **7**(10), 542.
87. Iles, L., et al. *J Am Coll Cardiol,* 2008, **52**(19), 1574-80.
88. Bun, S.-S., et al. *Invest Radiol,* 2012, **47**(5), 319-23.
89. Flett, A.S., et al. *Eur Heart J Cardiovasc Imaging,* 2012, **13**(10), 819-26.
90. Flett, A.S., et al. *Circulation,* 2010, **122**(2), 138-44.
91. Loganathan, R., et al. *Int J Cardiovasc Imaging,* 2006, **22**(1), 81-90.
92. Aguor, E.N.E., et al. *Magn Reson Mat Phys Biol Med,* 2012, **25**(5), 369-79.
93. Witschey, W.R., et al. *J Cardiovasc Magn Reson,* 2012, **14**, 37.
94. Ulmer, J.L., et al. *AJNR Am J Neuroradiol,* 1996, **17**(5), 805-19.
95. Sepponen, R.E., et al. *J Comput Assist Tomogr,* 1985, **9**(6), 1007-11.
96. Jerosch-Herold, M. *J Cardiovasc Magn Reson,* 2010, **12**, 57.
97. Detre, J.A., et al. *J Magn Reson Imaging,* 2012, **35**(5), 1026-37.
98. Epstein, F.H., Meyer C.H. *J Am Coll Cardiol Img,* 2011, **4**(12), 1262-4.
99. Heydari, B., et al. *Prog Cardiovasc Dis,* 2011, **54**(3), 191-203.
100. Muehling, O.M., et al. *J Cardiovasc Magn Reson,* 2004, **6**(2), 499-507.

101. Gerber, B.L., et al. *J Cardiovasc Magn Reson,* 2008, **10**, 18.
102. Petersen, S.E., et al. *Circulation,* 2007, **115**(18), 2418-25.
103. Greenwood, J.P., et al. *Lancet,* 2012, **379**(9814), 453-60.
104. Ten Hove, M., Neubauer S. *Heart Fail Rev,* 2007, **12**(1), 48-57.
105. Ingwall, J.S., Weiss R.G. *Circ Res,* 2004, **95**(2), 135-45.
106. Ingwall, J.S. *Cardiovasc Res,* 2009, **81**(3), 412-9.
107. Bottomley, P.A. *Science,* 1985, **229**(4715), 769-72.
108. Neubauer, S., et al. *Circulation,* 1997, **96**(7), 2190-6.
109. Hudsmith, L.E., Neubauer S. *J Am Coll Cardiol Img,* 2009, **2**(1), 87-96.
110. Holloway, C., Clarke K. *Heart Lung Circ,* 2010, **19**(3), 154-60.
111. Le Bihan, D., et al. *Radiology,* 1986, **161**, 401-7.
112. Strijkers, G.J., et al. *Israel J of Chem,* 2003, **43**, 71-80.
113. Francalanci, P., et al. *Hum Pathol,* 1995, **26**(3), 262-6.
114. Eggen, M.D., et al. *Magn Reson Med,* 2012, **67**(6), 1703-9.
115. Kim, S., et al. *Magn Reson Med,* 2005, **54**(6), 1387-96.
116. Healy, L.J., et al. *J Cardiovasc Magn Reson,* 2011, **13**, 74.
117. Strijkers, G.J., et al. *NMR Biomed,* 2009, **22**(2), 182-90.
118. Gamper, U., et al. *Magn Reson Med,* 2007, **57**(2), 331-7.
119. Toussaint, N., et al. *Med Image Comput Comput Assist Interv,* 2010, **13**(Pt 1), 418-25.
120. Nielles-Vallespin, S., et al. *Magn Reson Med,* 2012, doi: 10.1002/mrm.24488.
121. Huang, S., et al. Proc Intl Soc Mag Reson Med, Stockholm, Sweden, 2010, 488.
122. McGill, L.A., et al. *J Cardiovasc Magn Reson,* 2012, **14**(1), 86.
123. Wu, Y., Wu E.X. *Conf Proc IEEE Eng Med Biol Soc,* 2009, **2009**, 4395-8.
124. Wang, B., et al. IEEE International Symposium on Biomedical Imaging, Barcelona, 2012, 46-9.
125. Dauwe, D.F., Janssens S.P. *Curr Pharm Des,* 2011, **17**(30), 3328-40.
126. Wu, M.T., et al. *Circulation,* 2006, **114**(10), 1036-45.
127. Osborn, E.A., Jaffer F.A. *J Am Coll Cardiol Img,* 2010, **3**(11), 1181-95.
128. Caravan, P., et al. *Angew Chem Int Ed Engl,* 2007, **46**(43), 8171-3.
129. Kuo, P.H., et al. *Radiology,* 2007, **242**(3), 647-9.
130. van Kimmenade, R.R.J., et al. *J Am Coll Cardiol,* 2009, **53**(10), 884-90.
131. Levy, D., et al. *N Engl J Med,* 1990, **322**(22), 1561-6.
132. Wood, J.C., Noetzli L. *Ann N Y Acad Sci,* 2010, **1202**, 173-9.
133. Modell, B., et al. *J Cardiovasc Magn Reson,* 2008, **10**, 42.
134. Hunt, S.A., et al. *J Am Coll Cardiol,* 2009, **53**(15), e1-e90.
135. Owens, A.T., Jessup M. *J Am Coll Cardiol Img,* 2012, **5**(9), 881-3.
136. Maslov, M.Y., et al. *Am J Physiol Heart Circ Physiol,* 2007, **292**(1), H387-91.
137. Lewis, T. Diseases of the heart. New York: The MacMillan Co, 1937.
138. Izumiya, Y., et al. *Hypertension,* 2006, **47**(5), 887-93.
139. Cecchi, F., et al. *N Engl J Med,* 2003, **349**(11), 1027-35.
140. Kemp, C.D., Conte J.V. *Cardiovasc Pathol,* 2012, **21**(5), 365-71.
141. Hill, J.A., Olson E.N. *N Engl J Med,* 2008, **358**(13), 1370-80.
142. Mathiassen, O.N., et al. *J Hypertens,* 2007, **25**(5), 1021-6.

9

List of publications
Dankwoord
Curriculum vitae

List of publications

Papers

B.J. van Nierop, H.C. van Assen, E.D. van Deel, L.B.P. Niesen, D.J. Duncker, G.J. Strijkers, and K. Nicolay. *Phenotyping of left and right ventricular function in mouse models of compensated hypertrophy and heart failure with cardiac MRI*. Plos ONE, 2013, doi: 10.1371/journal.pone.0055424.

B.J. van Nierop, B.F. Coolen, W.J.R. Dijk, A.D. Hendriks, L. de Graaf, K. Nicolay, and G.J. Strijkers. *Quantitative first-pass perfusion MRI of the mouse myocardium*. Magn Reson Med, 2012, doi: 10.1002/mrm.24424.

B.J. van Nierop, A. Stekelenburg, S. Loerakker, C.W.J. Oomens, D.L.. Bader, G.J. Strijkers, and K. Nicolay. *Diffusion of water in skeletal muscle tissue is not influenced by compression in a rat model of deep tissue injury*. J. Biomech, 2010, 43(3), p570 - 575.

A.G. Gefen, **B.J. van Nierop**, D.L. Bader, and C.W.J. Oomens. *Strain-time cell death threshold for skeletal muscle in a tissue-engineered model system for deep tissue injury*, J. Biomech, 2008, 41(-), p2003-2012.

Selected conference proceedings

B.J. van Nierop, J.L. Nelissen, N.A.M. Bax, A.G. Motaal, L de Graaf, K. Nicolay and G.J. Strijkers. *In vivo ultra short TE (UTE) MRI detects diffuse fibrosis in hypertrophic mouse hearts.* In “Proceedings of the Annual meeting of the ISMRM”, April 2013, Salt Lake City, USA.

B.J. van Nierop, J.L. Nelissen, N.A.M. Bax, L. de Graaf, K. Nicolay and G.J. Strijkers. *In vivo ultra short TE (UTE) MRI of mouse myocardial infarction*. In “Proceedings of the Annual meeting of the ISMRM”, May 2012, Melbourne, Australia. **Magna Cum Laude Merit Award**.

B.J. van Nierop, B.F. Coolen, W.J.R. Dijk, L. de Graaf, K. Nicolay and G.J. Strijkers. *Repeatability of quantitative first-pass perfusion MRI in the mouse myocardium*. In “Proceedings of the Annual meeting of the ISMRM”, May 2012, Melbourne, Australia.

A.J. Bakermans, **B.J. van Nierop**, D. Abdurrachim, K. Nicolay and J.J. Prompers. *In vivo cardiac 31P-MRS in a mouse model of heart failure*. In “Proceedings of the Annual meeting of the ISMRM”, May 2012, Melbourne, Australia.

C. Gill, S. Meredith, A.J. Bakermans, **B.J. van Nierop**, G.J. Strijkers, H.C. van Assen, N. Colgan and K.M. Curran. *Linking myocardial function and structure through tagged MRI and diffusion tensor imaging*. In "Proceedings of the Annual meeting of the ISMRM", May 2012, Melbourne, Australia.

C. Gil, N. Colgan, A.J. Bakermans, **B.J. van Nierop**, G.J. Strijkers, H.C. van Assen and K.M. Curran. *Similarity measures for cardiac diffusion tensor imaging registration*. In "Proceedings of the Irish Machine Vision and Image Processing Conference", September 2011, Dublin, Ireland.

B. J. van Nierop, E.D. van Deel, D.J. Duncker, G.J. Strijkers and K. Nicolay. *Temporal evolution of cardiac function in mice with myocardial hypertrophy and heart failure*. In "Proceedings of the Annual meeting of the ISMRM", May 2011, Montreal, Canada.

B.J. van Nierop, T.J.L. Schreurs, H.C. van Assen, G.J. Strijkers and K. Nicolay. *Optimal tag distance for myocardial MR motion analysis of healthy and diseased mice*. In "Proceedings of the Annual meeting of the ISMRM", May 2011, Montreal, Canada.

C. Gil, N. Colgan, A. Bakermans, **B.J. van Nierop**, G. Strijkers, H.C. van Assen and K.M. Curran. *Cardiac Diffusion Tensor Imaging Registration*. In "Proceedings of the Annual meeting of the ISMRM", May 2011, Montreal, Canada.

B.J. van Nierop, E.D. van Deel, D.J. Duncker, K. Nicolay and G.J. Strijkers. *Global LV function in mice during the development of heart failure. An in vivo MRI study*. In "Proceedings of the SCMR/EuroCMR Joint Scientific Sessions", February 2011**,** Nice, France.

B.J. van Nierop, G.J. Strijkers, W.M. Blankesteijn and K. Nicolay. *Global and local LV function in mice during the development of HF. An in vivo MRI study*. In "Proceedings of the Annual Meeting of the Benelux ISMRM Chapter", January 2010, Utrecht, The Netherlands.

B.J. van Nierop, A. Stekelenburg, S. Loerakker, C.W.J. Oomens, G.J. Strijkers and K. Nicolay. *Water diffusion is not influenced by compression of skeletal muscle tissue. An in vivo MRI study.* In "Proceedings of the Annual Meeting of the Benelux ISMRM Chapter", December 2008, Antwerp, Belgium.

A.G. Gefen, **B.J. van Nierop**, D.L. Bader and C.W.J. Oomens. *A Method for Determining the Strain-Time Endurance of Cells in Planar Tissue-Engineered Constructs Subjected to Large Compressive Deformations*. In "Proceedings of the ASME Summer Bioengineering Conference", June 2008, Marco Island, FL, USA, p.253-4.